EPFL

The role of Zn in C-S-H atomic structure, nucleation and growth

Anna MORALES MELGARES

École
polytechnique
fédérale
de Lausanne

2023

Acknowledgements

This thesis and all of the work behind it would not have been possible without the advice of my supervisors; Karen Scrivener and Lyndon Emsley. I would like to thank both of them for accepting me into their respective labs: The Laboratory of Construction Materials (LMC) and the Laboratory of Magnetic Resonance (LRM). LMC and LRM are two laboratories from which I had the opportunity to learn different things and I am grateful to have met the incredible people who were working in them at the time.

First, I would like to thank the people at LMC, especially Paul Bowen, who guided me closely so that I could make sense of my experiments and consciously plan my experimental activity. He has also been always a very friendly figure who made sure we had a space to talk about our concerns, scientific and extracurricular.

From LMC, I also have to acknowledge my office companion, lab mate and, most importantly, close friend Maya Harris. Thanks for all those moments at the office, for teaching me how to precipitate C-S-H and for still commenting on reality shows with me, even if you are now in the far-away land of Luzern. And of course, many thanks as well to Andrea Teixeira who was also in the same project as me and who has been a friend inside and outside of the lab (and who shares a passion about Oporto). And last but not least, I also have to thank Ziga Casar, who has been working with me in our zinc-related project and without whom we would have not been able to pull-off a very nice publication.

Secondly, I would like to thank all of the people at LRM, especially Pinelopi Moutzouri, who taught me the intricacies of NMR (and was also very patient with me) and who is by all means one of the most intelligent people I know; and also, Amrit Venkatesh, who has always been very didactic, knowledgeable and friendly and who is now continuing his career overseas.

It would be a huge mistake not to mention one of the most important people who have helped this project move forward: Andrea Testino, from the Paul Scherrer Institute (PSI). Without him, Chapter 4 of this thesis would be non-existent. His will to make a comprehensive thermodynamic and kinetic model for C-S-H precipitation and to help me elucidate how to make the experimental work that it requires has definitely meant a huge step for my work and for myself. I would also like to mention that despite his teachings… I will always drink cappuccino after lunch, even if its sacrilege.

I would also like to thank all of my friends from outside the lab; especially Kato and Rubén who understand the difficulties of academia and who share a lot of my interests. I also have to thank Carmen Maza, who has been my roommate and friend for two years now and with whom I have been gossiping all around and also tried to unravel the truths and nuances of the human condition. Of course, my biggest thanks go to Ismael Carbayo, who has shown me what true companionship and love mean and with whom my life is several orders of magnitude brighter.

And last but not least, I would like to thank my parents, Aurelia Melgares and Rafael Morales, who have always been exceptionally supportive of me and my decisions and who have always been very clear about the importance of pursuing my dreams, whichever shape they take.

Thank you all for these years of support and love,

Anna.

Abstract

The most promising solution towards cementitious materials with a lower carbon footprint is the partial substitution of the clinker by supplementary cementitious materials (SCMs) such as fly ash, blast furnace slag, limestone and calcined clays. The production of these materials does not imply the formation of CO_2, but its implementation into cement pastes tends to lower the early-age strength of the latter. However, it has recently been demonstrated that the addition of zinc can enhance the mechanical strength of a clinker and therefore allow for a higher substitution of SCMs. The main hydration product of Portland Cement is calcium-silicate-hydrate (C-S-H), which constitutes 60% of its volume and is responsible for the main peak in the heat release curve during cement hydration (main hydration peak). Therefore, it is of utmost importance to study the effect of zinc in isolated and synthetic C-S-H systems.

This work introduces an extensive study through ^{29}Si solid-state nuclear magnetic resonance (NMR), density functional theory (DFT) simulations and molecular dynamics (MD) brick modelling to resolve the atomic structure of zinc-modified synthetic C-S-H. MD simulations are a method for analysing the movement and final positions of atoms in a structure in a fixed period of time. DFT is a computational quantum mechanical modelling used to investigate the electronic structure of the previously obtained bricks to determine the expected chemical shifts from the Si species. The possible structures obtained from MD and their expected chemical shifts obtained through DFT are then compared to NMR experimental data. To prepare the samples for this NMR analysis, aqueous sodium metasilicate, calcium nitrate and zinc nitrate solutions are reacted under controlled pH, temperature and atmospheric conditions. This precipitations process yields pure single-phase C-S-H in the presence of zinc with a target Ca/Si ratio of 1.75. Dynamic nuclear polarization (DNP) enhanced multi $\{^1H\}^{29}Si$ cross-polarization (multiCP) magic-angle spinning (MAS) NMR is used to measure the populations of the different Si species in the zinc-modified C-S-H structure. In addition, we use Incredible Natural Abundance Double Quantum Transfer Experiment (INADEQUATE) to determine the connectivities between silicate species which are present in the samples. Based on atomistic modeling, DFT simulations and experimental evidence it is found that there are two main new Si species, $Q^{(1,Zn)}$ and $Q^{(2p,Zn)}$, present.

The next step towards a complete description of C-S-H and zinc-modified C-S-H is understanding the nucleation and growth mechanisms of both materials. Here, a comprehensive C-S-H model is also developed which includes a complete set of thermodynamic and kinetic equations from classical nucleation theory and is fitted to high-quality data of all stages of precipitation: pre-titration, pre-precipitation, nucleation, growth, and equilibration. In addition, the model is extended to describe zinc-modified C-S-H and has potential to be extended to other C-S-H-derived materials. Although the model needs to be refined, it is a big step towards understanding the thermodynamic and kinetic processes involved in the nucleation and growth of C-S-H.

Table of contents

List of Figures

List of tables

v

Contents

Chapter 1: Introduction

1.1 Concrete: the most important construction material

1.1.1 What is concrete?

Cementitious materials have been in use since up to 12.000 years ago, dating back to the beginning of the Epipaleolithic period.[1] The first cement-like materials, made from burnt limestone and clay, were found in modern Israel, Egypt, Turkey, and Italy. These materials were composed of earth, limestone, calcium sulfates, slacked lime, and volcanic ash (pozzolana) and were used to construct all sorts of buildings, from housing to monuments like the Colosseum.[2] However, it was not until the industrial revolution in Europe during the 18th century that new discoveries, like the relation between the hydraulicity of cement and its clay content, were made. The increasing need of building construction in the cities and the recently gained interest in construction materials led Joseph Aspdin, a British bricklayer and builder, to experiment with calcined limestone and water, and develop, in 1824, the cementitious mixture known today as Portland Cement.[3]

Although Aspdin's Portland Cement was mainly used to build industrial buildings through the 19th century, modern Ordinary Portland Cement (OPC) is massively produced nowadays, hitting its record production of 4.4 billion tons/year in 2021.[4] Today, OPC is the most important construction material, and the most abundant man-made material on Earth, making up to 30-50% of all materials we produce. The main reasons why cement is so widely used are its durability, its reliability, its resistance to erosion, its low cost of only 0.12 USD/kg, its versatility, and its low carbon footprint of 0.7 $kgCO_2$/kg (see Figure 1.1).[5,6]
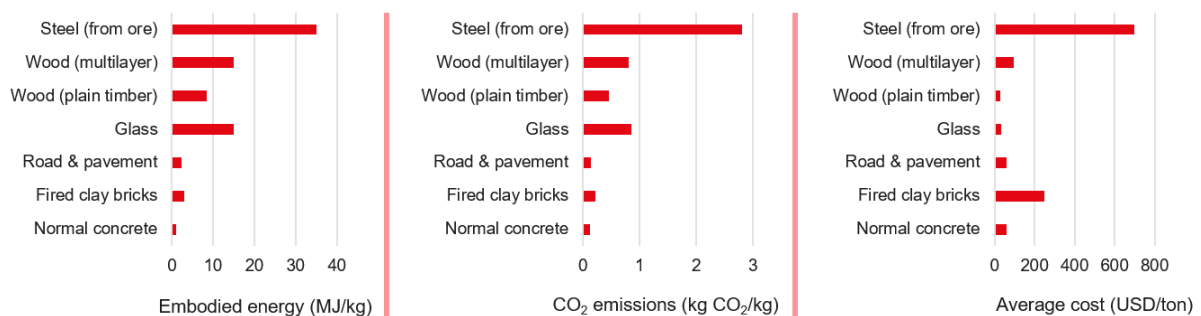
Figure 1.1: Embodied energy (MJ/kg), CO_2 emissions (kg CO_2/kg) and average cost (USD/ton) of popular construction materials.

The cement making process encompasses several steps. Limestone and clay are first sintered and milled to obtain the anhydrous mixture of phases known as the clinker.[7] The clinker typically contains tricalcium silicate (C_3S), dicalcium silicate (C_2S), and phases containing calcium, silicon, aluminium, and iron.[8] Water is then added, and the paste undergoes mixing. New phases precipitate after the addition of water: the hydration products. These hydration products, such as calcium silicate hydrate (C-S-H) and portlandite (CH), act as binders, pulling the anhydrous particles that did not dissolve upon hydration. After hydration, the cement paste hardens. The final construction material used nowadays comes from the hydration of not only cement clinker, but also particulate aggregates (sand, gravel, and crushed stone) that are added in the mixture. Together, particulate aggregates and cement binders (like OPCs) make the composite material we know as concrete.[9]

1.1.2 Concrete and CO_2: a problematic with numbers

The unprecedented economic growth and, by extension, population increase that humankind experienced during the 20th century, along with the industrialization of most human societies, has led to global warming and climate change. Numerous publications prove the correlation between the 1-degree increase in the average temperature of planet Earth and the ever-increasing CO_2 emissions from fossil fuels, agriculture, and the cement industry.[10,11]
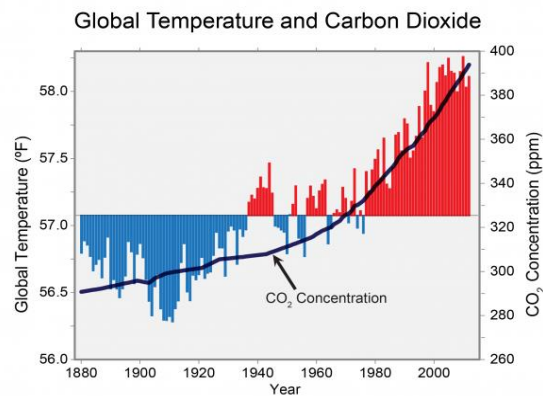
Figure 1.2: Global annual temperature compared to the average CO2 concentration in the atmosphere. Red bars show temperatures above the long-term average and blue bars show temperatures below the long-term average.[12]

Evidence points to the fact that the cement industry is contributing for at least 7-10% of the anthropogenic CO_2 emissions and therefore there is an increasing need for new strategies to palliate CO_2 pollution.[13–16] Two paths are usually proposed: substituting cement for other materials or making cement more environmentally friendly.

1.1.3 Alternatives to cement: ¿are there any?

Given the ever-increasing CO_2 emissions arising from the cement industry one might think about possible alternatives to cement. However, the abundance of its raw components, its low cost compared to other construction materials, the easiness of its manipulation and implementation, its strength, and its durability, make cement irreplaceable nowadays. Additionally, the CO_2 emissions per mass unit of cement remain one of the lowest among construction materials, making cement, again, the best option.

Wood can be utilized as a construction material and is widely used around the world, especially for building furniture, railroad ties, crossbeams, and utility poles, among many others. However, the mass of wood produced per year is still far from the mass of cement produced per year (around 200 M tonnes[17] and around 4 B tonnes,[18] respectively). This stems from the fact that wood has a high embodied energy per mass when studying its full life cycle and comparing it to cementitious materials. It is therefore not a good alternative to cement except for niche applications like construction in areas close to forests.[19]

There are other materials that are often used for construction like adobe, which employ raw materials such as soil, straw and grovel; these are known as **crude-earth materials**. Crude-earth materials are used often in poor areas since they have a low cost and can be fabricated with nearby raw materials

from the construction area itself. Crude-earth construction implies a limitation on the height of the buildings as well as on their shape, for they require thicker walls than wood, cement, or brick buildings.

Geopolymers consist of a slag mixture (produced as a by-product of the steel industry) which dissolves in an alkali solution. The resulting silicon and aluminium monomers form a gel known as C-(N)-A-S-H, which is responsible for the strength of the material. Geopolymers are also known as alkali-activated cements (AACs) and are often proposed as environmentally friendly alternatives to Portland cement. Although AACs are promising and could also be used in construction along with Portland cement, the quantity of aluminosilicates that the steel industry produces and hence the amount of AAC that can be fabricated from their dissolution, is not comparable to the amount of Portland cement produced worldwide.[20] For AACs to fully substitute cement production, the aluminosilicate production from the steel industry should increase at least by an order of magnitude, making geopolymers plausible materials to be used along with cement, but not on their own.

Other construction materials such as clay bricks or steel, although with high workability and compressive strength, are discarded because of their higher CO_2 emissions or cost when compared to concrete.[21] The embodied energy, CO_2 emissions and average cost of several construction materials of interest are shown in Figure 1.1.

The difficulty (or impossibility) of substituting concrete as a construction material evidences the need for solutions within the cement and concrete industry. Although materials like wood, geopolymers and crude-earth options can also coexist with concrete, these are not likely to overcome the availability, low-cost and over-all efficacy of the latter. Realistic solutions to the CO_2 problem must revolve around making cement and concrete more environmentally friendly; that is where Supplementary Cementitious Materials (SCMs) play a major role.

1.2 A compromising solution: supplementary cementitious materials (SCMs)

SCMs are materials that can be added to Portland cement, and which don't imply the emission of CO_2. In addition, some of these materials are also used to further enhance some other characteristics. For instance, SCMs are also mixed with concrete to increase durability, mitigate alkali reactivity or improve the overall hardened properties.[22,23]

The most common SCMs used in both the industry and at the research level are fly ash, blast furnace slag, silica fume, natural pozzolans (like calcined clay and metakaolin) and limestone. Nowadays, almost all cements available in the market are not 100% pure but contain at least some percentage of limestone (around 5%). In addition, some cement mixtures contain more than one type of SCM; these are then named ternary cements. One of the best examples of ternary cements is the so-called Limestone, Calcined Clay Cement or LC3[7] (which also contains a percentage of gypsum, a common practice that helps the retardation of cement hydration, which will be discussed in further sections).

The Laboratory of Construction Materials (LMC) at EPFL is a pioneer on LC3 and a leading group in the sector. LC3 mixtures allow for a substitution of clinker of up to 50% (see Figure 1.3), which will help with the CO_2 emissions dramatically if implemented widely. However, there is a need to further push this boundary to cope with global warming: this will be one of the driving forces of this work and an important point to keep in mind.

4
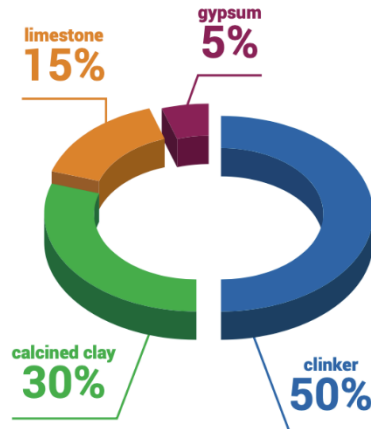
Figure 1.3: percentage of substitution by calcined clay, gypsum and limestone in LC3 cements.

1.3 An element with potential for CO_2 mitigation: zinc

The need for more environmentally friendly cements has driven researchers to study materials with potential for CO_2 mitigation upon mixing with clinker. Among these materials, zinc has recently gained interest because it has been shown in different works that it can enhance the heat release during the acceleration period of C_3S or alite hydration.[24,25] This increased reactivity translates into higher 1-day early-age strength properties, which are desirable since they allow for higher clinker substitutions by SCMs.

The enhanced reactivity and the concomitant accelerated strength development are related to the growth of longer C-S-H particles whose nucleation and growth governs the main hydration peak. While the availability of calcium is a limiting factor in C-S-H growth, zinc has also shown an effect on the formation of this hydration product. Small amounts of zinc oxide in alite enhance the heat flow and the degree of hydration and they also result in longer and thicker outgrows of C-S-H particles.[26] The works that describe the effects of zinc as a minor element in alite and C_3S hydration will be further discussed in Chapter 2, Section 2.5.

Although the addition of zinc could increase the cost of cement, understanding its role in cement hydration is still relevant since it can potentially help with CO_2 mitigation by enhancing the rate of hydration and allowing for higher SCM substitution. Additionally, zinc is commonly found in several industrial waste streams and can be given a new purpose and incorporated into lower-CO_2 cements.

1.4 Statement of the problem and goals

The main goal of this thesis is understanding the role of zinc in synthetic C-S-H as well as its atomic-level position within this material. Previous studies have focused on C-S-H as a product of the hydration of C_3S and alite but during this work, C-S-H will be precipitated synthetically under controlled laboratory conditions using the set-up described previously by Kumar et al.[27] and Harris et al.[28]

Controlled precipitation in terms of temperature, pH and atmosphere are required to precipitate pure-phase C-S-H with specific Ca/Si ratios. It is important to precipitate synthetic C-S-H to reduce the degrees of freedom in the system and to study C-S-H, without other phases in the hydrated product. Being able to precipitate C-S-H and zinc-modified C-S-H gels which are single phase and that can be compared to those found in real cement systems (e.g. Ca/Si=1.7) is therefore one of the goals of this work, and the first one that needs to be accomplished in order to move forward.

To understand the reasons behind the enhanced reactivity of cement in presence of zinc, zinc-modified single-phase synthetic C-S-H was investigated by means of **nuclear magnetic resonance (NMR)**. C-S-H lacks long-range periodicity in its crystal structure: it's a nanocrystalline material. Because C-S-H is nanocrystalline, techniques which rely on long-range periodicity are discarded to study the atomic-level position of zinc when coprecipitated with C-S-H. The most relevant technique which can help elucidate the chemical environments of the different elements that take part in zinc-modified C-S-H is NMR. This is why the second main goal of this thesis is to elucidate the atomic-level structure of zinc-modified C-S-H by means of ^{29}Si NMR, which is easier to carry out when compared to ^{43}Ca and ^{67}Zn NMR, and which has already been used to determine the structures of both C-S-H and C-A-S-H. Additionally, dynamic nuclear polarization (DNP) will be used, which is a technique that enhances the signals through the use of microwaves (MW) and which significantly reduces experimental times.

Determining the atomic-level structure of zinc-modified C-S-H is crucial to fundamentally understand why the reactivity of cement is enhanced, but a thermodynamic and kinetic study is also vital to get a full picture of how zinc affects the nucleation and growth of C-S-H. This is why this thesis will also focus on developing a thermodynamic and kinetic model of C-S-H nucleation and growth in absence and presence of zinc by adapting the model developed by Carino et al,[29] who described the nucleation and growth of synthetic $CaCO_3$ through the evolution of calcium activity.

The specific goals of this thesis are:

- To precipitate single-phase zinc-modified C-S-H.

- To verify the incorporation of zinc in C-S-H.

- To elucidate by means of DNP-enhanced ^{29}Si-NMR the atomic-level structure of zinc-modified C-S-H.

- To develop a thermodynamic and kinetic model for C-S-H and zinc-modified C-S-H.

6

1.5 Structure of this thesis

This thesis is composed of 6 different chapters whose content is described below:

Chapter 1 (introduction, pages 1-9) defines the general scope of this work and the specific goals that are to be met during this dissertation.

Chapter 2 (state of the art, pages 10-30) describes the previous work done by other researchers and groups that is relevant to this thesis. In this chapter, the fundamental knowledge regarding the effect of zinc in cement hydration, DNP-enhanced NMR on C-S-H and C-A-S-H, and thermodynamic modelling will be discussed. This chapter is of vital importance to further understand the goals of this thesis in the framework of the research that has already been done.

Chapter 3 (The Atomic-level structure of zinc-modified C-S-H, pages 31-51) examines the incorporation of zinc in the C-S-H structure by means of XRD-TEM, and the atomic-level structure of this material by means of DNP-enhanced ^{29}Si-NMR. This chapter corresponds to a publication which is accessible at https://pubs.acs.org/doi/10.1021/jacs.2c06749.

Chapter 4 (Thermodynamic and kinetic modelling, pages 52-77) describes the thermodynamic and kinetic modelling done to achieve one of the major goals of this thesis: to make a model for C-S-H and zinc-modified C-S-H. A complete description of the experiments, the final model and future perspectives are described in this chapter.

Chapter 5 (Conclusions, pages 78-83) summarizes the results seen through this thesis and discusses the conclusions that can be extracted from this work while putting in perspective the role of zinc during C-S-H precipitation, nucleation and growth.

Annex (pages 84-108) contains the Supporting Information of Chapter 3 (which corresponds to the publication "The Atomic-level structure of zinc-modified C-S-H", and which is accessible at: https://pubs.acs.org/doi/10.1021/jacs.2c06749. Additionally, a small study about the simultaneous incorporation of aluminium and zinc in C-S-H is also included.

1.6 References

(1)   Jahren, P.; Sui, T. *History of Concrete: A Very Old and Modern Material*; World Scientific, 2017.

(2)   Silva, D. A.; Wenk, H. R.; Monteiro, P. J. M. Comparative Investigation of Mortars from Roman Colosseum and Cistern. *Thermochim Acta* **2005**, *438* (1–2), 35–40.

(3)   Halstead, P. E. The Early History of Portland Cement. *Transactions of the Newcomen Society* **1961**, *34* (1), 37–54.

(4)   Lim, C.; Jung, E.; Lee, S.; Jang, C.; Oh, C.; Shin, K. N. Global Trend of Cement Production and Utilization of Circular Resources. 에너지공학 **2020**, *29* (3), 57–63.

(5)   Sanjuán, M. Á.; Andrade, C.; Mora, P.; Zaragoza, A. Carbon Dioxide Uptake by Cement-Based Materials: A Spanish Case Study. *Applied Sciences* **2020**, *10* (1), 339.

(6)   Hammond, G. P.; Jones, C. I. Embodied Energy and Carbon in Construction Materials. *Proceedings of the Institution of Civil Engineers-Energy* **2008**, *161* (2), 87–98.

(7)   Scrivener, K.; Martirena, F.; Bishnoi, S.; Maity, S. Calcined Clay Limestone Cements (LC3). *Cem Concr Res* **2018**, *114* (August 2017), 49–56. https://doi.org/10.1016/j.cemconres.2017.08.017.

(8)   Herfort, D.; Moir, G. K.; Johansen, V.; Sorrentino, F.; Arceo, H. B. The Chemistry of Portland Cement Clinker. *Advances in Cement Research* **2010**, *22* (4), 187–194.

(9)   Hewlett, P.; Liska, M. *Lea's Chemistry of Cement and Concrete*; Butterworth-Heinemann, 2019.

(10)   Knapp, T.; Mookerjee, R. Population Growth and Global CO2 Emissions: A Secular Perspective. *Energy Policy* **1996**, *24* (1), 31–37.

(11)   Hallegatte, S.; Rogelj, J.; Allen, M.; Clarke, L.; Edenhofer, O.; Field, C. B.; Friedlingstein, P.; Van Kesteren, L.; Knutti, R.; Mach, K. J. Mapping the Climate Change Challenge. *Nat Clim Chang* **2016**, *6* (7), 663–668.

(12)   Karl, T. R.; Melillo, J. M.; Peterson, T. C. *Global Climate Change Impacts in the United States: A State of Knowledge Report from the US Global Change Research Program*; Cambridge University Press, 2009.

(13)   Shakun, J. D.; Clark, P. U.; He, F.; Marcott, S. A.; Mix, A. C.; Liu, Z.; Otto-Bliesner, B.; Schmittner, A.; Bard, E. Global Warming Preceded by Increasing Carbon Dioxide Concentrations during the Last Deglaciation. *Nature* **2012**, *484* (7392), 49–54.

(14)   Andrew, R. M. Global CO 2 Emissions from Cement Production. *Earth Syst Sci Data* **2018**, *10* (1), 195–217.

(15)   Li, C.; Gong, X. Z.; Cui, S. P.; Wang, Z. H.; Zheng, Y.; Chi, B. C. CO2 Emissions Due to Cement Manufacture. In *Materials Science Forum*; Trans Tech Publ, 2011; Vol. 685, pp 181–187.

(16)   Shen, W.; Cao, L.; Li, Q.; Zhang, W.; Wang, G.; Li, C. Quantifying CO2 Emissions from China's Cement Industry. *Renewable and Sustainable Energy Reviews* **2015**, *50*, 1004–1012.

(17)   Tubiello, F. N.; Salvatore, M.; Rossi, S.; Ferrara, A.; Fitton, N.; Smith, P. The FAOSTAT Database of Greenhouse Gas Emissions from Agriculture. *Environmental Research Letters* **2013**, *8* (1), 015009.

(18)   Shirani, S.; Cuesta, A.; Morales-Cantero, A.; Santacruz, I.; Diaz, A.; Trtik, P.; Holler, M.; Rack, A.; Lukic, B.; Brun, E. 4D Nanoimaging of Early Age Cement Hydration. *Nat Commun* **2023**, *14* (1), 2652.

(19)   Ashby, M. F. *Materials and the Environment: Eco-Informed Material Choice*; Elsevier, 2012.

(20)   Katsiki, A. Aluminosilicate Phosphate Cements–a Critical Review. *Advances in Applied Ceramics* **2019**, *118* (5), 274–286.

(21)   Kim, Y.; Worrell, E. International Comparison of CO2 Emission Trends in the Iron and Steel Industry. *Energy Policy* **2002**, *30* (10), 827–838.

(22)   Lothenbach, B.; Scrivener, K.; Hooton, R. D. Supplementary Cementitious Materials. *Cem Concr Res* **2011**, *41* (12), 1244–1256.

(23)   Lothenbach, B.; Le Saout, G.; Gallucci, E.; Scrivener, K. Influence of Limestone on the Hydration of Portland Cements. *Cem Concr Res* **2008**, *38* (6), 848–860.

(24)   Bazzoni, A.; Ma, S.; Wang, Q.; Shen, X.; Cantoni, M.; Scrivener, K. L. The Effect of Magnesium and Zinc Ions on the Hydration Kinetics of C3S. *Journal of the American Ceramic Society* **2014**, *97* (11), 3684–3693.

(25)   Li, X.; Scrivener, K. L. Impact of ZnO on C3S Hydration and CSH Morphology at Early Ages. *Cem Concr Res* **2022**, *154*, 106734.

(26)   Ouzia, A.; Scrivener, K. The Needle Model: A New Model for the Main Hydration Peak of Alite. *Cem Concr Res* **2019**, *115*, 339–360.

(27)   Kumar, A.; Walder, B. J.; Kunhi Mohamed, A.; Hofstetter, A.; Srinivasan, B.; Rossini, A. J.; Scrivener, K.; Emsley, L.; Bowen, P. The Atomic-Level Structure of Cementitious Calcium Silicate Hydrate. *The Journal of Physical Chemistry C* **2017**, *121* (32), 17188–17196.

(28)   Harris, M.; Simpson, G.; Scrivener, K.; Bowen, P. A Method for the Reliable and Reproducible Precipitation of Phase Pure High Ca/Si Ratio (> 1.5) Synthetic Calcium Silicate Hydrates (CSH). *Cem Concr Res* **2022**, *151*, 106623.

(29)   Carino, A.; Testino, A.; Andalibi, M. R.; Pilger, F.; Bowen, P.; Ludwig, C. Thermodynamic-Kinetic Precipitation Modeling. A Case Study: The Amorphous Calcium Carbonate (ACC) Precipitation Pathway Unravelled. *Cryst Growth Des* **2017**, *17* (4), 2006–2015.

Contents

Chapter 2: State of the Art

This chapter looks at the most relevant publications for this thesis. It is divided into five sections to give the necessary background on synthetic C-S-H and the importance of understanding zinc incorporation. The sections start more general and go to more specific: 2.1) Hydration of Portland Cement, 2.2) What is C-S-H, 2.3) The atomic-level structure of C-S-H, 2.4) C-S-H nucleation and growth, and 2.5) The effect of zinc in cement hydration.

2.1 Hydration of Portland Cement

Portland Cement (PC) is the most common type of cement in general use by far (>99%). It is the main component of concrete, mortar, grout, and stucco. Portland cement is produced by heating ground limestone and clay at about 1450 °C, a process known as clinkering The product of clinkering is clinker, which is an anhydrous mixture of four main phases: alite (an impure form of $3CaO \cdot (SiO_2)$ or C_3S in cement notation), belite (an impure form of $2CaO \cdot (SiO_2)$ or C_2S in cement notation), calcium aluminate $3CaO \cdot (Al_2O_3)$ or C_3A), and ferrite ($4CaO \cdot (Al_2O_3)_x \cdot (Fe_2O_3)_{2-x}$ or C_4AF_{2-x}). Before hydration, clinker is ground with gypsum ($CaSO_4 \cdot 2H2O$), which is added to regulate the reactivity of calcium aluminate during hydration and provide sufficient time before setting and hardening.[1] At this stage, SCMs can be added to replace part of the clinker. When PC is mixed with water, the different phases in the clinker, the SCMs and gypsum dissolve completely or partially and new phases precipitate. The main reactions that participate in cement hydration are described in eq. 1-3.[2]

Hydration of alite
$$C_3S + (3 + x - n)HO \rightarrow C_xSH_n + (3 - x)CH \qquad (1)$$
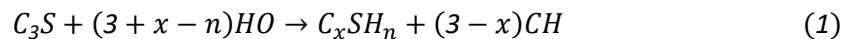
Hydration of belite
$$C_2S + H_2O \rightarrow C - S - H + CH \qquad (2)$$

Effect of gypsum in C_3A hydration
$$C_3A + H_2O + CaSO_4 \rightarrow CAC\underline{S}H_{12} \qquad (3)$$
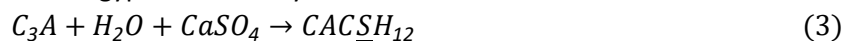
The products of these reactions contain water (H) and are thus known as hydration products. The most relevant hydration products in Portland cement are portlandite ($Ca(OH)_2$), ettringite ($Ca_6Al_2(SO_4)_3(OH)_{12} \cdot 26H_2O$), calcium aluminium iron (AFm) phases and calcium silicate hydrate (C-S-H). The precipitation of the latter, which occurs through the hydration of alite, or C_3S, and belite drives the hydration of cement and plays a major role on the final mechanical properties of cement.[3,4] The general traits and most important information about the cement hydration process will be discussed next, taking Figure 2.1 as reference, which shows a typical calorimetry curve where the heat of reaction is plotted against time.
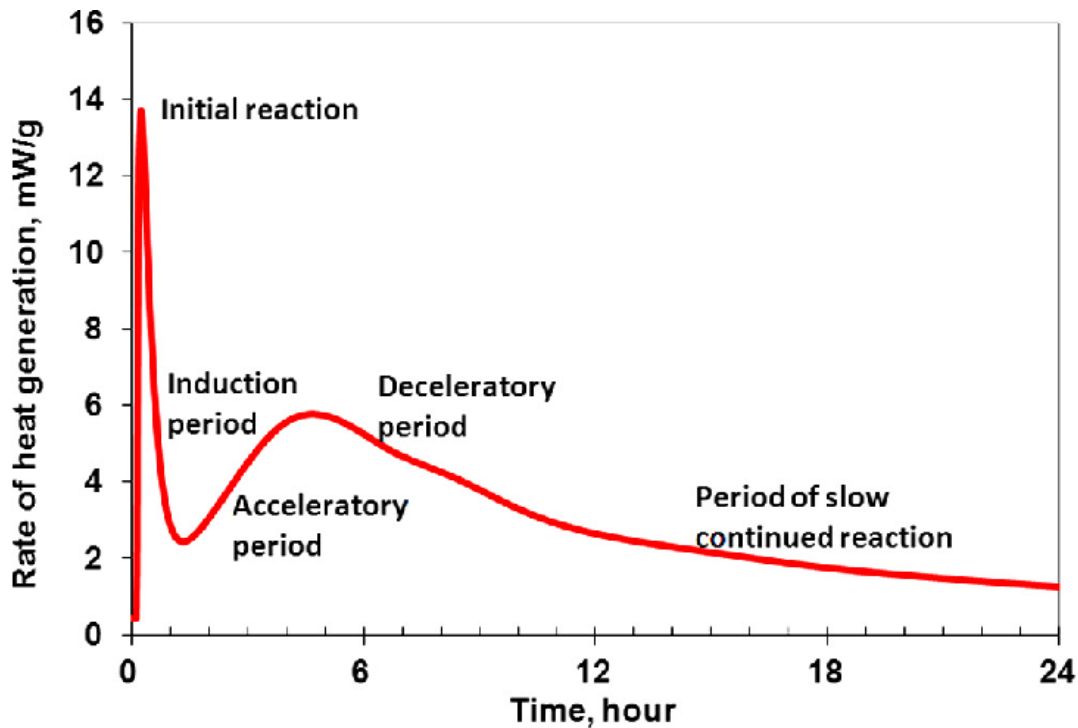
Figure 2.1: Rate of heat generation against time during cement hydration.

The first step in cement hydration occurs when water and cement are mixed. This is known as the **initial period** or *stage 1*, where an acute heat release peak appears immediately after mixing. This peak reflects the reaction between C_3A and water (eq. 3), which produces calcium aluminate hydrate phases. Afterwards, there is an **induction period** which is also known as *stage 2*.

The induction period is important for the transportation of concrete and for its placing before it sets. The absence of gypsum can lead to a rapid setting immediately after mixing, a process known as flash set. This is undesirable and therefore all Portland cement contain around 5% of gypsum.

When the induction period comes to an end, the heat release increases, indicating an acceleration of the reaction. This is known as the **acceleration period** or *stage 3*. Acceleration is mainly due to the reactions of C_3S with water and is dominated by the precipitation and growth of C-S-H (eq. 1 and 2), which accounts for ca. 60% of the cement's final volume, making it the most abundant hydration product. In addition, some additives, such zinc oxide, have been shown to delay the acceleration period but also to increase the heat release. These substances are called "delayed accelerators" and are of potential interest since higher heat release rates are related to higher early age strength properties. Understanding the growth mechanisms of C-S-H and its atomic-level structure when it coprecipitates with zinc, a delayed accelerator, is a major goal in this thesis.

A maximum rate is reached, and the reaction slows down. This reduction in heat release and reaction rate marks what is known as **deceleration period** or *stage 4*.

12

Understanding the underlying mechanisms that have a role in cement hydration and how they affect the final properties of cement is of vital importance to make cost-effective, high-quality, and environmentally friendly cementitious materials. As stated previously, the focus of this thesis revolves around understanding the role of zinc, a delayed accelerator, in cement hydration, for reasons that will be discussed later (section 1.4). However, studying these processes is difficult since cement is a complex material made of many different phases. That is why this work will be centered around the formation of pure C-S-H only, which drives the hydration's acceleration period, and won't consider other participating phases like aluminates or gypsum.

2.2 What is C-S-H?: a not-so-easy question

2.2.1 Introduction to C-S-H

C-S-H is the major hydration product in Portland Cement, and it accounts for up to 60% of its final volume. It is obtained through the hydration of C_3S (alite) and C_2S (belite), but it can also be precipitated synthetically under controlled atmosphere, temperature, and pH conditions.[5,6] Because of its ubiquity and relevance to cement hydration, C-S-H has been intensely studied, but the intricacies of this material make it difficult to understand.

The formation of C-S-H in cement is known to be a dissolution-precipitation process where the anhydrous calcium silicates dissolve rapidly releasing Ca and Si species into the pore solution. When the concentration of the system reaches a state of critical supersaturation with respect to C-S-H, the precipitation of this phase is triggered, with the resulting calcium silicate having a lower Ca/Si ratio than C_3S. In addition, the presence of calcium aluminates, fly ash or slag in the clinker, promote the dissolution of aluminum ions and their further incorporation in C-S-H, leading to the formation of C-(A)-S-H. Details and current theories and models on C-S-H precipitation and growth are further discussed in Section 2.3.

The stoichiometry of C-S-H is variable, and it depends on the conditions in which it formed. At standard conditions in cement samples, C-S-H is known to have a Ca/Si ratio higher than 1.5, generally averaging around 1.7.[7] The water content is between 20-44% depending on how the material is dried.[8]

C-S-H has structural order at the short range. However, it lacks a long-range order or periodicity which makes it difficult to analyze with techniques such as X-Ray Diffraction (XRD) or electron diffraction. Studying C-S-H at the atomic level then requires other characterization techniques that do not rely on crystallinity such as X-ray absorption spectroscopy (XAS), small-angle X-ray scattering (SAXS), or nuclear magnetic resonance (NMR).

Morphologically Calcium silicate hydrate in cement is divided into inner product C-S-H, which forms on the place of the reacting alite grain and outer product C-S-H. which forms in the originally water filled space.[9] Outer C-S-H forms during early stages of hydration and grows away from the anhydrous particle. Inner C-S-H forms during late stages of hydration.[10]
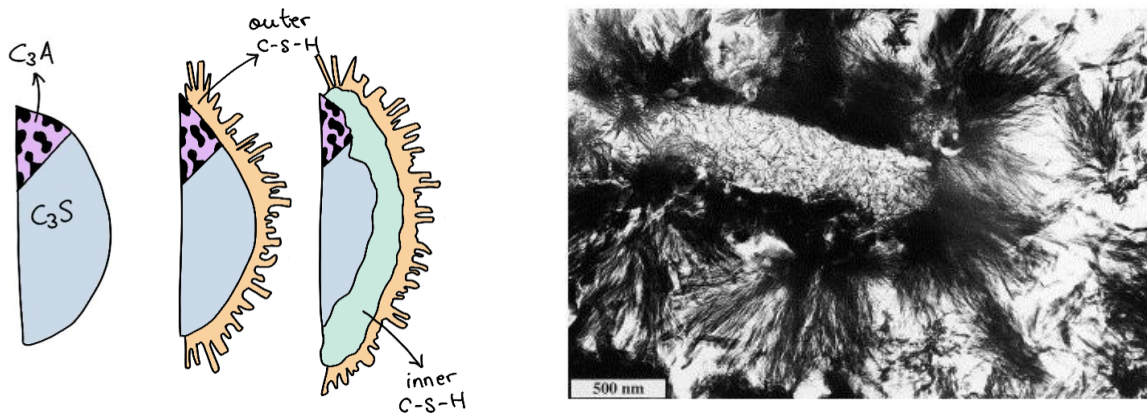
Figure 2.2: Left) a schematic representation of the growth process of outer and inner C-S-H, where the growth of AFt phases has been omitted. Right) a TEM micrograph showing a low-density inner product surrounded by a rim of relatively dense C-S-H and fibrillar outer product C-S-H in a mature Portland cement paste (from Richardson et al).[11]

2.2.2 Synthetic C-S-H

The presence of many diverse phases in cementitious samples makes it difficult to study C-S-H on its own. Thermodynamic and kinetic experiments, as well as spectroscopies, are better applied to pure phases. Because of this, there have been several attempts to synthesize pure-phase C-S-H under controlled lab conditions. The resulting material is what is known as **synthetic C-S-H**.

Over the past two decades, synthetic C-S-H precipitation has been able to produce calcium silicate hydrates with a maximum Ca/Si ratio of 1.5, which falls below the Ca/Si ratio found in cement samples (1.7). Two methods have been commonly used to produce synthetic C-S-H: the reaction between CaO or Ca(OH) and reactive silica[12–15] and the double decomposition of sodium silicate with a calcium salt as in the works from Martín-Garrido et al.[16] and Chen et al.[13] The latter, however, resulted in the coprecipitation of both C-S-H and Portlandite, which is undesired.

Kumar et al.[6] were the first succeeded in making single pure-phase synthetic C-S-H with Ca/Si ratios up to 2. In this work a dropwise precipitation was used, in which a sodium metasilicate solution is titrated into a calcium nitrate solution (or vice versa) in well-mixed, controlled pH and temperature conditions. Further thermodynamic and kinetic modeling by Andalibi et al.[17,18] proved that controlling pH and temperature is key to ensure high Ca/Si ratios with this methodology. Additionally, the dropwise precipitation method can ensure that the solution never becomes supersaturated with respect to Portlandite, allowing for the precipitation of only pure-phase synthetic C-S-H. The dropwise C-S-H precipitation method was then refined by Harris et al.[5] whose work focused on perfecting a reliable method to produce single-phase C-S-H of the desired Ca/Si ratio by controlling the reactant concentrations, the mixing conditions, temperature, and the pH of the system.

The set-up used by Harris et al.[5] consists of a poly(methyl metacrylate) (PMMA) batch reactor with a lid that has slots for the different measurements that can be carried out during precipitation. Two of the slots have glass inlet and outlet tubes to allow for a gas purge using N_2. A pH meter which also makes temperature measurements occupies one of the slots. The system has a 3-input micromixer on top; and a magnetic stirring bar is added at the bottom of the batch reactor, as is shown in Figure 2.3.
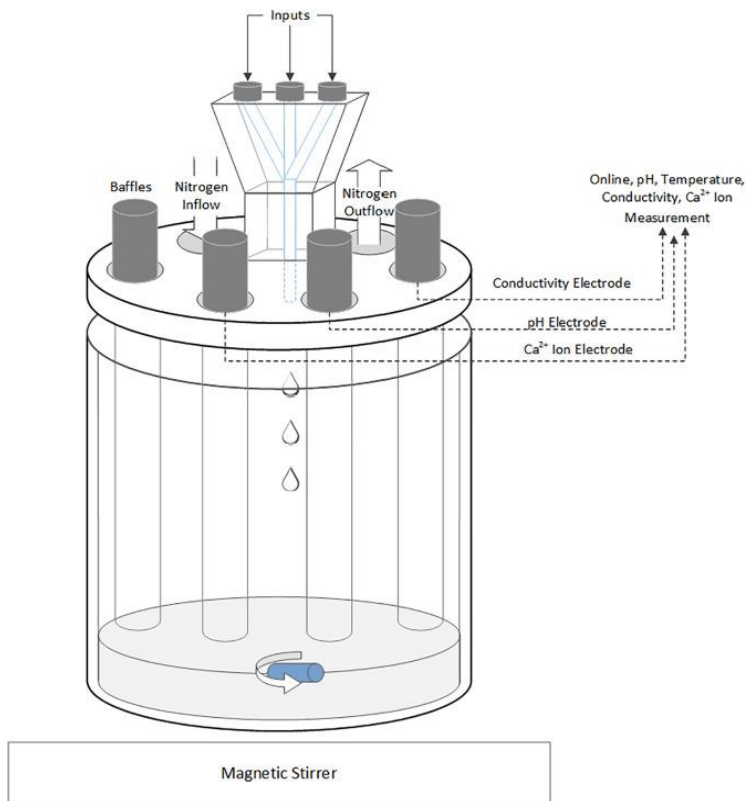
Figure 2.3: Schematic representation of the experimental set-up used to precipitate C-S-H in a batch reactor.[5]

The precipitation of pure-phase C-S-H is carried out by adding one of the two solutions (sodium metasilicate and calcium nitrate) into the other through the micromixer at a known rate (usually 2 mL/min). A continuous rapid (~3000 rpm) stirring is required to ensure the homogeneity of the reaction; and NaOH is added to achieve the desired pH, which for high Ca/Si ratios (1.5-2.0) ranges from 12.8 to 13.2, approximately. Details on the specific methodology, reactant concentrations and experimental conditions used to precipitate C-S-H for the present work of this thesis will be presented in Chapters 3 and 4, where this method is used experimentally.

2.3 Atomic-level structure of C-S-H

The complex nature of calcium silicate hydrates, combined with their lack of crystallographic long-range order, prevent techniques such as XRD from being able to determine their crystal structure. Nuclear magnetic resonance (NMR) is key when trying to unravel the chemical environments of the different atoms in materials which lack long-range periodicity, which is essential when determining the atomic-level structure of C-S-H.[19]

Because cements are complex materials, there are many nuclei that could be of interest: ^{1}H, ^{13}C, ^{17}O, ^{19}F, ^{23}Na, ^{25}Mg, ^{27}Al, ^{29}Si, ^{31}P, ^{33}S, ^{35}Cl, ^{39}K and ^{43}Ca.[20] For the present work, however, since the focus is put on C-S-H and C-S-H-related phases like C-A-S-H or zinc-modified C-S-H, the nuclei of interest are narrowed down to ^{1}H and ^{29}Si.

2.3.1 Basics of a solid-state NMR experiment

In an NMR experiment, a sample is held in a magnetic field (B0) and is subject to radiofrequency radiation in the form of pulses, which induces the precession of the nuclear spin. The spin relaxes back to align with B0, and the electromagnetic signal of this relaxation is measured as a free induction decay, which becomes an NMR spectrum upon being Fourier transformed. This NMR spectrum shows resonances that are characteristic to the specific chemical environments the atoms of interest are subject to.[21]

The NMR spectra of solid-state samples are broadened when compared to the spectra of solution-state samples. This is due to dipolar interactions, chemical shift anisotropy, shielding and quadrupolar interactions. However, this broadening can be reduced by spinning the sample at what is known as the magic angle, known as **magic angle spinning (MAS)**.[21] Because the nuclear dipolar interaction has a dependency of $3 \cdot cos^2\Theta - 1$, where Θ is the angle between B0 and the sample's rotational axis, the "magic angle" (Θm) which makes the dipolar interaction vanish is:

$$\Theta_m = cos^{-2}\left(\frac{1}{3}\right) = 54.74°$$

Additionally, chemical shielding anisotropy and first-order quadrupolar interaction are also removed, resulting in the narrowing of the spectral lineshapes. Nuclei with spins greater than ½ (like ^{43}Ca, ^{27}Al, ^{17}O and ^{67}Zn), known as quadrupolar nuclei, also experience a second order quadrupolar interaction that results in broader lineshapes, which limits the resolution of these signals; a broadening that can be reduced by using stronger magnetic fields.

All nuclei participating in C-S-H are interesting for the study of these materials, but because it makes up the structural unit of the *dreierketten* chains, **^{29}Si MAS NMR** are the most common NMR experiments conducted in cementitious calcium silicates. Silicate sites in NMR have their own nomenclature, from which the nomenclature of other sites such as aluminum or zinc sites is also derived.

2.3.2 The Q nomenclature

Silicate sites are commonly referred to using a notation of the form: $Q^n(mX)$ with $0 \leq m \leq n \leq 4$, where silicate atoms in tetrahedral coordination are represented by Q and n denotes other tetrahedral atoms coordinated to Q via oxygen bridges (from which m atoms are of element X).[20] In other words, a silicate monomer is a $Q^{(0)}$; a silicon site which is at the end of a *dreierketten* chain and is only connected to another silicate is a $Q^{(1)}$; a silicate connected to two other silicates is a $Q^{(2)}$ ($Q^{(2p)}$ if occupying a pairing site, and $Q^{(2b)}$ if occupying a bridging site); and $Q^{(3)}$ and $Q^{(4)}$ are then silicates connected to three or four other silicates, respectively.

$Q^{(0)}$, $Q^{(1)}$, $Q^{(2)}$ and $Q^{(4)}$ typically resonate in ^{29}Si NMR experiments in the region between -60 ppm to -120 ppm (with respect to tetramethylsilane or TMS), resulting in signals which often present significant overlapping. As the silicate species present higher connectivities, they also show more negative chemical shifts, as is shown in Figure 2.4A. It is also important to note that these typical ranges vary as adjacent silicate groups are substituted by aluminum atoms, a fact that will be important when describing C-A-S-H, later in this section.
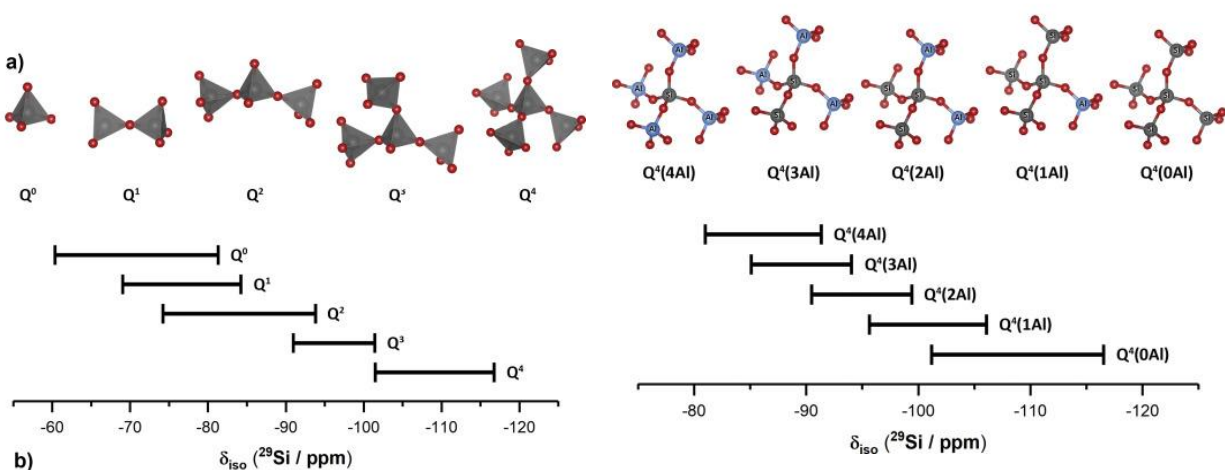
Figure 2.4: A) Typical ^{29}Si chemical shift ranges of silicate species $Q^{(0)}$, $Q^{(1)}$, $Q^{(2)}$, $Q^{(3)}$ and $Q^{(4)}$, and B) typical ^{29}Si chemical shifts of Si-Al $Q^{(4)}$ species.[20]

2.3.3 Determination of the atomic-level structure of C-S-H by means of NMR

There are numerous structural models which have been proposed to explain the atomic-level structure of C-S-H, including those derived from jennite, tobermorite, portlandite, or a combination of these three. However, solid-state ^{29}Si and ^{17}O NMR experiments have shown the structural similarity of calcium silicate hydrate to a defective tobermorite, pushing the research and the new models proposed to be based on this structure, instead of jennite or portlandite.[22] Furthermore, recent work[6] which combines dynamic nuclear polarization (DNP), (^{29}Si)^{29}Si double quantum coherence (the Incredible Natural Abundance Double Quantum Coherence Experiment, INADEQUATE, developed by Bax et al.[23] and adapted to the solid-state by Lesage et al.[24]), (^{1}H)^{29}Si heterocorrelation (HETCOR) NMR, and atomistic modeling,

determined the atomic-level structure of several synthetic C-S-H formulations covering a range of Ca/Si ratios from 1.25 to 2.0. This specific publication is of great interest for the present thesis and will be now discussed in more detail.

Kumar et al.[6] reported not only the first synthesis of pure-phase high Ca/Si ratio (tunable between 1.0 and 2.0) C-S-H, but also solved the three-dimensional structure of these materials with different composition. multiple strategies were used. First, AMUPol is mixed with the C-S-H gel sample to allow for **dynamic nuclear polarization (DNP)**[25,26] upon irradiation with microwaves (MW), a technique used in solid-state NMR to transfer the polarization from a radical to the nuclei of interest and enhance the signal to noise ratio of the spectra. DNP-enhanced **^{29}Si cross-polarization (CP)** MAS experiments were carried out, which were one-dimensional (spin echo) and two-dimensional (2d refocused INADEQUATE).
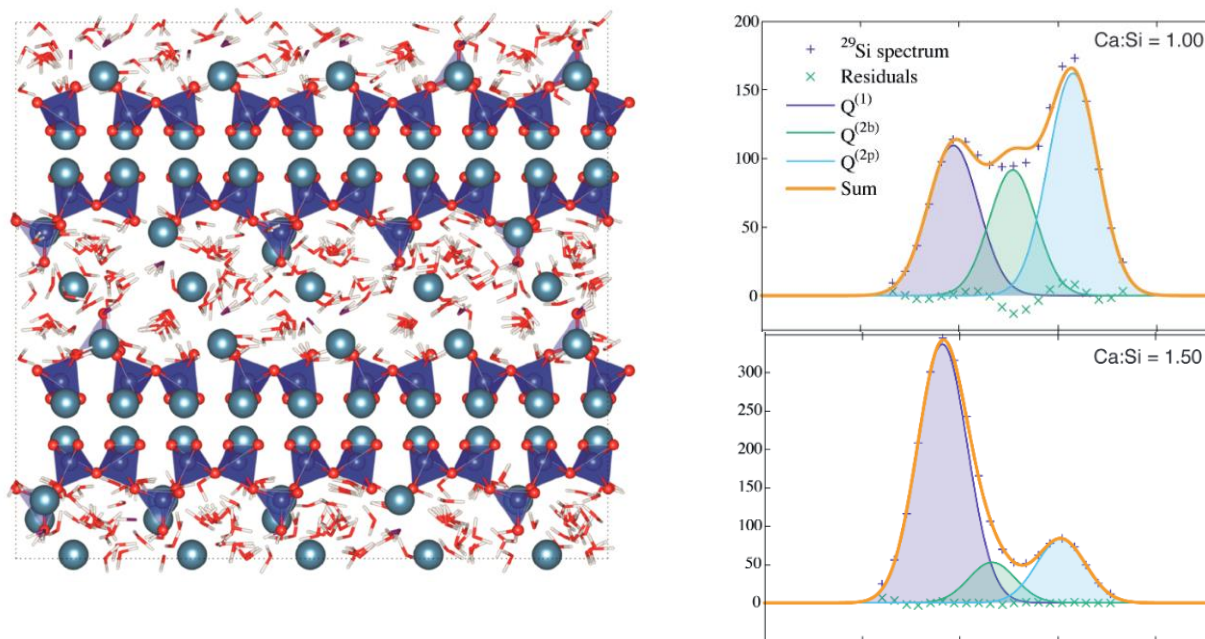
Figure 2.5: A) Atomic-level structure of C-S-H as determined through the brick model and molecular dynamics and B) deconvoluted ^{29}Si NMR spectra of samples with Ca:Si = 1.00 and Ca:Si = 1.50. From Kumar et al.[6]

Deconvolutions of the 1D spectra were used to constrain the 2D deconvolutions of the 2D spectra, which allowed for the quantification of the silicate connectivities (i.e $Q^{(1)}$-$Q^{(1)}$, $Q^{(2p)}$-$Q^{(2p)}$, $Q^{(1)}$-$Q^{(2p)}$ and $Q^{(2p)}$-$Q^{(2b)}$). Additionally, (^{1}H)^{29}Si HETCOR experiments were carried out and used to correlate ^{1}H and ^{29}Si chemical shifts. To determine the atomic-level structure, a model based on defective tobermorite 14 Å was adopted. The defects introduced in the tobermorite structure were removal of SiO_2 units from the bridging site. This picture in combination with the connectivities obtained from the INADEQUATE ^{29}Si MAS NMR experimental analysis, allows for the calculation of *dreierketten* chain distributions and mean chain lengths. These results were then combined with **density functional theory (DFT)**,[27] thanks to which a set of structures were relaxed and compared to the experimental results to allow the determination of the structure of C-S-H with different Ca/Si ratios. Figure 2.5 shows the as-determined structure of C-S-H with

18

Ca/Si ratio of 1.5 (and structures corresponding to other Ca/Si are shown in the Supplementary Information of this publication).

One of the most important conclusions from this work is that as the Ca/Si ratio is increased, calcium atoms are not only found in the interlayer but can occupy the bridging site, replacing $Q^{(2b)}$ species. This calcium site is associated with strong hydrogen bonding which seems to stabilize the C-S-H structure. Additionally, this computational model does not need to invoke other phases like portlandite or Jennite, and shows, once again, that C-S-H can be modeled uniquely by tobermorite 14 Å. These results and model are central for the present work and a similar path will be followed to resolve the structure of zinc-modified C-S-H.

There are many structural models of C-S-H which make use of ^{29}Si NMR experiments in the solid state.[7,20,28] Although results show that C-S-H phases exist with great diversity among different Ca/Si ratios and water content, the chemical shifts corresponding to $Q^{(1)}$, $Q^{(2p)}$ and $Q^{(2b)}$ species seem to not be a matter of discussion, since there is a clear agreement across publications on their assignment; which is always very similar to the deconvolved lineshapes of Figure 2.5B.

Aside from the variety of ^{29}Si NMR experiments on C-S-H, there are other works that aim to resolve the chemical environments of other nuclei present in C-S-H, like ^{17}O or ^{43}Ca. Cong et al.[29,30] carried out ^{17}O NMR experiments, and determined Si-O linkages, in support of the Richardson and Groves tobermorite model. Also, Moudrakovski et al.[31] and Richardson et al.[14,32] found that the coordination of calcium in C-S-H is 6 or 7 thanks to a series of ^{43}Ca NMR experiments. These nuclei are difficult to analyze because they are quadrupolar and have very broad signals, and they almost always require labeling in order to increase the signal to noise ratio, which increases the cost and the experimental times. Despite their difficulty, the experiments carried out on these nuclei are still very relevant to the atomic-level structure, coordination numbers and oxidation states of the atoms that participate in C-S-H.[33]

The presence of various phases and elements during cement hydration promotes the formation of calcium silicate hydrates with incorporated elements such as aluminum or sodium, forming C-A-S-H, (C,N)-A-S-H or N-A-S-H. C-A-S-H is of especial interest for this thesis since it's the results of the incorporation of a metal ion (like zinc) in the C-S-H structure. The means by which the C-A-S-H atomic-level structure is resolved are relevant for the further study of zinc incorporation in C-S-H; hence, the most relevant publications on this topic are discussed below.

2.3.4 Determination of the atomic-level structure of C-(A)-S-H by means of NMR

The incorporation of elements, specifically aluminum, in C-S-H has been a well-researched topic. Studies using ^{29}Si NMR to probe the local structure of C-A-S-H gels are numerous: from those studying this phase in OPC or binary/ternary blends,[34–36] to even in 2000-year-old cements from the Roman Empire.[37]

It has been through ^{29}Si NMR that $Q^{(1)}$, $Q^{(2)}$ and $Q^{(n,mAl)}$ have been resolved and that the calculation of mean chain lengths (MCLs) has been possible. The equation below shows how the MCL can be calculated, extracting all required information from the intensities of the different signals from $Q^{(1)}$, $Q^{(2)}$ and $Q^{(2,Al)}$.[38]

$$MCL_{CASH} = \frac{2[Q^1 + Q^2 + \frac{3}{2}Q^2(Al)]}{Q^1}$$

Interestingly, Richardson et al.[39] used ^{29}Si NMR to resolve the aluminum sites in C-A-S-H and found that Al preferentially substitutes bridging silicates and that the MCL depends on the availability of Al^{3+} ions and hydration time; these findings were later confirmed by Andersen, Jakobsen and Skibsted.,[28,40,41] whose extensive work on ^{29}Si NMR and ^{27}Al NMR has allowed the community to understand the types of aluminum involved in C-A-S-H (AlIV, AlV, AlVI).

Recent work on synthetic C-A-S-H by Kunhi et al.[38] which combines the brick computational model developed by Kunhi et al.,[38] ^{29}Si and ^{27}Al NMR, and DFT-calculated chemical shifts (see Figure 2.6), to resolve the atomic-level structure of C-A-S-H with great level of detail. Particularly, (^{29}Si)^{27}Al heterocorrelation experiments showed that while aluminum substitutes for the bridging site in all coordinations, tetrahedral Al(IV) species are favored at low Ca/Si (<1.5), at higher calcium content, Al(V) and Al(VI) species overtake Al(IV) (always considering that there are enough hydroxyl groups). With hydroxyl availability increasing with additional water and calcium in the interlayer, bridging species become the most stable, hence supporting this Al(VI) bridging theory. Figure 2.6 shows the as-determined C-A-S-H structure for a sample with stoichiometry $(CaO)_{1.7}(Al_2O_3)_{0.05}SiO_2(H_2O)_{1.9}$. This work has also been supported by Yang et al.,[42] who studied the incorporation of both sodium and aluminum in C-A-S-H phases through ^{23}Na, ^{27}Al, and ^{29}Si MAS NMR.
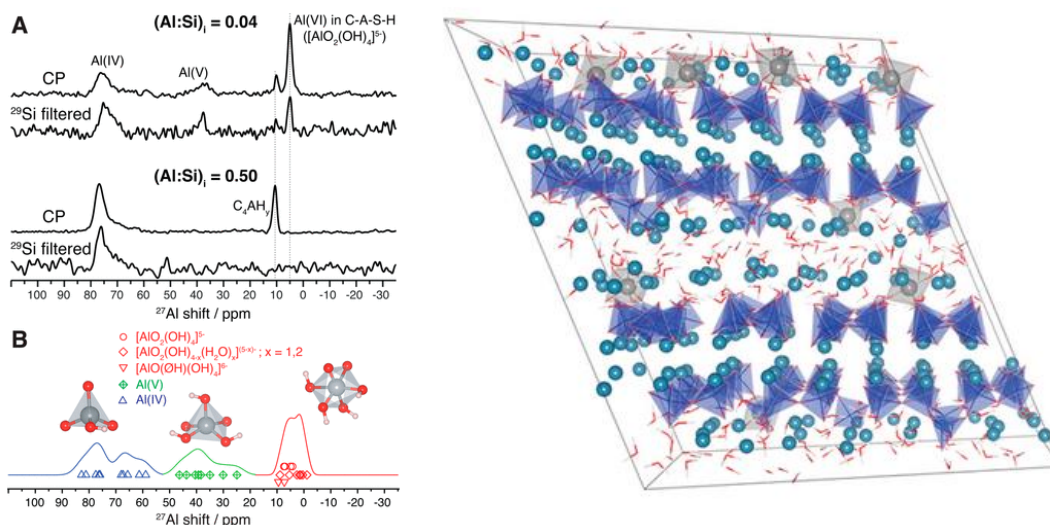
Figure 2.6: A) ^{27}Al NMR spectra of samples with (Al:Si)$_i$=0.04 and (Al:Si)$_i$=0.50. B) DFT-simulated ^{27}Al chemical shifts. C) Atomic-level structure of C-A-S-H as determined by Kunhi et al.[38]

The structures of both C-S-H and C-A-S-H determined through means of dropwise synthetic precipitation, NMR and computational methods, and the publications discussed in this section are of great interest for this thesis, especially the ones from Kumar et al. and Kunhi et al.[38] since similar experimental routes will be followed to determine how zinc incorporates in the C-S-H structure.

Despite structural determination being a quest on its own, there is another objective to be aimed at during this work, and that is thermodynamic and kinetic modelling of synthetic C-S-H precipitation, as previously mentioned during the introduction. Let's then review the most relevant publications that will set the base of C-S-H and zinc-modified C-S-H modelling with respect to nucleation and growth.

2.4 Nucleation and growth of C-S-H

It comes as no surprise upon reading this chapter that C-S-H is not only elusive in regard to its structure, but also when it comes to its nucleation and growth mechanisms. The interest in its thermodynamic and kinetic behavior revolves around the fact that it drives cement hydration and is responsible for the final strength of the hardened cement thanks to its percolating network. Understanding how C-S-H, the main hydration product, initiates its formation and precipitation, and how it grows is key for fine tuning of the final cement properties. Because of this, there have been many attempts to propose models to describe these underlying mechanisms.

2.4.1 Existing thermodynamic-kinetic works on C-S-H

In the past decade, the early stages of crystallization in a wide range of materials have gained a great research interest. Many of these researchers consider non-classical pathways, which differ from classical nucleation theory by including the formation of precursors and pre-nucleation clusters, and are now often used to describe the majority of materials.[43,44] For the interested reader, Karthika et al.[44] published a review on classical and non-classical two-step nucleation pathways that helps understanding the view of the current state of the art on this matter. Regarding the nucleation and growth mechanisms of C-S-H, there are three publications which are important to address. These are the works of Garrault-Gauffinet and Nonat,[45] Krautwurst et al.[46,47] and Andalibi et al.[17]

First, Garrault-Gauffinet and Nonat made conductivity measurements during the formation of C-S-H in solutions with different supersaturation levels with respect to this phase.[45] Although a model was not provided at the time, the conclusions from this experimental analysis were of great importance and a much necessary starting point. They found that C-S-H nucleation follows the general laws of nucleation, that the degree of supersaturation is the main parameter governing homogeneous nucleation rates, and the lime concentration also controls the characteristics of heterogeneous nucleation.

Second, in her thesis and publication, Nina Krautwurst used time-resolved potentiometry, turbidimetry experiments, dynamic light scattering (DLS), small-angle X-ray scattering (SAXS), and cryo-TEM to conclude that C-S-H has a two-step non-classical nucleation pathway. According to their results, the first step consists of the formation of amorphous and dispersed C-S-H spheroids, sometimes referred to as

globular C-S-H.[48] This phase has lower Ca/Si ratios and evolves through time. In the second step, these spheroids crystallize into higher Ca/Si ratio tobermorite-like C-S-H.

Experiments trying to elucidate the nucleation pathway of C-S-H and better grasp its complexity are really important. However, further interpretation of these results through thermodynamic and kinetic modelling is crucial in order to extract important data like solubility constants, surface energies or nucleation and growth rates. This is no easy task, for it requires deep understanding of the laws governing the precipitation and crystallization processes and making a number of assumptions. Andalibi et al.[17] made an important breakthrough in this regard. They developed a thermodynamic-kinetic model with a population balance approach. This model, which embraces primary nucleation, secondary nucleation and molecular growth, is regressed and fitted to experimental calcium concentrations, as is shown in Figure 2.7. These experiments are very similar to the dropwise precipitation method used by both Kumar et al. and Harris et al., with the particularity of the sodium metasilicate solution being titrated into the calcium nitrate solution. This model was able to describe the evolution of calcium activity in an experiment where sodium metasilicate is poured into a calcium nitrate solution and which resulted in C-S-H with a Ca:Si ratio of 2.

One of the most important characteristics of Andalibi's model is that it assumes C-S-H crystallites to be cuboids of adjustable aspect ratios with three dimensions (L_c x arL_c x arL_c, with variable ar), where the internal coordinate that is tracked over time in the model is L_c.
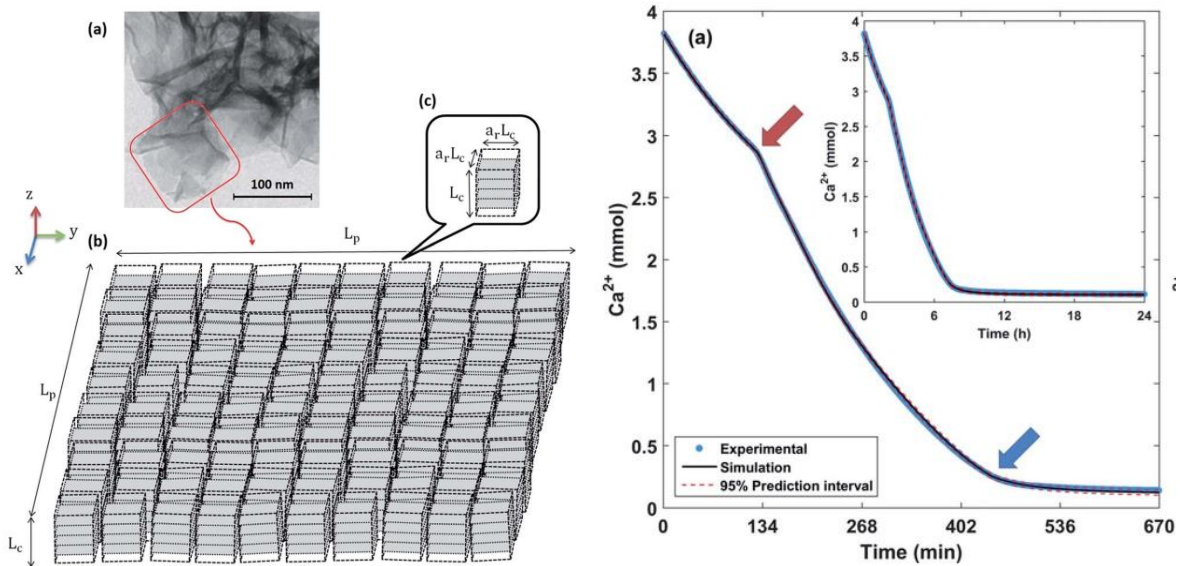
Figure 2.7: A) Schematic representation of how the model described in Andalibi et al.[17] assumes cuboids to describe C-S-H. B) Simulated Ca^{2+} concentration data overlaid on the experimental data.

Other features which are important to mention about this model is that it assumes Kersten's definition of solubility,[49] and that it optimizes a set of population balance ordinary differential equations through a MATLAB code. The model can correctly predict when the precipitation of C-S-H occurs and to estimate

the cohesion energy between crystallites (46 mJ/m2), and activation free energies (120 kJ for primary nucleation and 70 kJ for secondary nucleation). The MATLAB-based code is powerful and able to describe a lot of the features in C-S-H precipitation, but we will now discuss a couple of publications which set the framework that will be used during this thesis in order to develop a new model for C-S-H precipitation which is faster, describes the system during longer equilibration times, and models the reverse titration, in which the calcium nitrate is added to the sodium metasilicate. This is the model developed by Carino, Testino and co-workers.[50]

2.4.2 A relevant thermodynamic-kinetic model: Amorphous Calcium Carbonate

The thermodynamic-kinetic model which is going to be discussed now is not a C-S-H model. However, it is still relevant in the sense that it is extremely comprehensive and can potentially be extended to the calcium silicate hydrate system. Hence, it is worth mentioning and discussing.

In their work, Carino and coworkers[50] collected calcium $[Ca^{2+}]$ activity data as amorphous calcium carbonate (ACC) formed from a dilute solution. Data sets at different temperatures portray the evolution of the calcium signal from an electrode (later transformed into activity or molality) over time as the events of nucleation, precipitation and growth occur. An example of this is shown in Figure 2.8.A, where ACC formed at 298.15 K and pH 9.00.
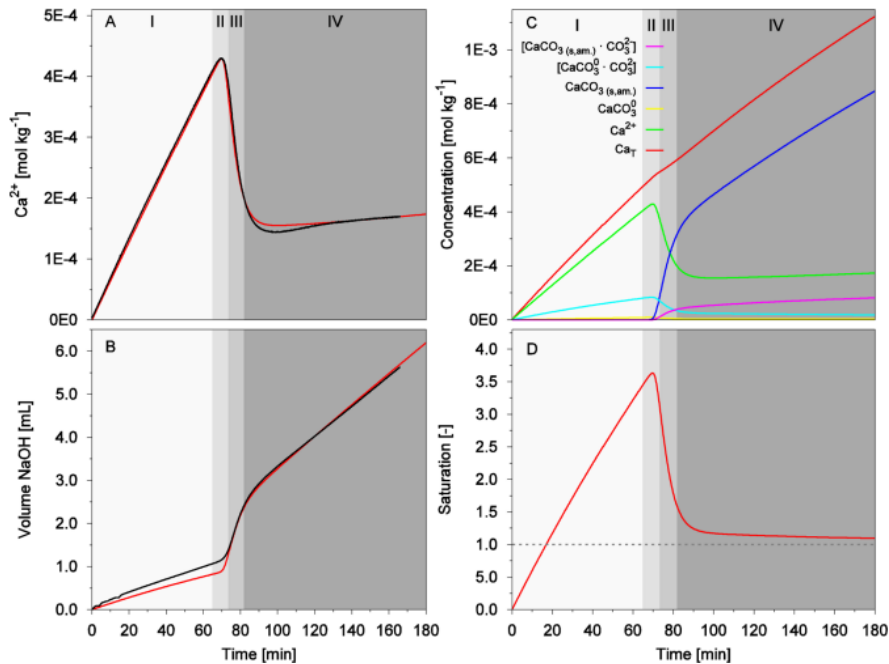
Figure 2.8: Summary of the modelling carried out by Carino et al.[50]

Their thermodynamic model is based on classical nucleation theory equations, including homogeneous and "true" secondary nucleation, as well as diffusion limited processes which influence the growth rate among other parameters. The model embraces thermodynamic and kinetic modeling with a code that

23

was developed in FORTRAN which can solve for relevant thermodynamic information such as speciation, the saturation (Figure 2.8.D), the ionic strength, the total volume and added NaOH volume at any given moment in time. Additionally, the model also tracks nucleation and growth rates over time as well as particle sizes. Results show how this work can not only model the precipitation of ACC but also fit parameters like surface energy and solubility products, which can then be estimated with this model. Further details on the actual modelling and the different data sets and fits for different temperatures and pH can be found in the Supporting Information of this publication.[50]

This model, which comprehensively describes the formation of ACC, is not far from our material of interest: synthetic C-S-H. Both systems are based on a dropwise precipitation in which [Ca^{2+}] can be monitored through ion-selective electrodes (ISE). Despite their obvious differences regarding their morphologies and composition, the case study of ACC can be of great help when building a comprehensive thermodynamic and kinetic model for C-S-H. A similar approach has been successfully applied in the case of calcium phosphates formation from solution[51] and recently also in the case of Aft-Afm phases[*].

Having reviewed and discussed the work carried out by many researchers about the structure and the nucleation and growth mechanisms of C-S-H, let's review the state of the art on zinc incorporation in this phase, which is the main focus of the work presented here.

2.5 Zinc incorporation in C-S-H

Zinc (Zn) is the chemical element with atomic number 30. It is situated in group 12 (IIB) and period 4 in the periodic table and has electron configuration [Ar]$4s^2 3d^{10}$. Its normal oxidation state is Zn^{2+} and can be commonly found in solution as Zn^{2+}, $Zn(OH)^+$, $Zn(OH)$, $Zn(OH)_3^-$ and $Zn(OH)_4^{2-}$, depending on temperature and pH conditions. It is present in Earth's crust, making up 0.0075% of it, which makes it the 24th most abundant element.

Despite it not being a very abundant material on Earth, zinc can be recovered from waste streams. A comprehensive overview on the recovery of zinc and its economic and life cycle feasibility was published by Siew Ng et al.[52] and the interested reader is encouraged to glance at their results. In summary, research and technology must and are shifting towards a resource recovery system in which heavy metals such as zinc are recovered from spent batteries, industrial wastewaters, demolition and construction sites, and the steelmaking industry.

In the present work, we focus on the incorporation of zinc in C-S-H for its enhancing effect on the hydration peak and mechanical properties of cement and explore the importance of using this precious material at the fundamental level. The implementation of zinc in cementitious systems as a standard, however, will require a comprehensive life cycle analysis for the specific case of zinc-modified cements.

---

[*] Unpublished work.

2.5.1 The effect of zinc on C_3S and alite hydration

Several works over the last two decades have demonstrated the effect of adding zinc (in the form of zinc oxide, mainly) in cement hydration. Small amounts of ZnO have proven to enhance the early hydration.[53–55] The research on C_3S and C-S-H and their importance on cement hydration has led to recent studies on the effect of zinc in these specific phases.

Bazzoni et al.[56] studied the hydration of C_3S in the presence of zinc and found that zinc not only incorporated in C-S-H homogeneously, but also increased the maximum heat release by a factor of 2 while the needles of the resulting hydrate grew longer. Figure 2.9 shows a TEM micrograph progression of samples at different stages of hydration without and with zinc.

A more recent study by Li et al.[57] about the hydration of C_3S in presence of ZnO, proved once again that zinc promotes a higher degree of hydration, longer needles, and enhanced compressive early age strength (which is a desirable feature since it allows of a faster workable strength, lower concrete consumption, and improved service of life structure).
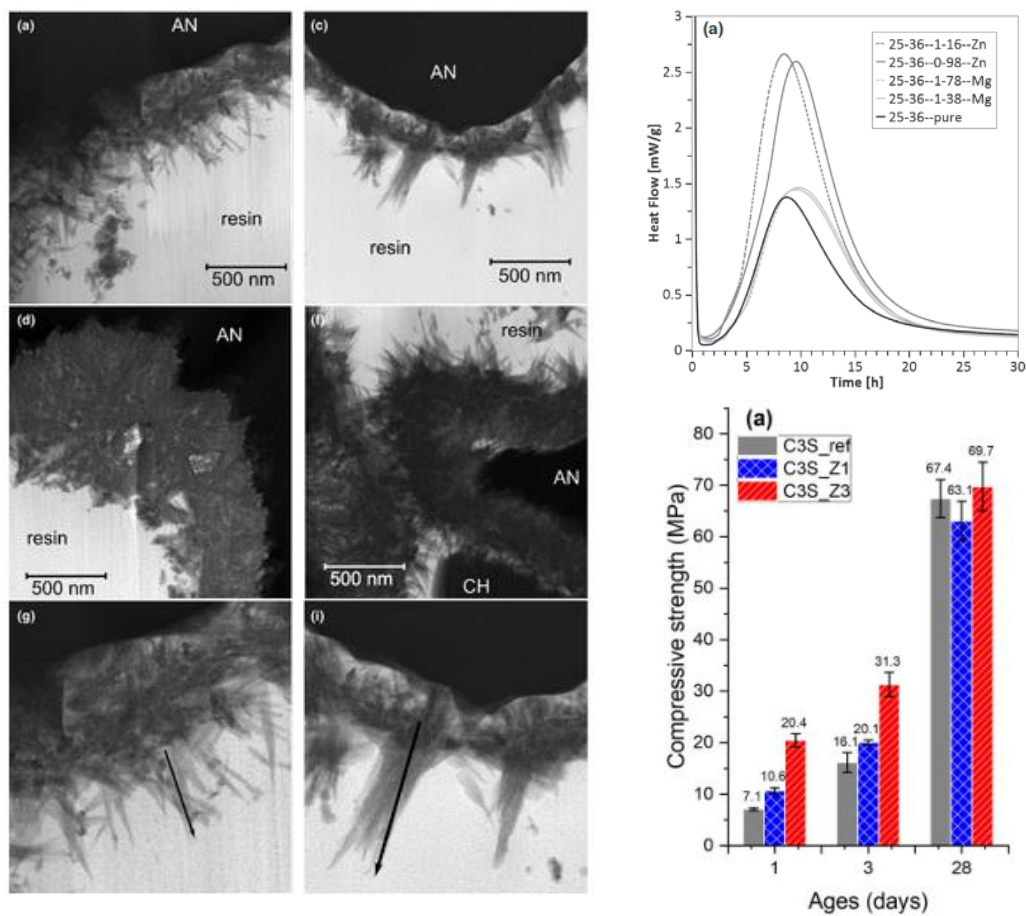
Figure 2.9: A) A series of TEM micrographs showing the growth of C-S-H "needles" in absence (left column) and presence (right column) of zinc.[56] B) Heat flow during hydration of C_3S with and without zinc. C)

Compressive strength of C$_3$S samples without (grey) and with a lower (blue) and a higher (red) content of zinc.[57]

Interestingly, the results from Bazzoni et al.[56] were incorporated in Alexandre Ouzia's "needle" model,[58] which embraces the idea that the heat release curve during hydration can be modelled assuming that C-S-H grows outward from an alite grain as needles. This model, which is not discussed here in detail as it belongs more to C$_3$S and alite modelling rather than synthetic C-S-H, successfully predicted the heat release behavior during the hydration of samples with and without zinc.
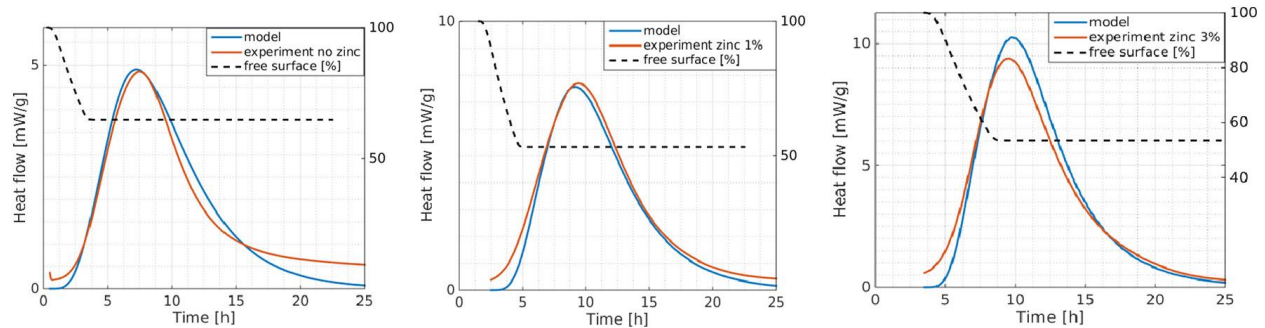
Figure 2.10: Experimental and calculated (needle model) heat flow of C$_3$S samples with A) 0% zinc, B) 1% zinc, and C) 3% zinc content by weight.[58]

With zinc becoming a potential enhancer of cement hydration, and with many of its effects and incorporation mechanisms still elusive, new research is pushed towards understanding the role of zinc in cement. Since C-S-H is agreed to be of utmost importance in cement hydration and strength properties, it seems like a natural path to follow to study the effect and the role of zinc in pure-phase cementitious calcium silicate hydrate. In the following chapters, the determination of the atomic-level structure of zinc-modified C-S-H (Chapter 3) will be discussed and to a preliminary thermodynamic and kinetic model for the nucleation and growth of C-S-H will be designed and built (Chapter 4).

2.6 References

(1) Bullard, J. W.; Jennings, H. M.; Livingston, R. A.; Nonat, A.; Scherer, G. W.; Schweitzer, J. S.; Scrivener, K. L.; Thomas, J. J. Mechanisms of Cement Hydration. *Cem Concr Res* **2011**, *41* (12), 1208–1223.

(2) Mindess, S.; Young, J. F.; Darwin, D. Concrete Prentice-Hall. *Englewood Cliffs, NJ* **1981**, *481*, 939.

(3) Scrivener, K.; Ouzia, A.; Juilland, P.; Mohamed, A. K. Advances in Understanding Cement Hydration Mechanisms. *Cem Concr Res* **2019**, *124*, 105823.

(4) Scrivener, K. L.; Juilland, P.; Monteiro, P. J. M. Advances in Understanding Hydration of Portland Cement. *Cem Concr Res* **2015**, *78*, 38–56.

(5) Harris, M.; Simpson, G.; Scrivener, K.; Bowen, P. A Method for the Reliable and Reproducible Precipitation of Phase Pure High Ca/Si Ratio (> 1.5) Synthetic Calcium Silicate Hydrates (CSH). *Cem Concr Res* **2022**, *151*, 106623.

(6) Kumar, A.; Walder, B. J.; Kunhi Mohamed, A.; Hofstetter, A.; Srinivasan, B.; Rossini, A. J.; Scrivener, K.; Emsley, L.; Bowen, P. The Atomic-Level Structure of Cementitious Calcium Silicate Hydrate. *The Journal of Physical Chemistry C* **2017**, *121* (32), 17188–17196.

(7) Nonat, A. The Structure and Stoichiometry of C-S-H. *Cem Concr Res* **2004**, *34* (9), 1521–1528. https://doi.org/10.1016/j.cemconres.2004.04.035.

(8) Bellmann, F.; Scherer, G. W. Analysis of CSH Growth Rates in Supersaturated Conditions. *Cem Concr Res* **2018**, *103*, 236–244.

(9) Rayment, D. L.; Majumdar, A. J. The Composition of the CSH Phases in Portland Cement Pastes. *Cem Concr Res* **1982**, *12* (6), 753–764.

(10) Groves, G. W. TEM Studies of Cement Hydration. *MRS Online Proceedings Library (OPL)* **1986**, *85*, 3.

(11) Richardson, I. G. The Nature of CSH in Hardened Cements. *Cem Concr Res* **1999**, *29* (8), 1131–1147.

(12) Kunther, W.; Ferreiro, S.; Skibsted, J. Influence of the Ca/Si Ratio on the Compressive Strength of Cementitious Calcium–Silicate–Hydrate Binders. *J Mater Chem A Mater* **2017**, *5* (33), 17401–17412.

(13) Chen, J. J.; Thomas, J. J.; Taylor, H. F. W.; Jennings, H. M. Solubility and Structure of Calcium Silicate Hydrate. *Cem Concr Res* **2004**, *34* (9), 1499–1519.

(14) Tajuelo Rodriguez, E.; Richardson, I. G.; Black, L.; Boehm-Courjault, E.; Nonat, A.; Skibsted, J. Composition, Silicate Anion Structure and Morphology of Calcium Silicate Hydrates (CSH) Synthesised by Silica-Lime Reaction and by Controlled Hydration of Tricalcium Silicate (C3S). *Advances in Applied Ceramics* **2015**, *114* (7), 362–371.

(15) Cong, X.; Kirkpatrick, R. J. 29Si MAS NMR Study of the Structure of Calcium Silicate Hydrate. *Advanced Cement Based Materials* **1996**, *3* (3–4), 144–156.

(16) Martín-Garrido, M.; Martínez-Ramírez, S. CO 2 Adsorption on Calcium Silicate Hydrate Gel Synthesized by Double Decomposition Method. *J Therm Anal Calorim* **2021**, *143*, 4331–4339.

(17) Andalibi, M. R.; Kumar, A.; Srinivasan, B.; Bowen, P.; Scrivener, K.; Ludwig, C.; Testino, A. On the Mesoscale Mechanism of Synthetic Calcium-Silicate-Hydrate Precipitation: A Population Balance Modeling Approach. *J Mater Chem A Mater* **2018**, *6* (2), 363–373. https://doi.org/10.1039/c7ta08784e.

(18) Andalibi, M. R.; Bowen, P.; Carino, A.; Testino, A. Global Uncertainty-Sensitivity Analysis on Mechanistic Kinetic Models: From Model Assessment to Theory-Driven Design of Nanoparticles. *Comput Chem Eng* **2020**, *140*, 106971.

(19) Cong, X.; Kirkpatrick, R. J.; Yarger, J. L.; McMillan, P. F. The Structure of Calcium Silicate Hydrate: NMR and Raman Spectroscopic Results. *Nuclear magnetic resonance spectroscopy of cement-based materials* **1998**, 143–158.

(20) Walkley, B.; Provis, J. L. Solid-State Nuclear Magnetic Resonance Spectroscopy of Cements. *Mater Today Adv* **2019**, *1*, 100007.

(21) Keeler, J. *Understanding NMR Spectroscopy*; John Wiley & Sons, 2010.

(22) Duque-Redondo, E.; Bonnaud, P. A.; Manzano, H. A Comprehensive Review of CSH Empirical and Computational Models, Their Applications, and Practical Aspects. *Cem Concr Res* **2022**, *156*, 106784.

(23) Bax, R. Freeman, and TA Frenkiel. *J. Am. Chem. Soc* **1981**, *103* (2), 69–82.

(24) Lesage, A.; Bardet, M.; Emsley, L. Through-Bond Carbon-Carbon Connectivities in Disordered Solids by NMR. *J Am Chem Soc* **1999**, *121* (47), 10987–10993. https://doi.org/10.1021/ja992272b.

(25) Abraham, M.; McCausland, M. A. H.; Robinson, F. N. H. Dynamic Nuclear Polarization. *Phys Rev Lett* **1959**, *2* (11), 449.

(26) Maly, T.; Debelouchina, G. T.; Bajaj, V. S.; Hu, K.-N.; Joo, C.-G.; Mak–Jurkauskas, M. L.; Sirigiri, J. R.; Van Der Wel, P. C. A.; Herzfeld, J.; Temkin, R. J. Dynamic Nuclear Polarization at High Magnetic Fields. *J Chem Phys* **2008**, *128* (5).

(27) Engel, E. *Density Functional Theory*; Springer, 2011.

(28) Andersen, M. D.; Jakobsen, H. J.; Skibsted, J. Incorporation of Aluminum in the Calcium Silicate Hydrate (C− S− H) of Hydrated Portland Cements: A High-Field 27Al and 29Si MAS NMR Investigation. *Inorg Chem* **2003**, *42* (7), 2280–2287.

(29) Cong, X.; Kirkpatrick, R. J. 17O and 29Si MAS NMR Study of β–C2S Hydration and the Structure of Calcium-Silicate Hydrates. *Cem Concr Res* **1993**, *23* (5), 1065–1077.

(30) Cong, X.; Kirkpatrick, R. J. 17O MAS NMR Investigation of the Structure of Calcium Silicate Hydrate Gel. *Journal of the American Ceramic Society* **1996**, *79* (6), 1585–1592.

(31) Moudrakovski, I.; Alizadeh, R.; Beaudoin, J. J. Natural Abundance Ultrahig-Field 43Ca Solid-State NMR in Cement. **2010**.

(32) Richardson, I. G.; Skibsted, J.; Black, L.; Kirkpatrick, R. J. Characterisation of Cement Hydrate Phases by TEM, NMR and Raman Spectroscopy. *Advances in Cement Research* **2010**, *22* (4), 233–248.

(33) Bowers, G. M.; Kirkpatrick, R. J. Natural Abundance 43Ca NMR Spectroscopy of Tobermorite and Jennite: Model Compounds for C–S–H. *Journal of the American Ceramic Society* **2009**, *92* (2), 545–548.

(34) Jamsheer, A. F.; Kupwade-Patil, K.; Büyüköztürk, O.; Bumajdad, A. Analysis of Engineered Cement Paste Using Silica Nanoparticles and Metakaolin Using 29Si NMR, Water Adsorption and Synchrotron X-Ray Diffraction. *Constr Build Mater* **2018**, *180*, 698–709.

(35) Fernández, R.; Ruiz, A. I.; Cuevas, J. Formation of CASH Phases from the Interaction between Concrete or Cement and Bentonite. *Clay Miner* **2016**, *51* (2), 223–235.

(36) Gutberlet, T.; Hilbig, H.; Beddoe, R. E. Acid Attack on Hydrated Cement—Effect of Mineral Acids on the Degradation Process. *Cem Concr Res* **2015**, *74*, 35–43.

28

(37)   Jackson, M. D.; Chae, S. R.; Mulcahy, S. R.; Meral, C.; Taylor, R.; Li, P.; Emwas, A.-H.; Moon, J.; Yoon, S.; Vola, G. Unlocking the Secrets of Al-Tobermorite in Roman Seawater Concrete. *American Mineralogist* **2013**, *98* (10), 1669–1687.

(38)   Kunhi Mohamed, A.; Moutzouri, P.; Berruyer, P.; Walder, B. J.; Siramanont, J.; Harris, M.; Negroni, M.; Galmarini, S. C.; Parker, S. C.; Scrivener, K. L. The Atomic-Level Structure of Cementitious Calcium Aluminate Silicate Hydrate. *J Am Chem Soc* **2020**, *142* (25), 11060–11071.

(39)   Richardson, I. G.; Brough, A. R.; Brydson, R.; Groves, G. W.; Dobson, C. M. Location of Aluminum in Substituted Calcium Silicate Hydrate (C-S-H) Gels as Determined by 29Si and 27Al NMR and EELS. *Journal of the American Ceramic Society* **1993**, *76* (9), 2285–2288.

(40)   Andersen, M. D.; Jakobsen, H. J.; Skibsted, J. Characterization of White Portland Cement Hydration and the C-S-H Structure in the Presence of Sodium Aluminate by 27Al and 29Si MAS NMR Spectroscopy. *Cem Concr Res* **2004**, *34* (5), 857–868. https://doi.org/10.1016/j.cemconres.2003.10.009.

(41)   Andersen, M. D.; Jakobsen, H. J.; Skibsted, J. A New Aluminium-Hydrate Species in Hydrated Portland Cements Characterized by 27Al and 29Si MAS NMR Spectroscopy. *Cem Concr Res* **2006**, *36* (1), 3–17.

(42)   Yang, S.-Y.; Yan, Y.; Lothenbach, B.; Skibsted, J. Incorporation of Sodium and Aluminum in Cementitious Calcium-Alumino-Silicate-Hydrate C-(A)-SH Phases Studied by 23Na, 27Al, and 29Si MAS NMR Spectroscopy. *The Journal of Physical Chemistry C* **2021**, *125* (51), 27975–27995.

(43)   Gebauer, D.; Cölfen, H. Prenucleation Clusters and Non-Classical Nucleation. *Nano Today* **2011**, *6* (6), 564–584.

(44)   Karthika, S.; Radhakrishnan, T. K.; Kalaichelvi, P. A Review of Classical and Nonclassical Nucleation Theories. *Cryst Growth Des* **2016**, *16* (11), 6663–6681.

(45)   Garrault-Gauffinet, S.; Nonat, A. Experimental Investigation of Calcium Silicate Hydrate (CSH) Nucleation. *J Cryst Growth* **1999**, *200* (3–4), 565–574.

(46)   Krautwurst, N. Nucleation of Calcium Silicate Hydrate in Aqueous Solution and the Influence of Biomolecules on Cement Hydration. **2017**, 131.

(47)   Krautwurst, N.; Nicoleau, L.; Dietzsch, M.; Lieberwirth, I.; Labbez, C.; Fernandez-Martinez, A.; Van Driessche, A. E. S.; Barton, B.; Leukel, S.; Tremel, W. Two-Step Nucleation Process of Calcium Silicate Hydrate, the Nanobrick of Cement. *Chemistry of Materials* **2018**, *30* (9), 2895–2904. https://doi.org/10.1021/acs.chemmater.7b04245.

(48)   Schönlein, M.; Plank, J. A TEM Study on the Very Early Crystallization of CSH in the Presence of Polycarboxylate Superplasticizers: Transformation from Initial CSH Globules to Nanofoils. *Cem Concr Res* **2018**, *106*, 33–39.

(49)   Kersten, M. Aqueous Solubility Diagrams for Cementitious Waste Stabilization Systems. 1. The CSH Solid-Solution System. *Environ Sci Technol* **1996**, *30* (7), 2286–2293.

(50)   Carino, A.; Testino, A.; Andalibi, M. R.; Pilger, F.; Bowen, P.; Ludwig, C. Thermodynamic-Kinetic Precipitation Modeling. A Case Study: The Amorphous Calcium Carbonate (ACC) Precipitation Pathway Unravelled. *Cryst Growth Des* **2017**, *17* (4), 2006–2015.

(51)   Carino, A.; Ludwig, C.; Cervellino, A.; Müller, E.; Testino, A. Formation and Transformation of Calcium Phosphate Phases under Biologically Relevant Conditions: Experiments and Modelling. *Acta Biomater* **2018**, *74*, 478–488.

(52) Ng, K. S.; Head, I.; Premier, G. C.; Scott, K.; Yu, E.; Lloyd, J.; Sadhukhan, J. A Multilevel Sustainability Analysis of Zinc Recovery from Wastes. *Resour Conserv Recycl* **2016**, *113*, 88–105.

(53) Li, D.; Xing, G.; Tang, S.; Li, X.; Fan, L.; Li, Y. Ultrathin ZnSe Nanowires: One-Pot Synthesis: Via a Heat-Triggered Precursor Slow Releasing Route, Controllable Mn Doping and Application in UV and near-Visible Light Detection. *Nanoscale* **2017**, *9* (39), 15044–15055. https://doi.org/10.1039/c7nr03547k.

(54) Gopalakrishnan, R.; Nithiyanantham, S. Effect of ZnO Nanoparticles on Cement Mortar for Enhancing the Physico-Chemical, Mechanical and Related Properties. *Adv Sci Eng Med* **2020**, *12* (3), 348–355.

(55) Shafeek, A. M.; Khedr, M. H.; El-Dek, S. I.; Shehata, N. Influence of ZnO Nanoparticle Ratio and Size on Mechanical Properties and Whiteness of White Portland Cement. *Appl Nanosci* **2020**, *10*, 3603–3615.

(56) Bazzoni, A.; Ma, S.; Wang, Q.; Shen, X.; Cantoni, M.; Scrivener, K. L. The Effect of Magnesium and Zinc Ions on the Hydration Kinetics of C3S. *Journal of the American Ceramic Society* **2014**, *97* (11), 3684–3693.

(57) Li, X.; Scrivener, K. L. Impact of ZnO on C3S Hydration and CSH Morphology at Early Ages. *Cem Concr Res* **2022**, *154*, 106734.

(58) Ouzia, A.; Scrivener, K. The Needle Model: A New Model for the Main Hydration Peak of Alite. *Cem Concr Res* **2019**, *115*, 339–360.

Contents

Chapter 3: The Atomic-Level Structure of Zinc-Modified Cementitious Calcium Silicate Hydrate

Authors: Anna Morales-Melgares, Ziga-Casar, Pinelopi Moutzouri, Amrit Venkatesh, Manuel Cordova, Aslam Kunhi Mohammed, Karen L. Scrivener, Paul Bowen, Lyndon Emsley

Commentary about this chapter

Abstract

It has recently been demonstrated that the addition of zinc can enhance the mechanical strength of tri-calcium silicates (C_3S) upon hydration, but the structure of the main hydration product of cement, calcium silicate hydrate (C-S-H), in zinc-modified formulations remains unresolved. Here we combine ^{29}Si DNP enhanced solid-state nuclear magnetic resonance (NMR), density functional theory (DFT) based chemical shift computations and molecular dynamics (MD) modelling to determine the atomic-level structure of zinc-modified C-S-H. The structure contains two main new silicon species ($Q^{(1,Zn)}$ and $Q^{(2p,Zn)}$) where zinc substitutes $Q^{(1)}$ silicon species in dimers and bridging $Q^{(2b)}$ silicon sites, respectively. Structures determined as a function of zinc content show that zinc promotes an increase in the dreierketten mean chain lengths.

Keywords: Calcium, Chemical Structure, Oligomers, Silicon, Zinc

3.1 Introduction

Due to it being the second most used substance on earth (after water), concrete accounts for around 8% of anthropogenic CO2 emissions.[1] The most promising approach to lower this carbon footprint is the partial substitution of clinker by supplementary cementitious materials (SCMs) such as fly ash, blast furnace slag, limestone, and calcined clays. The SCMs have much lower associated CO_2, but blending them with clinker tends to lower the early-age strength of the resulting concrete.[2,3] This means that increasing the reaction rate of cement formation would allow higher substitution levels and lower CO_2 emissions. It has been demonstrated that the addition of zinc to C_3S or alite (the main phase in clinker) can enhance the 1-day mechanical strength of the hydrated paste substantially (×3).[4–6] This accelerated strength development is related to the faster growth of longer and thicker calcium silicate hydrate (C-S-H) particles, which is the main phase (around 50% by volume) in the cement paste part of the final hardened concrete.[7–9] Ouzia and Scrivener[10] demonstrated that C-S-H nucleates and grows predominantly as outgrowths on the surface of alite grains during the hardening reaction (hydration). The rate of reaction peaks at about 10 h (at 20 °C). After this, the reaction rate drops to a low rate at 1 day as the period of fast growth of C-S-H ends. Small amounts of zinc oxide in alite were found to enhance the heat flow and the degree of hydration, and they also result in longer and thicker outgrowths of C-S-H.[11] There is a concomitant enhancement of compressive strength of concrete during the early stages of hardening for up to 7 days.[5] Although zinc addition could potentially increase the overall cost of cement, understanding the role of zinc in C-S-H growth and kinetics would open pathways to synthetic tunability of the rate of reaction of lower-CO_2 materials. However, the atomic-level mechanism of action that links the presence of small amounts of zinc to the enhanced growth of C-S-H, and so to the faster development of strength, is not known. Therefore, it would be of great value to determine how zinc is incorporated into the C-S-H structure at the atomic level. A number of techniques have been used previously to probe the structure of C-S-H,[12–14] but interpretation is hampered by the lack of long-range order. Indeed, the atomic-level structure of C-S-H materials with industrially relevant Ca/Si ratios (i.e., higher than 1.5) was only determined recently[15,16] by the use of a combination of solid-state NMR spectroscopy, molecular dynamics, and density functional theory (DFT)-based chemical shift calculations.

Here, we determine the atomic-level structure of zincmodified synthetic C-S-H using dynamic nuclear polarization (DNP)-enhanced solid-state NMR spectroscopy in concert with other standard characterization methods. Notably, we discover that the structure contains new silicate species that are directly related to the incorporation of zinc and have not been observed previously to the best of our knowledge. We also find that increasing zinc content leads to increasing silicate chain lengths in the structure, which is concomitant with the observed increase in the length of the C-S-H outgrowths at the meso-scale.

33

3.2 Methods

3.2.1 Synthesis

Samples were synthesized through the dropwise precipitation method previously developed by Kumar et al.[15] and standardized by Harris et al.[17] A polymethacrylate batch reactor was placed in a water bath to maintain a temperature between 19 and 21 °C. Two hundred milliliters of a 50 mM sodium silicate solution in deionized water was placed in a batch reactor and 5 mL of 10 M NaOH was added to regulate the final pH between 12.8 and 13.0 to ensure a target Ca/Si molar ratio of ~1.75. The two solutions were mixed and purged under a flow of nitrogen gas for 15 min prior to the reaction. Two hundred milliliters of 90 mM calcium nitrate tetrahydrate (and zinc nitrate hexahydrate with varying concentrations depending on the target $(Zn/Si)_i$) was added through a piston pump at a rate of 2 mL/min followed by stirring at 1100 rpm for 3 h after which the precipitate was collected, washed with 60 mL of a 50% ethanol/water solution, and filtered under vacuum. The supernatant of each sample was also collected. The amounts of reactants used for each sample can be found in Table S1 in the Supporting Information (SI).

3.2.2 X-ray Diffraction (XRD)

Powder XRD was performed on a qualitative basis to observe the presence of undesired phases (i.e., portlandite).[18] The main C-S-H peaks appear at 29.4, 32.1, and 50.1 ± 0.1°.[19] A Bruker Discovery X-ray diffractometer with double bounced monochromatic CuK α radiation (λ = 1.54 Å) was used. A fixed divergence slit of 0.25 mm was used and the experimental time for all samples was 30 min. Spectra and further details are given in SI Section IIa.

3.2.3 Inductively Coupled Plasma (ICP)

Samples were prepared by dispersing 20 mg of C-S-H gel or 1 mL of the supernatant in 10 mL or 9 mL of concentrated nitric acid, respectively. Then, the samples were diluted up to three orders of magnitude prior to analysis. Experiments were conducted using a Spectro Arcos ICP-OES analyser from Ametek. Further details are given in SI Section IIc.

3.2.4 Electron Microscopy

A Tecnai OSIRIS TEM system at 200 kV in bright field mode with a single tilt holder and FEI SmartCAM CCD camera was used to observe the sample morphology (SI Section IIb). The TEM grids employed to observe these samples are copper-based grids coated with a thin film of carbon. C-S-H gel (100–300 mg) was dispersed in ca. 20 mL of isopropanol (IPA). The samples were dried prior to analysis.

3.2.5 Electron Dispersive X-rays (EDX)

The same instrument used for TEM analysis was used to conduct STEM and STEM-EDX experiments. In STEM mode, a bright field (BF) detector and a highangle annular dark-field (HAADF) detector were used, whereas in EDX mode, a twin pole piece with a Super-X EDX system and four SDD detectors with a 0.9 rad solid angle were used.

3.2.6 NMR Spectroscopy

Samples were prepared for DNP-enhanced NMR[20–22] by adapting previously used protocols for C-S-H materials.[15,16] About 300 mg of the C-S-H gel was mixed with 3 mg of AMUPol[23] and dried under N_2 flow to $\sim$200 mg before packing into sapphire rotors and sealing with PTFE inserts and zirconia drive caps. Since the poorly crystalline C-S-H structure contains a substantial amount of water that is not all removed, no additional impregnating medium is required.[15] All experiments were performed using a 400 MHz Bruker Avance III HD NMR spectrometer equipped with a 263 GHz Bruker gyrotron[24] or klystron microwave source and a HXY 3.2 mm low-temperature MAS DNP probe in ^{1}H–^{29}Si configuration at 100 K. ^{1}H DNP enhancements were measured as the ratio of the ^{1}H$\rightarrow^{29}$Si cross-polarization (CP) signal intensity between spectra recorded with and without microwaves and were found to be between 30 and 40. All spectra were acquired at a magic angle spinning (MAS) frequency of 8 kHz, except for SUPER[25] and 2D spin diffusion experiments, which were performed at 5 kHz. For multi-CPMAS experiments, presaturation pulse trains were applied on ^{1}H and ^{29}Si channels. The ^{29}Si chemical shifts were referenced to tetrakis (trimethylsilyl)silane (TMSS). Topspin was used to acquire and process NMR spectra, while fitting of the chemical shift anisotropy patterns was performed with ssNake.[26] Additional experimental details are provided in the SI.

3.2.7 Atomistic Structure Modeling

The previously reported brick model was used to generate candidate zinc-modified C-S-H structures.[27] LAMMPS28 was used for structure energy minimization and the Erica FF2[29] force field extended with the required zinc interatomic potentials[30] was used. A single or double brick unit cell was constructed with a target Ca/(Si+Zn) ratio while maintaining the characteristic features of the C-S-H structure.[15] Some silicate tetrahedra were replaced with zinc polyhedra including fourcoordinate ZnO_4^{6-} and $ZnO_2(OH)_2^{4-}$ and five-coordinate $ZnO_2(OH)_3^{5-}$ species. To achieve charge balance, the number of interlayer calcium ions (Ca^{2+}) and hydroxides (OH^-) were adjusted. Classical energy minimization with the Erica FF2 force field was carried out prior to the DFT energy minimization to discard energetically unfavorable structures and save computational time. Full details and codes used are provided with the raw data.

3.2.8 Chemical Shift Computations

The atomic positions and lattice parameters of the structures obtained from molecular dynamics modeling were first optimized using the Perdew–Burke–Ernzerhof (PBE)[31] functional and Grimme D2 dispersion correction.[32,33] Projector augmented wave scalar relativistic pseudopotentials obtained from

35

PSlibrary version 1.0.0 were used.[34,35] Semicore *s* and *p* electrons were included for zinc and calcium, and nonlinear core correction was applied for heavy atoms. Wavefunction and charge density energy cutoffs were set to 160 and 1280 Ry, respectively. A Monkhorst–Pack grid of *k*-points corresponding to a maximum spacing of 0.05 Å−1 was used.[36] After geometry optimization, a single-point computation was performed with the same parameters, and chemical shieldings were computed using the GIPAW method.[37,38] The conversion from computed shieldings (σ) to ^{29}Si chemical shifts (δ) was carried out by linear regression ($\delta = -1.05\sigma + 345.32$) using a reference set of crystal structures containing willemite,[39] hemimorphite,[40] foshagite,[41] and α-quartz[42] with their corresponding experimental shifts.[43,44] All NMR computations were carried out using the plane-wave DFT program Quantum ESPRESSO v6.5.[45,46] Simulated ^{29}Si spectra for individual Si sites were generated using a kernel density estimate of Gaussian kernels as implemented in the scipy Python library.[47]

3.3. Results and discussion

3.3.1. Chemical Composition and Morphology

As described previously, single-phase C-S-H can be synthesized using a dropwise precipitation method, which allows for a controlled synthesis of C-S-H with a specific Ca/Si ratio.[17] This approach was modified to produce zinc-modified C-S-H by adding certain amounts of zinc nitrate hexahydrate to the aqueous calcium nitrate solution depending on the target Zn to Si ratio (denoted as $(Zn/Si)_i$ where the subscript *i* indicates that it is the initial ratio used in the synthesis). The initial calcium and zinc nitrate solution had calcium concentration of 90 mM and zinc concentration of 0, 7.5, or 20 mM depending on their target $(Zn/Si)_i$ (e.g., 0, 0.15, and 0.40, respectively). The initial sodium metasilicate solution had a concentration of 50 mM. As described by Anseau et al.,[48] both zinc and aluminum can form complexes with silicate monomers, which are the main species in solution at the pH used here. Therefore, zinc is expected to behave similar to aluminum and to substitute for silicate species, as seen in the case of aluminum incorporation in C-A-S-H structures synthesized through dropwise precipitation.[16] In addition, previous studies on C_3S hydration in the presence of zinc show that zinc is in tetrahedral coordination and substitutes for silicate species in C-S-H chains.[49,50] DFT-relaxed structures in which zinc substituted for calcium in the main layer presented 6-fold coordination and unusually long bond lengths (see SI Section VII); therefore, substitution of main layer calcium by zinc was neglected. The possible sites where different zinc polyhedra can be incorporated into the C-S-H structure (Figure 3.1A) are illustrated in Figure 3.1B. These structures are a result of zinc substitutions of $Q^{(2b)}$, $Q^{(2p)}$, or $Q^{(1)}$ sites in conventional C-S-H. In addition, the figure also shows how zinc can also be present on top of the silicate chains, facing into the interlayer, where it could coordinate to one or both $Q^{(1)}$ species of a silicate dimer.
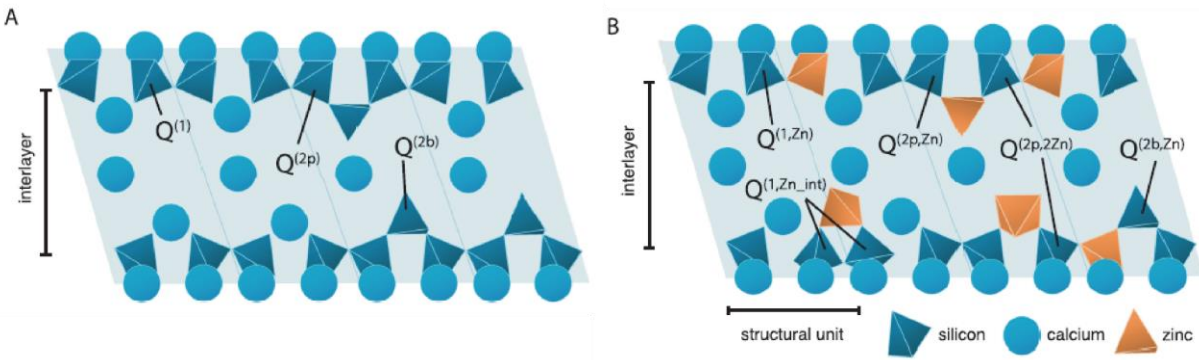
Figure 3.1: A) Schematic of the dreierketten chains in conventional C-S-H showing all of the silicate species present: $Q^{(1)}$, $Q^{(2b)}$, and $Q^{(2p)}$. B) Schematic of zinc-modified C-S-H, showing all of the new silicate sites that could potentially be present: $Q^{(1,Zn)}$, $Q^{(2p,Zn)}$, $Q^{(2p,2Zn)}$, $Q^{(2b,Zn)}$, and $Q^{(1,Zn\_int)}$.

If zinc substitutes for the $Q^{(2b)}$ site, it yields two identical new neighboring silicate species, which, following the Q-site nomenclature, are named $Q^{(2p,Zn)}$. If zinc substitutes for a $Q^{(2p)}$ site, it yields a $Q^{(2b,Zn)}$ species and either a $Q^{(1,Zn)}$ or a $Q^{(2p,Zn)}$ depending on whether the chain unit is a pentamer or a higher-degree unit, respectively. If zinc substitutes for a $Q^{(1)}$ site it can yield a $Q^{(1,Zn)}$ or a $Q^{(2p,Zn)}$, depending on whether the chain unit is a dimer or a higher-degree unit. If zinc is adjacent to both silicates in a $Q^{(1)}$–$Q^{(1)}$ dimer, it coordinates to one or both $Q^{(1)}$ species and protrudes into the interlayer, becoming a $Q^{(2p,Zn\_int)}$. Finally, this model also includes the possibility of two zinc units substituting for two silicate chain sites simultaneously (i.e., $Q^{(1)}$ and $Q^{(2p)}$), producing a new silicate species that is isolated from other silicate linkages, as represented in Figure 1B in the case of $Q^{(2p,2Zn)}$ species.
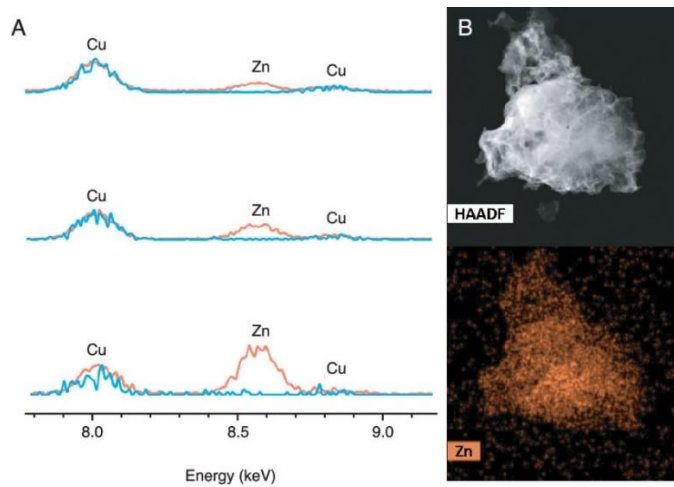
Figure 3.2: A) STEM-EDX spectra of C-S-H samples with (Zn/Si)$_i$ ratios of 0.03 (top), 0.08 (center), and 0.15 (bottom). For each (Zn/Si)$_i$, spectra corresponding to regions including (orange) and excluding (blue) C-S-H particles are shown. The intensities of the Zn signals are normalized with respect to the Cu absorption line at 8 keV from the TEM grid. B) HAADF-STEM X-ray composition map of a C-S-H particle with a (Zn/Si)$_i$ ratio of 0.15, showing an apparent Zn uptake.

In summary, this scheme includes the possibility of five different four-coordinated zinc species and one five-coordinated zinc species substituting for a Q$^{(2b)}$ site. To determine the atomic-level structure of zinc-modified C-S-H, the chemical composition, purity, and incorporation of zinc in the C-S-H structure need to be verified prior to structure determination. A series of XRD experiments were performed to confirm that our material is a single-phase, pure C-S-H sample and no secondary phases such as portlandite are observed (Figure S1). Additionally, inductively coupled plasma (ICP) analysis of the supernatant shows that only around 1 – 2% of the added zinc remains in solution after synthesis (Table S2), indicating the incorporation of the vast majority of zinc into the precipitated zinc-modified C-S-H. Figure 2A shows normalized EDX spectra of samples with different initial Zn to Si ratios of 0.03, 0.08, and 0.15 in the reagent solutions. Comparison of the EDX spectra recorded from a region excluding (blue) and including a C-S-H particle (orange) shows a clear trend: samples that have been synthesized with an increased concentration of zinc nitrate show higher zinc counts in the EDX experiment, pointing to an incorporation of zinc in C-S-H (Figure 3.2A). Furthermore, HAADF and TEM data show no appreciable differences between the observed morphology of conventional C-S-H and zinc-modified C-S-H, with all samples showing a nanofoil morphology that is consistent with the literature (Figures 3.2B and S2).

3.3.2 Characterization by DNP NMR

To determine the zinc-modified C-S-H structure, DNP-enhanced ^{29}Si one-dimensional (1D) multi-CPMAS NMR spectra[51] and two-dimensional (2D) INADEQUATE spectra[15,22,52,53] were obtained.

To be able to acquire the relatively insensitive 1D and 2D ^{29}Si solid-state spectra necessary to determine the populations and connectivities of different silicon sites in the materials, we prepared a series of zinc-modified C-S-H formulations. These were chosen to yield enhancement of NMR signals by MAS DNP,[20,21] by adapting the procedures developed previously[15,16,20] by incorporating a small amount of the organic biradical AMUPol[23] into the C-S-H sample. When the sample is frozen at 100 K, AMUPol allows efficient transfer of large electron polarization to protons in the frozen sample when microwaves are applied. The enhanced ^{1}H magnetization is then transferred to ^{29}Si nuclei through CP.

Figure 3A compares the ^{29}Si DNP-enhanced multi-CP spectra from three samples with (Zn/Si)$_i$ of 0, 0.15, and 0.40. The multi-CPMAS pulse sequence, which is based on the repetition of CP periods,[51] yields ^{29}Si NMR spectra that allow for quantitative analysis of different silicate species in C-S-H samples.[51,54] The spectrum of the sample with (Zn/Si)$_i$ of 0 shows the well-characterized ^{29}Si peaks expected in conventional high Ca/Si ratio C-S-H whose signals are attributed to Q$^{(1)}$ (−78.9 ppm), Q$^{(2b)}$ (−81.4 ppm), and Q$^{(2p)}$ (−84.4 ppm) silicate species.[15,55–57] The spectra of the samples with (Zn/Si)$_i$ of 0.15 and 0.40 show the presence of new Q sites at around −72 and −79 ppm; details regarding the spectral deconvolution are provided below. All of the different species present in the zinc-modified C-S-H spectra are more clearly shown in Figure 3B where the deconvolution of different Q sites is carried out. The presence of the new 29Si signals around −72 and −79 ppm suggests the incorporation of zinc in the C-S-H structure as it indicates that the chemical environment of at least one silicate species is changed with respect to conventional C-S-H samples. The new species that gives rise to the signal at −72 ppm has a chemical shift similar to those of

silicate monomers ($Q^{(0)}$) that typically range from −60 to −75 ppm.[58] Silicate monomers ($Q^{(0)}$) are however discarded since, although observed in minor amounts in works from other groups with different synthetic routes,[59–61] they are not usually observed in C-S-H samples,[15,16] and they are not a characteristic feature of the high Ca/Si ratio C-S-H structures synthesized through our dropwise precipitation method.[15,16]
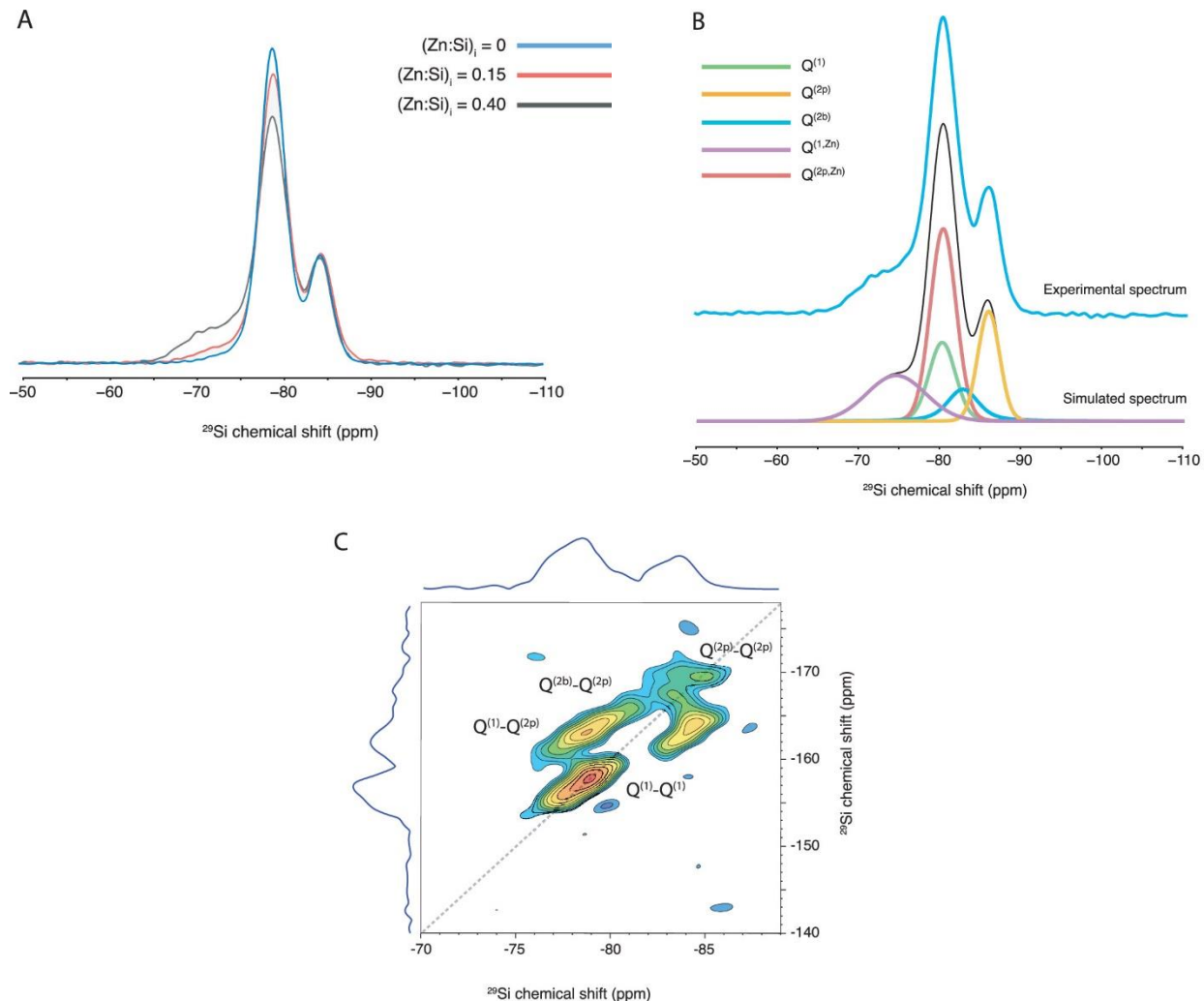
Figure 3.3: DNP-enhanced A) ^{29}Si{^{1}H} 1D multi-CPMAS spectra of samples with $(Zn/Si)_i$ of 0, 0.15, and 0.40; B) 1D multi-CPMAS spectrum of the sample with $(Zn/Si)_i$ of 0.40 (top) showing deconvolution into the different Q sites (bottom); and (C) 2D ^{29}Si–^{29}Si INADEQUATE spectrum of a zinc-modified C-S-H sample with a $(Zn/Si)_i$ ratio of 0.40.

The spectra in Figure 3.3A were normalized to total intensity and show evidence of two trends. As the $(Zn/Si)_i$ is increased, the signal at −78.9 ppm decreases while the new signal at around −72 ppm increases in intensity. To further investigate the species present, DNP-enhanced natural-abundance homonuclear ^{29}Si–^{29}Si refocused INADEQUATE spectra were acquired.[15,22,52,53] A 2D INADEQUATE spectrum of a zinc-

modified C-S-H gel with (Zn/Si)$_i$ of 0.40 is shown in Figure 3.3C (and spectra corresponding to (Zn/Si)$_i$ of 0 and 0.15 are shown in Annex X.

This spectrum shows the expected connectivities in conventional C-S-H samples:[15] Q$^{(1)}$–Q$^{(1)}$, Q$^{(2p)}$–Q$^{(1)}$, Q$^{(2p)}$–Q$^{(2b)}$, and Q$^{(2p)}$–Q$^{(2p)}$. Signals corresponding to Q$^{(2b)}$–Q$^{(1)}$ or Q$^{(2b)}$–Q$^{(2b)}$ connectivities are not present, as is consistent with the connectivity of the C-S-H silicate chains. Additionally, no correlations with the new ^{29}Si species at −72 ppm are observed. Through-space exchange spectroscopy (EXSY) experiments were also carried out and confirmed that this new species, although not having through-bond correlations with other Q sites, has close through-space correlations mediated by spin diffusion, which further confirms its incorporation in the C-S-H internal structure. Results from the ^{29}Si–^{29}Si EXSY experiments are shown in Figures S9 and S10.

3.3.3 Candidate Structure Generation: Stability of Zincate Species in Zinc-Modified C-S-H

To determine the possible sites for incorporation of zinc species into the silicate chains of C-S-H at the atomic level, 98 different zinc-modified C-S-H structural units with Ca/Si ratios ranging from 1.2 to 2.25 were generated via brick models.[27] For each structure, DFT[32,34]- based chemical shifts were calculated and compared to the experimental chemical shifts obtained from 1D and 2D NMR experiments. To calibrate the calculated shifts, the mean shifts of the well-established characteristic sites present in conventional C-S-H gels (Q$^{(1)}$, Q$^{(2p)}$, Q$^{(2b)}$) were computed (Figure 3.4B) and found to be in good agreement with experiments and literature. All possible DFT-based calculated chemical shifts for all of the silicon sites in the 98 candidate structures are provided with the raw data.
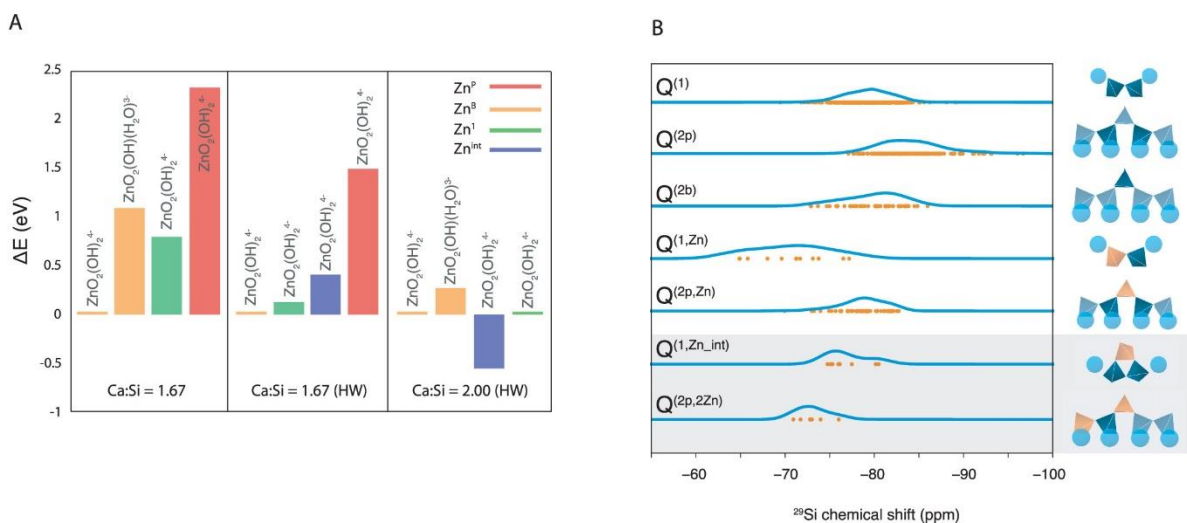
Figure 3.4. A) Relative calculated energies of representative zinc-modified C-S-H structures according to each substitution site with different Ca/Si ratios and interlayer amounts. Each column is normalized to the substitution of zinc in the bridging site with Δ*E* = 0 eV. Nomenclature: Zn^B = zinc in the Q$^{(2b)}$ site, Zn^P = zinc in the Q$^{(2p)}$ site, Zn^1 = zinc in the Q$^{(1)}$ site, Zn^{Int} = zinc on top of a Q$^{(1)}$–Q$^{(1)}$ dimer site, and HW = high water content. All structures are labeled with their corresponding zinc species that may coordinate to hydroxides

or water. B) DFT-calculated shifts from the silicate species obtained from brick models for zinc-modified C-S-H and their respective schematic structures.

DFT was also used to compute the absolute energies of each structure to investigate differences in stability. Figure 3.4A shows a selection of relevant structures, where four-coordinated zinc substitutes for $Q^{(1)}$, $Q^{(2p)}$, or $Q^{(2b)}$ silicates or is adjacent to two silicates and in the interlayer. The calculated energies of all candidate structures corresponding to a Ca/Si ratio of 1.67 and 2.0 are shown in Figure S4. Table S3 shows the relative calculated energies of all of the candidate structures, ordered in sets according to their Ca/Si ratio. The calculated energies are normalized to the structure where zinc substitutes for a $Q^{(2b)}$ site and is coordinated as $ZnO_2(OH)_2$, which is consistently the most stable Q-site substitution at Ca/Si ratios of 1.67.

3.3.4 NMR Crystallography with DFT-Based Calculated Chemical Shifts.

The DFT-calculated ^{29}Si isotropic shifts resulting from each structure are shown in Figures 4B and S5 and also provided with the raw data. Results from energy minimization and chemical shift calculations through DFT were then compared to experimental data from both 1D multi-CPMAS and 2D INADEQUATE experiments to verify or discard the relaxed structures, as discussed below.

At the Ca/Si ratios used in this work, zinc substituting for a $Q^{(2b)}$ site is predicted to be the most favorable structure owing to its lowest mean energies, while zinc substituting for a $Q^{(1)}$ site is predicted to be energetically more favorable than zinc substituting for a $Q^{(2p)}$ site (Figure S4). This is consistent with the experimental 2D ^{29}Si–^{29}Si INADEQUATE NMR results, since zinc substitution in a $Q^{(2p)}$ site should yield $Q^{(2b,Zn)}$– $Q^{(2p)}$ and $Q^{(2b,Zn)}$–$Q^{(2p,Zn)}$ correlations in the region between −74.8 and −84.4 ppm, which are not observed. Based on both the calculated energies and the NMR results, we conclude that zinc does not substitute for the $Q^{(2p)}$ species in C-S-H.

When zinc substitutes for a $Q^{(1)}$ site in a dimer, the mean calculated isotropic chemical shift of the generated $Q^{(1,Zn)}$ species, as shown in Figure 3.4B, is −71.5 ppm that is also the measured value for a Zn–Si dimer complex.[48] This value agrees with the signal observed experimentally at approximately −72 ppm and is also consistent with the fact that there are no ^{29}Si–^{29}Si correlations with this chemical shift in the 2D INADEQUATE NMR experiments. Additionally, our DFT calculations predict a lower span (Ω) of the chemical shift anisotropy (CSA) tensor for $Q^{(1,Zn)}$ when compared to the other species, which is in agreement with our experimental results (see SI Section Vd).

Having unambiguously identified the $Q^{(1,Zn)}$ species, we however note that it can only account for ca. 60–70% of the total zinc content (see SI Section Ve). Therefore, the remaining zinc atoms must be incorporated in other sites of the structure.

In all of the 1D multi-CPMAS spectra with the (Zn/Si)$_i$ ratio between 0 and 0.4, the ratios of the integrated signal intensities of Q$^{(2p)}$ and Q$^{(2b)}$ sites are found to be consistently equal to two, as expected. Upon inclusion of a fifth site in the deconvolution of the ^{29}Si NMR spectra with a signal intensity constrained to account for the remaining 30–40% of zinc, the only possible chemical shift for the second new ^{29}Si species is found to be −79 ppm (Figure 3B).

With DFT, substitution for Q$^{(2b)}$ is always predicted to be the most favorable energetically at Ca/Si ratio 1.67 (Table S3), and the resulting two symmetrical ^{29}Si sites, denoted Q$^{(2p,Zn)}$, have a calculated mean chemical shift of −79 ppm.

Due to the overlap of the Q$^{(2p,Zn)}$ species with the Q$^{(1)}$ species (−78.9 ppm), these two species are indistinguishable in 1D ^{29}Si NMR spectra. The Q$^{(2p,Zn)}$ species can be connected either to Q$^{(2p)}$ or Q$^{(1)}$ species, which would yield similar correlations as those observed between Q$^{(1)}$–Q$^{(1)}$ and Q$^{(2p)}$– Q$^{(1)}$ species, making them again indistinguishable in the INADEQUATE spectra. However, we note that the only substitution site that is compatible with both the 1D multi-CPMAS and 2D INADEQUATE experiments is Q$^{(2b)}$, leading to two symmetrical Q$^{(2p,Zn)}$ species. These considerations, taken together with the fact that the integrated area corresponding to the conventional Q$^{(2p)}$ sites cannot account for all of the expected new species arising from zinc incorporation, led us to determine that the only region where the signal corresponding to Q$^{(2p,Zn)}$ species could be is indeed overlapping with the signal that corresponds to the Q$^{(1)}$ species. Therefore, we assign a second new ^{29}Si species at −79 ppm to be Q$^{(2p,Zn)}$. The substitution at the bridging site is also analogous to the previously determined C-A-S-H structure.[16]

Based on the evidence shown, Q$^{(1,Zn)}$ and Q$^{(2p,Zn)}$ species are identified as the main silicate species arising from zinc incorporation in C-S-H systems.

Finally, we consider two other energetically possible sites Q$^{(2p,2Zn)}$ and Q$^{(1,Zn\_int)}$ (see Figure 4B). Q$^{(2p,2Zn)}$ species (Figure 1), with a calculated chemical shift of −73.0 ppm, can only be present in a pentamer or a higher-degree unit if zinc substitutes for the Q$^{(1)}$ and Q$^{(2b)}$ species simultaneously, creating a Zn−Si−Zn linkage at the start of the chain. The calculated chemical shift is similar to that of Q$^{(1,Zn)}$ species and would yield a signal in the 1D ^{29}Si experiments while yielding no ^{29}Si−^{29}Si correlations in the 2D ^{29}Si INADEQUATE NMR experiments, which is compatible with our results. This species requires a high (Zn/Si)i as well as a high degree of polymerization to occur, as it is the combination of a zinc substitution for Q$^{(1)}$ and Q$^{(2b)}$ simultaneously. Due to the fact that this species (Q$^{(2p,2Zn)}$) requires two Zn substitutions to occur, though possible, they are rendered less probable and are discarded in further analysis.

Q$^{(1,Zn\_int)}$ (Figure 1) has a calculated chemical shift at around −75 ppm, which would overlap with the signal from Q$^{(1)}$ species. Similarly to Q$^{(2p,Zn)}$ species, Q$^{(1,Zn\_int)}$ species would also be unresolvable in ^{29}Si−^{29}Si INADEQUATE NMR experiments since their predicted correlation would overlap with the Q$^{(1)}$–Q$^{(1)}$ correlation. However, to our knowledge, there are no known structures that exhibit such a Zn−Si feature. Therefore, again, though possible, this species is not considered further.

A summary of the predicted silicate species that arise from zinc incorporation into C-S-H and their DFT-calculated chemical shift distributions is shown in Figure 4B. Our experimental results identify that zinc-modified C-S-H includes $Q^{(1)}$, $Q^{(2p)}$, $Q^{(2b)}$, $Q^{(1,Zn)}$, and $Q^{(2p,Zn)}$, and while $Q^{(2p,2Zn)}$ and $Q^{(1,Zn\_int)}$ species are predicted to be feasible with regard to the energetics, they cannot be verified through ^{29}Si NMR experiments and no such species have been found in the literature, they are therefore shown in Figure 3.4B as possible structures but they are discarded for the following C-S-H chain length and Q population analyses.

3.3.5 Chain Length and Population Analysis

Quantitative analyses of Q species populations and C-S-H chain length distributions were carried out assuming the silicate species present in zinc-modified C-S-H samples are $Q^{(1)}$, $Q^{(2b)}$, $Q^{(2p)}$, $Q^{(1,Zn)}$, and $Q^{(2p,Zn)}$.

The spectra acquired from samples with (Zn/Si)i of 0, 0.15, and 0.40 were analyzed by fitting each of the constituent Q sites with a Gaussian lineshape whose integrals are used to determine the relative populations of Q species in each sample (Figure 5). As mentioned above, at a $(Zn/Si)_i$ ratio of 0 (conventional C-S-H), typical ^{29}Si signals for C-S-H with high Ca/Si ratios are present: $Q^{(1)}$ at −78.9 ppm, $Q^{(2b)}$ at −81.4 ppm, and $Q^{(2p)}$ at −84.4 ppm. The population analysis from multi-CPMAS matches the results of Kumar et al.[15] for pure single-phase C-S-H samples with Ca/Si ratios of 1.75.
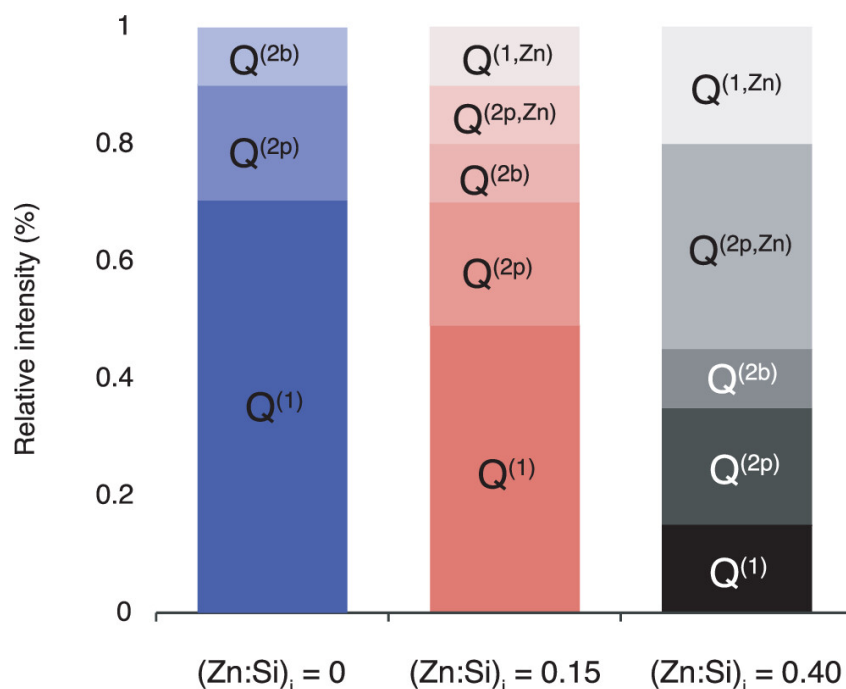
Figure 3.5: Results of the quantitative population analysis in the three samples with (Zn/Si)*i* of 0, 0.15, and 0.40.

Figure 3.5 shows a quantitative Q species population analysis of the three samples with different $(Zn/Si)_i$ ratios. These results show that conventional C-S-H has a population distribution in which the majority (70%) of the silicate species are $Q^{(1)}$ sites, which is consistent with the literature for high Ca/Si ratios, while 20% are $Q^{(2p)}$ sites and 10% are $Q^{(2b)}$ sites. As zinc is incorporated into the C-S-H structure, the population of $Q^{(1)}$ species decreases, while the populations of $Q^{(2p)}$ and $Q^{(2b)}$ species remain constant. The populations of $Q^{(1,Zn)}$ and $Q^{(2p,Zn)}$ increase upon zinc incorporation. $Q^{(1,Zn)}$ species constitute 10% of all silicate species in samples with $(Zn/Si)_i$ of 0.15, while constituting 23% of all silicate species in the sample with $(Zn/Si)_i$ of 0.40. The $Q^{(2p,Zn)}$ species increases from 10% in the sample with $(Zn/Si)_i$ of 0.15 to 34% in the sample with $(Zn/Si)_i$ of 0.40. This analysis suggests a conversion of $Q^{(1)}$ species into $Q^{(1,Zn)}$ and $Q^{(2p,Zn)}$ species as more zinc is incorporated into the C-S-H structure.

The effect of zinc on the Q-site populations can be related to changes in the distribution of mean chain lengths. Understanding the effect of zinc on the mean chain length distributions could allow for a fine tunability of this material for its implementation at a macroscopic scale. To assess the chain length distribution of zinc-modified C-S-H, it is again assumed that the only species present in the material are $Q^{(1)}$, $Q^{(2p)}$, $Q^{(2b)}$, $Q^{(1,Zn)}$, and $Q^{(2p,Zn)}$. Integrals from the multiCPMAS population analysis can be combined with the 2D connectivities seen in the INADEQUATE spectra to estimate the molar fractions of dimers in the system following the approach of Kumar et al.,[15] as described in SI Section Vf. Removing SiO_2 units from bridging sites creates defects that shorten and break the chains, generating dimers (x_0), pentamers (x_1), octamers (x_2), and higher-degree units with increasing numbers of SiO_2 bridging sites (x_n). The extent of defects determines the mean chain length, as well as its distribution into dimers, pentamers, octamers, or longer silicate–zincate units. The chain lengths for each sample are estimated by calculating the molar fractions of $Q^{(1)}$–$Q^{(1)}$ and $Q^{(1)}$–$Q^{(1,Zn)}$ dimers (x_0) and deriving the molar fraction of the silicate–zincate species that have higher degrees of polymerization (x_n).

Table 1 shows the molar fractions of the three samples with different $(Zn/Si)i$ ratios. The molar fraction of the higherdegree units (x_n), which is a direct sign of a higher degree of polymerization, is lowest in the pure C-S-H sample with $(Zn/Si)i = 0$. The molar fraction of higher-degree units increases to 0.52 in the sample with $(Zn/Si)i = 0.15$ and to 0.62 in the sample with $(Zn/Si)i = 0.40$.

Table 3.1: Molar Fractions of Dimers (x_0), Higher-Degree Units (x_n), and Mean Chain Length (MCL) for samples with $(Zn/Si)i$ of 0, 0.15, and 0.40.

$(Zn/Si)_i$ ratio	x_0	x_n	MCL
0.00	0.86	0.14	2.9
0.15	0.48	0.52	3.3
0.40	0.38	0.62	4.5

In addition to the molar fractions of dimers and higherdegree units present in zinc-modified C-S-H, the mean chain length (MCL) of each system was calculated. MCL is calculated according to *eq 1* below.

$$MCL = \frac{tptal\ Si\ +\ Zn\ species}{0.5(non\ bridging\ species) - (bridging\ species)} \qquad (1)$$

The MCL of the conventional C-S-H sample (with $(Zn/Si)_i = 0$) is 2.9, and is consistent with the literature for high Ca/Si ratios.[27] The sample with $(Zn/Si)_i = 0.15$ has a calculated MCL of 3.3, and the sample with $(Zn/Si)_i = 0.40$ has a MCL of 4.5. This shows that the presence of $Q^{(2p,Zn)}$ species in zinc-modified C-S-H systems leads to increased MCL with respect to unmodified C-S-H. We conclude that zinc-modified C-S-H has a higher degree of polymerization when compared to conventional C-S-H.

Figure 6 shows a representative atomic-level structure of the zinc-modified C-S-H determined here. It has the characteristic C-S-H $Q^{(1)}$ (−78.9 ppm), $Q^{(2p)}$ (−81.4 ppm), and $Q^{(2b)}$ (−84.36 ppm) species, as well as the newly discovered $Q^{(1,Zn)}$ and $Q^{(2p,Zn)}$ species, and in this example, the $(Zn/Si)_i$ is 0.15. Additional representative structures that incorporate the DFT-predicted $Q^{(1,Zn\_int)}$ and $Q^{(2p,2Zn)}$ species are shown in SI Section VI.
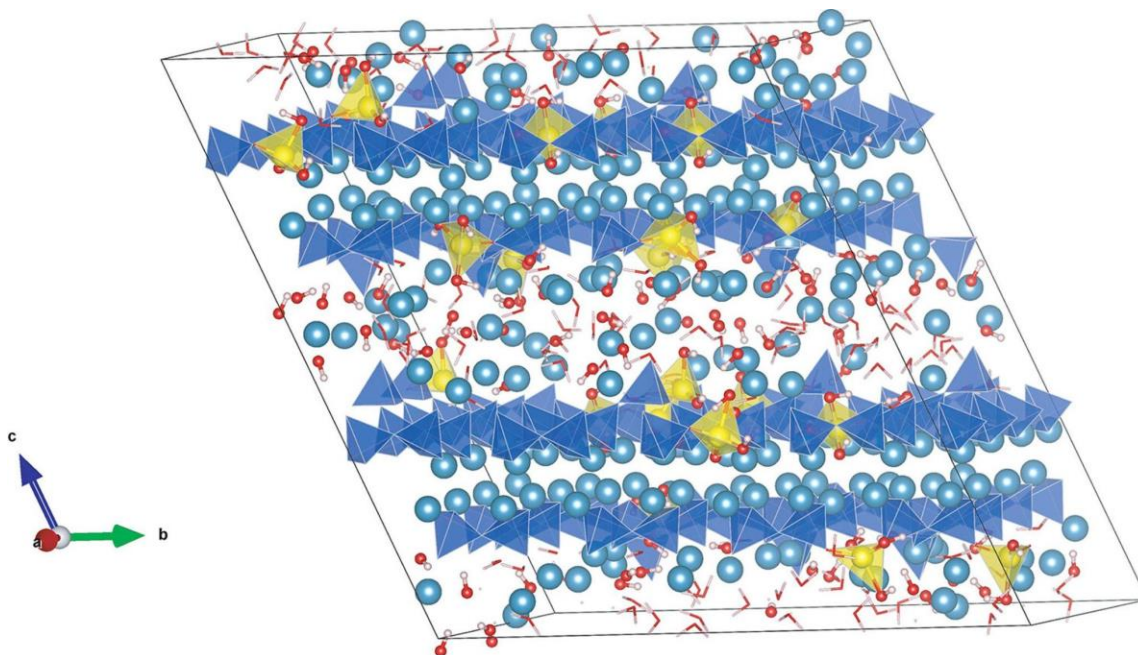
Figure 3.6: Representative atomic-level structure of zinc-modified C-S-H as determined with $(Zn/Si)_i = 0.15$. Silicate tetrahedra are depicted in blue; zincate tetrahedra are depicted in yellow; and calcium ions are depicted in light blue.

Formation of zinc-Modified C-S-H

We have identified two sites for the incorporation of tetrahedrally coordinated zinc oxyhydroxide species $(ZnO_2(OH)_2^{4-})$ into C-S-H. This was done experimentally at a Ca/Si ratio of 1.75 and explored between 1.25 and 2.25 with atomistic modeling. As mentioned above, the incorporation of small amounts of zinc in the hydration of the key cement phases leads to significant acceleration in hydration kinetics and accompanying increase in hardened strength.[5,11] Synthetic C-S-H systems generally show a thin sheet morphology (Figures 3.2B and S2), indicating that growth is mainly in the a–b directions and very limited along the c-axis. Three of the zinc sites are found in the silicate chains, which lie parallel to the b-direction. During the growth of C-S-H, the main silicate species in solution is the neutral complex $CaSiO_2(OH)_2$ (present at 2 mM concentrations).[62] To link these species to form the calcium silicate sheets that make up C-S-H, bridging species such as monomeric silicates (0.05 mM) or Ca^{2+} (10 mM) are needed. The main zinc species in solution is $ZnO_2(OH)_2^{4-}$ (2 mM) at the pH values used here and in cementitious systems.[48] Here, we have found that this species is readily incorporated into both the bridging position and the $Q^{(1)}$ end chain position and can hence accelerate the growth of C-S-H by simply increasing the number of growth units in solution. From ICP measurements of the supernatant (Figure S3), we see that even at a molar ratio of 0.4 Zn/Si, the vast majority (98–99%) of the zinc is incorporated into the C-S-H. Taking the ensemble of our observations together, we suggest the acceleration seen in hydration[4–6] could be due to the enhanced concentration of effective monomeric growth species (Zn $\gg$ Si) at the early stages of growth. Additionally, $[(HO)_3ZnOSiO_2OH]^{4-}$ and $[(HO)_3ZnO \text{ - } (SiO_2)O(SiO_2)OH]^{6-}$ species have been postulated at pH above 14, and they may also play a role in the chain formation process.[48] To validate the hypotheses generated from the atomic-level structures of zinc-modified C-S-H determined here, detailed thermodynamic modeling and kinetic experiments on synthetic C-S-H in the presence of zinc will be carried out in future studies, for example, using the population balance approach developed by Andalibi et al.[62] to model both growth rates and monitor solution speciation as a function of the reaction time.

3.4. Conclusions

We precipitated pure single-phase C-S-H in the presence of zinc with a target Ca/Si ratio of 1.75, analogous to industrially relevant compositions, from a solution of aqueous sodium metasilicate, calcium nitrate, and zinc nitrate under controlled pH, temperature, and atmospheric conditions. TEM was used to observe the microstructure of the precipitated product, and EDX confirmed the local composition. DNP-enhanced 1D $^1H \rightarrow ^{29}Si$ multi-CPMAS NMR was used to measure quantitative populations of Q species, and natural-abundance 2D ^{29}Si -^{29}Si INADEQUATE spectra were used to determine the connectivities between the silicate species. These data, in combination with atomistic modeling and DFT chemical shift calculations, were used to determine the atomic-level structure of zinc-modified synthetic C-S-H. Specifically, as shown in Figure 3.6, two new silicate sites are present in the structure: $Q^{(1,Zn)}$ and $Q^{(2p,Zn)}$. By determining the structure in three samples with different $(Zn/Si)_i$ ratios, we find that zinc promotes an increase of the mean chain lengths. The structure suggests that the enhanced hydration kinetics in zinc-containing cementitious systems could be due to the enhanced concentration of effective monomeric species at the

early stages of growth. Considering that real cementitious systems also contain aluminum and that aluminum is known to incorporate into the C-S-H structure, work is in progress to study the impact of dual incorporation of zinc and aluminum in C-S-H.

3.5. Associated content

The Supporting Information is available free of charge at https://pubs.acs.org/doi/10.1021/jacs.2c06749. Experimental details, additional characterization data, structures, and link to the raw data (DFT output files of each structure investigated, LAMMPS input files, and NMR raw data) (PDF) CIF files of the Zn-modified C-S-H structures (ZIP).

3.6. Acknowledgements

3.7. References

(1) Scrivener, K. L.; Kirkpatrick, R. J. Innovation in Use and Research on Cementitious Material. Cem. Concr. Res. 2008, 38, 128– 136.

(2) Megat Johari, M. A.; Brooks, J. J.; Kabir, S.; Rivard, P. Influence of Supplementary Cementitious Materials on Engineering Properties of High Strength Concrete. Constr. Build. Mater. 2011, 25, 2639– 2648.

(3) Juenger, M. C. G.; Siddique, R. Recent Advances in Understanding the Role of Supplementary Cementitious Materials in Concrete. Cem. Concr. Res. 2015, 78, 71–80.

(4) Stephan, D.; Maleki, H.; Knöfel, D.; Eber, B.; Härdtl, R. Influence of Cr, Ni, and Zn on the Properties of Pure Clinker Phases: Part I. C3S. Cem. Concr. Res. 1999, 29, 545–552. Journal of the American Chemical Society pubs.acs.org/JACS Article https://doi.org/10.1021/jacs.2c06749 J. Am. Chem. Soc. 2022, 144, 22915–22924 22922

(5) Li, X.; Scrivener, K. L. Impact of ZnO on C3S hydration and CS-H Morphology at Early Ages. Cem. Concr. Res. 2022, 154, No. 106734.

(6) Odler, I.; Abdul-Maula, S. Polymorphism and Hydration of Tricalcium Silicate Doped with ZnO. J. Am. Ceram. Soc. 1983, 66, 1– 4.

(7) Bullard, J. W.; Jennings, H. M.; Livingston, R. A.; Nonat, A.; Scherer, G. W.; Schweitzer, J. S.; Scrivener, K. L.; Thomas, J. J. Mechanisms of Cement Hydration. Cem. Concr. Res. 2011, 41, 1208– 1223.

(8) Scrivener, K. L.; Juilland, P.; Monteiro, P. J. M. Advances in understanding hydration of Portland cement. Cem. Concr. Res. 2015, 78, 38–56.

(9) Scrivener, K.; Ouzia, A.; Juilland, P.; Kunhi Mohamed, A. Advances in Understanding Cement Hydration Mechanisms. Cem. Concr. Res. 2019, 124, No. 105823.

(10) Ouzia, A.; Scrivener, K. The Needle Model: A New Model for the Main Hydration Peak of Alite. Cem. Concr. Res. 2019, 115, 339– 360.

(11) Bazzoni, A.; Ma, S.; Wang, Q.; Shen, X.; Cantoni, M.; Scrivener, K. L. The Effect of Magnesium and Zinc Ions on the Hydration Kinetics of C3S. J. Am. Ceram. Soc. 2014, 97, 3684–3693.

(12) Nonat, A.; Lecoq, X. The Structure, Stoichiometry and Properties of C-S-H Prepared by C3S hydration under Controlled Condition. In Nuclear Magnetic Resonance Spectroscopy of Cementbased Materials; Springer, 1998; pp 197–207.

(13) Nonat, A. The Structure and Stoichiometry of C-S-H. Cem. Concr. Res. 2004, 34, 1521–1528.

(14) Klur, I.; Pollet, B.; Virlet, J.; Nonat, A. C-S-H Structure Evolution with Calcium Content by Multinuclear NMR. In Nuclear magnetic resonance spectroscopy of cement-based materials, Springer, 1998; pp 119–141.

(15) Kumar, A.; Walder, B. J.; Kunhi Mohamed, A.; Hofstetter, A.; Srinivasan, B.; Rossini, A. J.; Scrivener, K.; Emsley, L.; Bowen, P. The atomic-level structure of cementitious calcium silicate hydrate. J. Phys. Chem. C 2017, 121, 17188–17196.

(16) Kunhi Mohamed, A.; Moutzouri, P.; Berruyer, P.; Walder, B. J.; Siramanont, J.; Harris, M.; Negroni, M.; Galmarini, S. C.; Parker, S. C.; Scrivener, K. L.; Emsley, L.; Bowen, P. The Atomic-Level Structure of Cementitious Calcium Aluminate Silicate Hydrate. J. Am. Chem. Soc. 2020, 142, 11060–11071.

(17) Harris, M.; Simpson, G.; Scrivener, K.; Bowen, P. A Method for the Reliable and Reproducible Precipitation of Phase Pure high Ca/Si ratio (> 1.5) Synthetic Calcium Silicate Hydrates (C-S-H). Cem. Concr. Res. 2022, 151, No. 106623.

(18) Maddalena, R.; Hamilton, A. Low-pressure Silica Injection for Porosity Reduction in Cementitious Materials. Constr. Build. Mater. 2017, 134, 610−616.

(19) Renaudin, G.; Russias, J.; Leroux, F.; Frizon, F.; Cau-ditCoumes, C. Structural Characterization of C−S−H and C−A−S−H Samples-Part I: Long-Range Order Investigated by Rietveld Analyses. J. Solid State Chem. 2009, 182, 3312−3319.

(20) Rossini, A. J.; Zagdoun, A.; Lelli, M.; Lesage, A.; Coperet, C.; Emsley, L. Dynamic Nuclear Polarization Surface Enhanced NMR Spectroscopy. Acc. Chem. Res. 2013, 46, 1942−1951.

(21) Lesage, A.; Lelli, M.; Gajan, D.; Caporini, M. A.; Vitzthum, V.; Miéville, P.; Alauzun, J.; Roussey, A.; Thieuleux, C.; Mehdi, A.; Bodenhausen, G.; Cóperet, C.; Emsley, L. Surface Enhanced NMR Spectroscopy by Dynamic Nuclear Polarization. J. Am. Chem. Soc. 2010, 132, 15459−15461.

(22) Rossini, A. J.; Zagdoun, A.; Hegner, F.; Schwarzwälder, M.; Gajan, D.; Copéret, C.; Lesage, A.; Emsley, L. Dynamic Nuclear Polarization NMR Spectroscopy of Microcrystalline Solids. J. Am. Chem. Soc. 2012, 134, 16899−16908.

(23) Sauvée, C.; Rosay, M.; Casano, G.; Aussenac, F.; Weber, R. T.; Ouari, O.; Tordo, P. Highly Efficient, Water-Soluble Polarizing Agents for Dynamic Nuclear polarization at high frequency. Angew. Chem. 2013, 125, 11058−11061.

(24) Ni, Q. Z.; Daviso, E.; Can, T. V.; Markhasin, E.; Jawla, S. K.; Swager, T. M.; Temkin, R. J.; Herzfeld, J.; Griffin, R. G. High Frequency Dynamic Nuclear Polarization. Acc. Chem. Res. 2013, 46, 1933−1941.

(25) Liu, S.-F.; Mao, J.-D.; Schmidt-Rohr, K. A Robust Technique for Two-Dimensional Separation of Undistorted Chemical-Shift Anisotropy Powder Patterns in Magic-Angle-Spinning NMR. J. Magn. Reson. 2002, 155, 15−28.

(26) van Meerten, S. G. J.; Franssen, W. M. J.; Kentgens, A. P. M. ssNake: A Cross-Platform Open-Source NMR Data Processing and Fitting Application. J. Magn. Reson. 2019, 301, 56−66.

(27) Kunhi Mohamed, A.; Parker, S. C.; Bowen, P.; Galmarini, S. An Atomistic Building Block Description of C-S-H-Towards a Realistic C-S-H Model. Cem. Concr. Res. 2018, 107, 221−235.

(28) Thompson, A. P.; Aktulga, H. M.; Berger, R.; Bolintineanu, D. S.; Brown, W. M.; Crozier, P. S.; in't Veld, P. J.; Kohlmeyer, A.; Moore, S. G.; Nguyen, T. D.; et al. LAMMPS-a Flexible Simulation Tool for Particle-Based Materials Modeling at the Atomic, Meso, and Continuum Scales. Comput. Phys. Commun. 2022, 271, No. 108171.

(29) Valavi, M.; Casar, Z.; Kunhi Mohamed, A.; Bowen, P.; Galmarini, S. Molecular Dynamic Simulations of Cementitious Systems Using a Newly Developed Force Field Suite ERICA FF. Cem. Concr. Res. 2022, 154, No. 106712.

(30) Lewis, G. V.; Catlow, C. R. A. Potential Models for Ionic Oxides. J. Phys. C 1985, 18, 1149−1161.

(31) Perdew, J. P.; Burke, K.; Ernzerhof, M. Generalized Gradient Approximation Made Simple. Phys. Rev. Lett. 1996, 77, 3865−3868.

(32) Grimme, S. Semiempirical GGA-Type Density Functional Constructed with a Long-Range Dispersion Correction. J. Comput. Chem. 2006, 27, 1787−1799.

49

(33) Barone, V.; Casarin, M.; Forrer, D.; Pavone, M.; Sambi, M.; Vittadini, A. Role and Effective Treatment of Dispersive Forces in Materials: Polyethylene and Graphite Crystals as Test Cases. J. Comput. Chem. 2009, 30, 934−939.

(34) Kresse, G.; Joubert, D. From Ultrasoft Pseudopotentials to the Projector Augmented-Wave Method. Phys. Rev. B 1999, 59, 1758− 1775.

(35) Dal Corso, A. Pseudopotentials Periodic Table: From H to Pu. Comput. Mater. Sci. 2014, 95, 337−350. (36) Monkhorst, H. J.; Pack, J. D. Special Points for Brillouin-Zone Integrations. Phys. Rev. B 1976, 13, 5188−5192.

(37) Pickard, C. J.; Mauri, F. All-Electron Magnetic Response with Pseudopotentials: NMR Chemical Shifts. Phys. Rev. B 2001, 63, No. 245101.

(38) Yates, J. R.; Pickard, C. J.; Mauri, F. Calculation of NMR Chemical Shifts for Extended Systems using Ultrasoft Pseudopotentials. Phys. Rev. B 2007, 76, No. 024401.

(39) Klaska, K.-H.; Eck, J.; Pohl, D. New Investigation of Willemite. Acta Crystallogr. B: Struct. Sci. Cryst. Eng. Mater. 1978, 34, 3324− 3325.

(40) Hill, R. J.; Gibbs, G. V.; Craig, J. R. A Neutron-Diffraction Study of Hemimorphite. Z. Kristallogr. Cryst. Mater. 1977, 146, 241− 259.

(41) Gard, J. A.; Taylor, H. F. W. The Crystal Structure of Foshagite. Acta Crystallogr. 1960, 13, 785−793.

(42) Smith, G. S.; Alexander, L. E. Refinement of the Atomic Parameters of [Alpha]-Quartz. Acta Crystallogr. 1963, 16, 462−471.

(43) Chandrappa, G. T.; Ghosh, S.; Patil, K. C. Synthesis and Properties of Willemite, Zn2SiO4, and M2+:Zn2SiO4 (M=Co and Ni). J. Mater. Synth. Process. 1999, 7, 273−279.

(44) Lippmaa, E.; Maegi, M.; Samoson, A.; Engelhardt, G.; Grimmer, A.-R. Structural Studies of Silicates by Solid-State HighResolution Silicon-29 NMR. J. Am. Chem. Soc. 1980, 102, 4889− 4893.

(45) Giannozzi, P.; Baroni, S.; Bonini, N.; Calandra, M.; Car, R.; Cavazzoni, C.; Ceresoli, D.; Chiarotti, G. L.; Cococcioni, M.; Dabo, I.; Dal Corso, A.; de Gironcoli, S.; Fabris, S.; Fratesi, G.; et al. QUANTUM ESPRESSO: a Modular and Open-Source Software Journal of the American Chemical Society pubs.acs.org/JACS Article https://doi.org/10.1021/jacs.2c06749 J. Am. Chem. Soc. 2022, 144, 22915−22924 22923 Project for Quantum Simulations of Materials. J. Phys. Condens. Matter 2009, 21, No. 395502.

(46) Giannozzi, P.; Andreussi, O.; Brumme, T.; Bunau, O.; Buongiorno Nardelli, M.; Calandra, M.; Car, R.; Cavazzoni, C.; Ceresoli, D.; Cococcioni, M.; Colonna, N.; Carnimeo, I.; Dal Corso, A.; de Gironcoli, S.; et al. Advanced Capabilities for Materials Modelling with Quantum ESPRESSO. J. Phys. Condens. Matter 2017, 29, No. 465901.

(47) Virtanen, P.; Gommers, R.; Oliphant, T. E.; Haberland, M.; Reddy, T.; Cournapeau, D.; Burovski, E.; Peterson, P.; Weckesser, W.; Bright, J.; et al. SciPy 1.0: Fundamental Algorithms for Scientific Computing in Python. Nat. Methods 2020, 17, 261−272.

(48) Anseau, M. R.; Leung, J. P.; Sahai, N.; Swaddle, T. W. Interactions of Silicate Ions with Zinc (II) and Aluminum (III) in Alkaline Aqueous Solution. Inorg. Chem. 2005, 44, 8023−8032.

(49) Tommaseo, C. E.; Kersten, M. Aqueous Solubility Diagrams for Cementitious Waste Stabilization Systems. 3. Mechanism of Zinc Immobilizaton by Calcium Silicate Hydrate. Environ. Sci. Technol. 2002, 36, 2919−2925.

(50) Rose, J.; Moulin, I.; Masion, A.; Bertsch, P. M.; Wiesner, M. R.; Bottero, J.-Y.; Mosnier, F.; Haehnel, C. X-Ray Absorption Spectroscopy Study of Immobilization Processes for Heavy Metals in Calcium Silicate Hydrates. 2. Zinc. Langmuir 2001, 17, 3658−3665.

(51) Johnson, R. L.; Schmidt-Rohr, K. Quantitative Solid-State 13C NMR with Signal Enhancement by Multiple Cross Polarization. J. Magn. Reson. 2014, 239, 44−49.

(52) Fyfe, C. A.; Grondey, H.; Feng, Y.; Kokotailo, G. T. NaturalAbundance Two-Dimensional Silicon-29 MAS NMR Investigation of the Three-Dimensional Bonding Connectivities in the Zeolite Catalyst ZSM-5. J. Am. Chem. Soc. 1990, 112, 8812−8820.

(53) Lesage, A.; Bardet, M.; Emsley, L. Through-Bond CarbonCarbon Connectivities in Disordered Solids by NMR. J. Am. Chem. Soc. 1999, 121, 10987−10993.

(54) Bertarello, A.; Berruyer, P.; Skantze, U.; Sardana, S.; Sardana, M.; Elmore, C. S.; Schade, M.; Chiarparin, E.; Schantz, S.; Emsley, L. Quantification of Magic Angle Spinning Dynamic Nuclear Polarization NMR Spectra. J. Magn. Reson. 2021, 329, No. 107030.

(55) Alonso, C.; Fernandez, L. Dehydration and Rehydration Processes of Cement Paste Exposed to High Temperature Environments. J. Mater. Sci. 2004, 39, 3015−3024.

(56) Sato, H.; Grutzeck, M. Effect of Starting Materials on the Synthesis of Tobermorite. MRS Online Proc. Libr. 1991, 245, 235− 240.

(57) Hong, S. H.; Young, J. F. Hydration Kinetics and Phase Stability of Dicalcium Silicate Synthesized by the Pechini Process. J. Am. Ceram. Soc. 1999, 82, 1681−1686.

(58) Wang, L.; Geddes, D. A.; Walkley, B.; Provis, J. L.; Mechtcherine, V.; Tsang, D. C. W. The Role of Zinc in Metakaolin-Based Geopolymers. Cem. Concr. Res. 2020, 136, No. 106194.

(59) Brunet, F.; Bertani, P.; Charpentier, T.; Nonat, A.; Virlet, J. Application of 29Si Homonuclear and 1 H− 29Si Heteronuclear NMR Correlation to Structural Studies of Calcium Silicate Hydrates. J. Phys. Chem. B 2004, 108, 15494−15502.

(60) Cong, X.; Kirkpatrick, R. J. 29Si MAS NMR Study of the Structure of Calcium Silicate Hydrate. Adv. Cem. Based Mater. 1996, 3, 144−156.

(61) Pustovgar, E.; Sangodkar, R. P.; Andreev, A. S.; Palacios, M.; Chmelka, B. F.; Flatt, R. J.; d'Espinose de Lacaillerie, J.-B. Understanding Silicate Hydration from Quantitative Analyses of Hydrating Tricalcium Silicates. Nat. Commun. 2016, 7, No. 10952.

(62) Andalibi, M. R.; Kumar, A.; Srinivasan, B.; Bowen, P.; Scrivener, K.; Ludwig, C.; Testino, A. On the Mesoscale Mechanism of Synthetic Calcium−Silicate−Hydrate Precipitation: a Population Balance Modeling Approach. J. Mater. Chem. A 2018, 6, 363−373.

Contents

Chapter 4: Towards a comprehensive thermodynamic and kinetic model for C-S-H precipitation

4.1 Introduction

Due to the importance of C-S-H in the framework of construction materials, there is a growing interest in modelling the nucleation and growth mechanisms that participate in the precipitation of this phase. For instance, Krautwurst et al.[1] developed an empirical model for C-S-H precipitation and growth, and Reza et al.[2] developed a preliminary thermodynamic model to understand the mesoscale mechanisms behind the precipitation of C-S-H. However, this model only focuses on growth and neglects the initial stages of nucleation, failing to describe the system before precipitation.

In this chapter, a comprehensive C-S-H model is developed which includes a complete set of thermodynamic and kinetic equations and is fitted to high-quality data where all stages of precipitation are represented: pre-titration, pre-precipitation, nucleation, growth, and equilibration. In addition, the model is extended to describe zinc-modified C-S-H and has potential to be extended to other C-S-H-derived materials.

The model described in this chapter represents a big step towards understanding the thermodynamic and kinetic processes that drive the formation of C-S-H, but there are still some unanswered questions and necessary further experiments that are addressed in the outlook section of this chapter (Section 4.4).

4.2 Experimental section

4.2.1 Preparation of precursor solutions

All precursor solutions (calcium nitrate tetrahydrate, zinc nitrate hexahydrate and sodium metasilicate) were prepared by weight by dissolving the needed amount of material (specified in table 1) in 1 L of deionized milliQ water at room temperature. Extra pure calcium nitrate tetrahydrate, zinc nitrate hexahydrate, and sodium metasilicate were purchased from Sigma Aldrich. A 0.1 M NaOH solution was purchased from Merck and used as pH adjuster throughout the experiments.

Table 4.1: Summary of all solutions used in our experimental data gathering. Solutions containing calcium and zinc are specific for each experiment and their nominal zinc to silicon ratios are used as their labelling system. The precursor molar $(Ca/Si)_i$ ratio in each case is 0.4.

Description	Material	Concentration (mM)	Volume (mL)
Initial	Na_2SiO_3	75	50
condition	NaOH	100	300
solutions	H_2O	55.5k	250
$(Zn:Si)_i = 0$	$Ca(NO_3)_2 \cdot 4H_2O$	10	150
	$Zn(NO_3)_2 \cdot 6H_2O$	0	
$(Zn:Si)_i = 0.02$	$Ca(NO_3)_2 \cdot 4H_2O$	10	150
	$Zn(NO_3)_2 \cdot 6H_2O$	0.4	
$(Zn:Si)_i = 0.04$	$Ca(NO_3)_2 \cdot 4H_2O$	10	150
	$Zn(NO_3)_2 \cdot 6H_2O$	1	
$(Zn:Si)_i = 0.06$	$Ca(NO_3)_2 \cdot 4H_2O$	10	150
	$Zn(NO_3)_2 \cdot 6H_2O$	1.6	
$(Zn:Si)_i = 0.08$	$Ca(NO_3)_2 \cdot 4H_2O$	10	150
	$Zn(NO_3)_2 \cdot 6H_2O$	2	

4.2.2 Dropwise precipitation

The precipitation reaction of C-S-H in presence of different concentrations of zinc was carried out through a constant composition approach, as proposed by Kazmierczak et al,[3] Tomson and Nancollas,[4] and Gebauer et al;[5] and as implemented by Carino et al.[6] for the precipitation of $CaCO_3$. In this kind of approach, one precursor solution is poured into a different precursor solution at a known rate. The saturation level (S) of the system is constantly increased through the addition of the first solution, while the temperature and the pH of the system remain constant. When the system reaches a supersaturated state, a solid phase precipitates. The changes in ion concentration, which contain thermodynamic and kinetic information about the nucleation and growth processes of the system, can be collected with ion-specific electrodes. Additionally, pH buffer solutions can be added to the system through a feedback loop connected to a pH electrode to ensure a constant and known pH. In this work, the solution poured into the inlet was a $(CaNO_3)_2 \cdot 4H_2O + Zn(NO_3)_2 \cdot 6H_2O$ solution, while the initial solution that was placed into the reactor was a $NaSiO_3$ solution.

The initial volume (600 mL) at the start of each experiment was reached by mixing 50 mL of a 75 mM $NaSiO_3$ solution with 250 mL of milliQ deionized water and 300 mL of 0.1 M NaOH. This initial solution has a pH of 12.82. The temperature was set to 20 °C with a cooling bath. All three solutions described above were prepared in volumes of 1L in order to use them as much as possible for each different experiment and provide identical initial conditions.

A fourth aqueous solution of 10 mM $Ca(NO_3)_2 \cdot 4H_2O$ and a certain concentration of $Zn(NO_3)_2 \cdot 6H_2O$ which is specific for each experiment is prepared before each run. This solution contains the ions (Ca^{2+}) whose electrical potential (E) is measured during experiments and each of these different solutions only varies

in zinc content. A summary of all solutions used in this work prior to mixing is shown in Table 4.1, where the initial ratio of the precursors which provide zinc and silicon is expressed as $(Zn:Si)_i$.

The calcium/zinc solution was added at a rate of 2 mL/min until a total of 150 mL was added to the system. Addition was then stopped, and the system was let to evolve for approximately 2 h to reach a state close to its thermodynamic equilibrium. NaOH was added to the reactor through the experiment by the dosing system to keep the pH at 12.80 ± 0.01 during the entirety of the experiment.

The data gathered during each step consists of the time, pH, NaOH addition volume, calcium/zinc solution addition volume, temperature, and three Ca^{2+} electric potential signals from each of the three electrodes (ISE 1, ISE 2 and ISE 3). Electric potential (E) data is recorded from three different sources to improve accuracy.
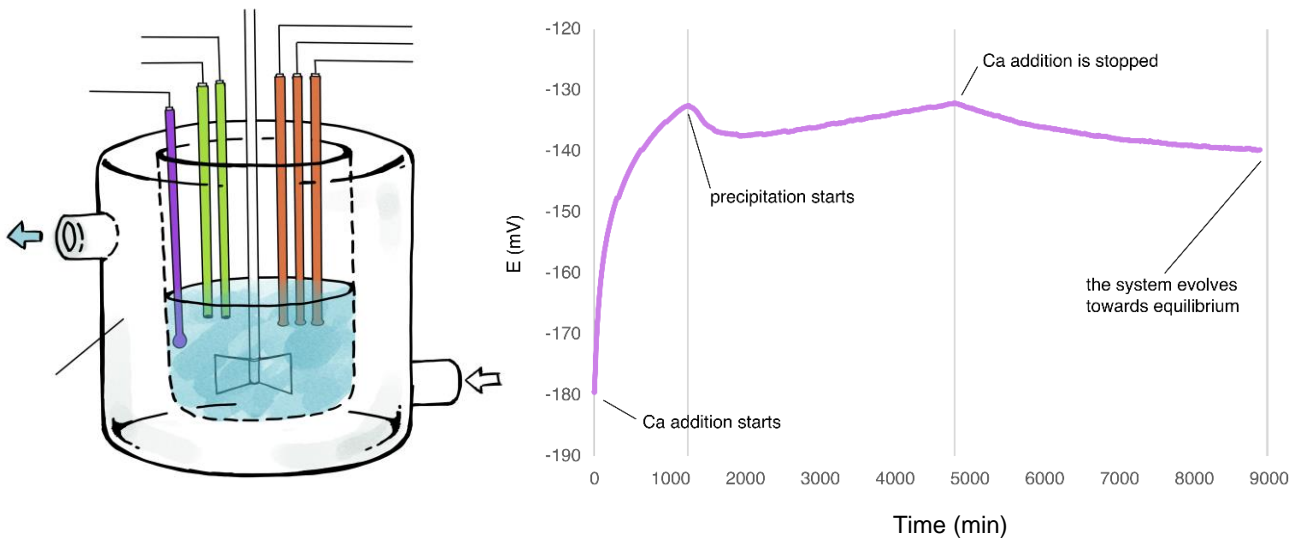
Figure 4.1: A) Scheme of the set-up used in these experiments and B) Ca^{2+} electrical signal vs time. This experiment corresponds to the precipitation of conventional C-S-H (with $(Zn:Si)_i$ of 0.0).

To analyze the system's thermodynamic and kinetic properties, data needs to be expressed as Ca^{2+} activity vs time, which allows for an estimation of the solubility products (K_{sp}) of the phase formed, as well as their relative change in surface energy and supersaturation as zinc is added to the system. This necessitates calibration of the electric signal and fitting to evaluate our data.

4.2.3 Preparation and analysis through TEM

To study the morphology of the precipitate at different experimental times, an aliquot ($\sim$0.5 mL) is extracted with a plastic syringe connected to a diffusion membrane that is introduced into the reactor. One drop of the solution is then placed on a TEM copper/carbon grid (Quantifoil ®, R 1.2/1.3 Cu 400) and an additional drop of isopropanol is added to allow for a rapid drying, stopping the thermodynamic

evolution of the sample. Samples are analyzed with a FEI Tecnai Osiris S/TEM with an alpha-tilt holder and operating at 200 kV.

4.2.4 Calibration and interpretation

Experimental electric potential data (E_{Ca2+}) obtained from the Ca^{2+} electrodes need to be transformed into a Ca^{2+} activity (a_{Ca2+}) dataset that is properly calibrated. This calibration is done by finding the relation between the experimental electric potential (E_{Ca2+}) and the calculated logarithm of Ca^{2+} activity ($log(a_{Ca2+})$) before precipitation with the thermodynamic software OLI stream analyzer,[7] which are theoretically related through the Nernst equation (1):

$$E_{Ca2+} = E_{Ca2+}^o + A \cdot log(a_{Ca2+}) \qquad (1)$$

Where the initial Ca^{2+} potential (E^o_{Ca2+}) is the intercept of this linear relation and A is its slope. The electric potential (E_{Ca2+}) can simply be obtained from our experimental data, and the calculated Ca^{2+} activity values (a_{Ca2+}) can be obtained from OLI stream analyzer and our experimental conditions through the following equation (2):

$$log(a_{Ca2+}) = log(x_{CaT}) + log(f_{Ca2+}) + log\left(\frac{Ca^{2+}}{Ca_T}\right) \qquad (2)$$

Where a_{CaT} is the total activity of all calcium species, x_{CaT} is the molar fraction of total calcium species expected from our experimental conditions, f_{Ca2+} is the activity coefficient of Ca^{2+} (computed through the semi-empirical extension to the Debye-Hükel equation), and Ca^{2+}/Ca_T is the ratio of Ca^{2+} ions to total calcium species. The logarithm of the Ca^{2+} activity ($log(a_{Ca2+})$) is plotted with respect to the experimental data of electric potential (E_{Ca2+}) before precipitation. This relationship theoretically follows a linear trend and allows for the calibration of the entirety of a data set corresponding to one experiment.

4.2.5 Thermodynamic modelling and speciation

The preliminary calculations that are needed to evaluate supersaturation and allow for the tunning of the initial concentrations were carried out with OLI stream analyzer.[7] These calculations indicated that at millimolar concentrations (specified in table 4.1), pH 12.83 and 20° C, C-S-H becomes supersaturated as calcium nitrate is added to the solution and that the system should precipitate in the first 30 min. XRD experiments on our final products confirmed no secondary phases were formed since only the peaks corresponding to C-S-H were observed. In these conditions, the species that need to be considered to describe conventional C-S-H or zinc-modified C-S-H are the ones specified in the equilibrium equations (3) - (12).

$$CaHSiO_3^+ + OH^- \leftrightarrow CaSiO_2(OH)_2^0 \ / \ K_1 = 2.47 \cdot 10^4 \qquad (3)$$

$$Ca^{2+} + OH^- \leftrightarrow CaOH^+ \ / \ K_2 = 16.7 \qquad (4)$$

$$CaOH^+ + SiO_2^0 \leftrightarrow CaHSiO_3^+ \quad / \quad K_3 = 1.59 \cdot 10^4 \tag{5}$$

$$Ca^{2+} + NO^{3-} \leftrightarrow CaNO_3 \ / \quad K_4 = 2.61 \tag{6}$$

$$Na^+ + H_2SiO_4^{2-} \leftrightarrow NaHSiO_3 + OH^- \quad / \quad K_5 = 14.7 \tag{7}$$

$$H_2SiO_4^{2-} + H^+ \leftrightarrow H_2SiO_4 \ / \quad K_6 = 1.27 \cdot 10^{13} \tag{8}$$

$$H_2SiO_4^{2-} + 2H^+ \leftrightarrow SiO_2 + 2H_2O \ / \quad K_7 = 8.53 \cdot 10^{22} \tag{9}$$

$$4SiO_2 + 4H_2O \leftrightarrow Si_4O_6(OH)_6^{2-} + 2H^+ \ / \ K_8 = 7.89 \cdot 10^{-15} \tag{10}$$

$$Na^+ + NO^{3-} \leftrightarrow NaNO_3 \ / \quad K_9 = 0.12 \tag{11}$$

$$2SiO_2 + 3H_2O \leftrightarrow Si_2O_3(OH)_4^{2-} + H^+ \ / \ K_{10} = 1.41 \cdot 10^{-19} \tag{12}$$
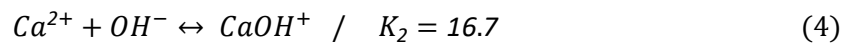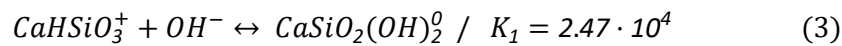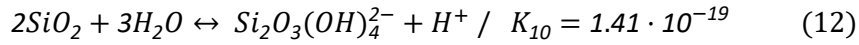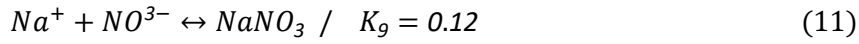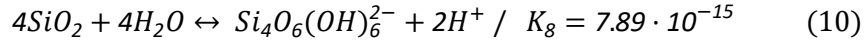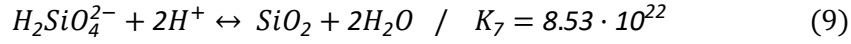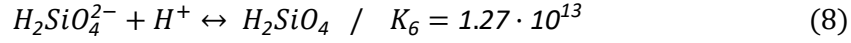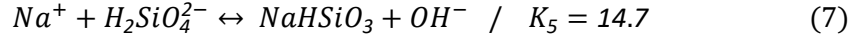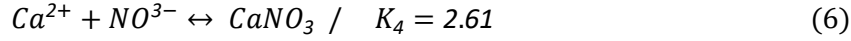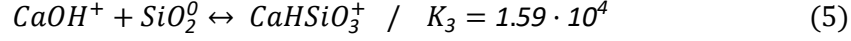
Where the equilibrium constants have been computed by considering formation energies from these species as stated in the *thermoddem* database (also evaluating its consistency with OLI, CEMGEM and NIST databases).

The activity coefficients (δ) and the ionic strength (I) are computed using the Huckel formula (13) and the general formula for ionic strength (14), respectively:

$$\log \delta_i = \frac{Az_i^2\sqrt{I}}{1+B\kappa_i\sqrt{I}} + C_iI + D_iI^2 + E_iI^3 \tag{13}$$

$$I = \frac{1}{2}\Sigma c_i z_i^2 \tag{14}$$

Where A and B are the Debye-Huckel parameters, and C, D, E and κ are specific for each species i; and where z_i is the charge and c_i is molality of species i. The stoichiometry of C-S-H considered in this work is derived from the Richardson and Groves model,[8] in which a number of indices (n, y, w) determine the Ca/Si ratio and the water content of the end-member. The formation of conventional C-S-H is considered in the next chemical equation:

$$n = 1$$

$$\frac{5}{2}CaOH^+ + Si_2O_3(OH)_4^{2-} + 3 \cdot H_2O \leftrightarrow Ca_2H_2Si_2O_7 \cdot \frac{1}{2}Ca(OH)_2 + \frac{1}{2}H^+ \tag{15}$$
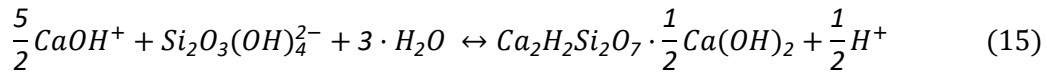
The associated solubility product for conventional C-S-H can be computed, according to Kersten et al.,[9] as the product of the aqueous species ($H_3SiO_4^-$), (OH^-) and ($CaOH^+$); which is convenient in our model since the speciation equations allow for the computing of the activity of these species at any moment during C-S-H precipitation:

$$Ksp_{C-S-H} = (\{H_3SiO_4^-\} + \{OH^-\})\{CaOH^+\} \qquad (15)$$

Finally, the saturation is computed with the corresponding activity product Q_{C-S-H} and K_{sp}:

$$Q_{C-S-H} = a(H_3SiO_4^-)^2 \cdot a(CaOH^+)^{\left(2+\frac{y}{2}\right)} \cdot a(OH^-)^{\frac{y}{2}} \qquad (16)$$

$$S_{C-S-H} = \frac{Q_{C-S-H}\,(t)}{Ksp_{C-S-H}\,(t)} \qquad (17)$$

With these, the full speciation, activity coefficients, ionic products, solubility products, activity products and saturation can be calculated at any time during C-S-H precipitation. Additionally, since NaOH is added through the feedback system in the reactor to maintain a stable pH of 12.82 ± 0.02, the required Na^+ ions are added in the speciation model to reach electroneutrality and serve as an internal check by allowing calculation of the addition volume of NaOH and comparison it to the experimental value.

The equations that define the thermodynamics of the precipitation of conventional C-S-H can also be adapted to describe zinc-modified C-S-H by introducing the index z, which is related to the amount of zinc incorporated in the structure. The additional stoichiometric reactions that need to be added in the zinc-extended model are:

$$Zn^{2+} + 3(OH)^- \leftrightarrow Zn(OH)_3^- \qquad (18)$$

$$Zn(OH)^+ + 2(OH)^- \leftrightarrow Zn(OH)_3^- \qquad (19)$$

$$Zn(OH)_2^0 + OH^- \leftrightarrow Zn(OH)_3^- \qquad (20)$$

$$Zn(OH)_4^{2-} \leftrightarrow OH^- + Zn(OH)_3^- \qquad (21)$$
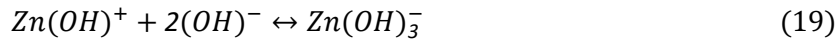
Following the results and conclusions in Chapter 3 (or Morales-Melgares et al.[10]), zinc can substitute for both calcium (in the bridging site) and silicate (bridging and $Q^{(1)}$ sites) species. This conclusion allows for the selection of end-members and the estimation of the stoichiometry of the final product. In the case of conventional C-S-H, different end members were proposed in literature due to the fact that the Ca/Si ratio can vary in a wide range. Kersten[9] proposed a description based on the end members and which was later refined using other end members[11] in order to improve the thermodynamic description of the solid phase. In our case, the selection of the end members is not of much relevance, since no thermodynamic evaluation is carried out on the solid phase. What matters is a clear definition of the end members' stoichiometry. In the case of Zn-modified C-S-H, other two end members should be considered in a general case:

$$Ca_2H_2Si_2O_7 \cdot 3H_2O \leftrightarrow Si_2O_3(OH)_4^{2-} + 2 \cdot CaOH^+ + 3 \cdot H_2O \quad (22)$$

$$Ca(OH)_2 \leftrightarrow CaOH^+ + OH^- \qquad (23)$$

$$Ca[Zn(OH)_3]_2 + OH^- \leftrightarrow CaOH^+ + 2 \cdot Zn(OH)_3^- \qquad (24)$$

$$Zn(OH)_2 + OH^- \leftrightarrow Zn(OH)_3^- \qquad (25)$$
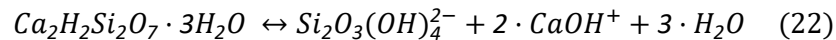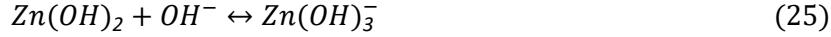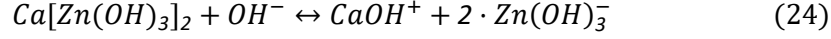
The selection of the specific dissolution reaction is arbitrary and does not influence the generality of the approach. The combination of the four end members in solid solution phase reads:

$$(1-z)[Ca_{2n}H_wSi_{(3n-1)}O_{(9n-2)} \cdot Ca_{\frac{ny}{2}}(OH)_{w+n(y-2)}] \cdot z[\frac{1}{2}Ca[Zn(OH)_3]_2 + (\frac{1}{2}+\frac{y}{4})Zn(OH)_2] \cdot mH_2O \quad (26)$$

This equation can be used to describe conventional C-S-H by simply setting z to zero. By tuning this index, the amount of incorporated zinc can be changed up to a theoretical maximum when z is set to 1, in which case the Zn:Si ratio is virtually infinite, and zinc has replaced all silicate sites. The activity and solubility products, following Kersten's model,[9] can be expressed as (given that n=1, y=2, m=3 and w=2 for simplification):

$$Q_{C-Z-S-H} = a(Si_2O_3(OH)_4^{2-})^{(1-z)} \cdot a(CaOH^+)^{(3+\frac{z}{2})} \cdot a(OH^-)^{(1-z)} \cdot a(Zn(OH)_3^-)^{2z} \qquad (27)$$

$$Ksp_{C-Z-S-H} = \{CaOH^+\}(\{H_3SiO_4^-\} + \{OH^-\} + \{Zn(OH)_3^-\}^2/\{OH^-\}) + \{Zn(OH)_3^-\}/\{OH^-\} \qquad (28)$$

Population mass balance equations are also implemented in the model which consider that the total amounts of calcium (Ca_T), silicon (Si_T), zinc (Zn_T), sodium (Na_T) and nitrogen (N_T), can be described as the sum of the concentrations of the species containing these elements:

$$Ca_T = Ca^{2+} + Ca(OH)^+ + CaSiO_2(OH)_2 + CaHSiO_3 + Ca(NO_3)_2 + \left(2+\frac{y}{2}\right) \cdot CSH \qquad (29)$$

$$Si_T = CaSiO_2(OH)_2 + CaHSiO_3 + NaHSiO_4 + SiO_2 + 2 \cdot Si_2O_3(OH)_4^{2-} + 4 \cdot SiO_4O_6(OH)_6 - 2 \cdot CSH \quad (30)$$

$$Zn_T = Zn^{2+} + Zn(OH)_3^- + Zn(OH)^+ + Zn(OH)_2^0 + Zn(OH)_4^{2-} \qquad (31)$$

$$N_T = Ca(NO_3)_2 + NaNO_3 + NO_3^- \qquad (32)$$

$$Na_T = Na^+ + NaHSiO_3 + NaNO_3 \qquad (33)$$

Where CSH (eq. 29, 30) refers to the solid solution phase in eq. 26. These equations need to be satisfied at all times during an experiment and serve also as an internal check for consistency, since the sum of all species minus the total amounts should always be very close to zero, within a maximum error of $\pm 10^{-9}$.

4.2.6 Kinetic modelling and population balance

To fully model the process of precipitation, it is necessary to account for nucleation and growth, which are kinetic processes. A kinetic package is integrated in the model in which the classical nucleation theory[12] relevant formulae are considered as in the work of Carino et al.[6]

First, the primary homogeneous nucleation rate (B_{homo}), which describes the number of new nuclei that form per unit volume and unit time, can be computed as:

$$B_{homo} = \frac{dN(r)}{dt} = \frac{2D}{d^5} exp\left(-\frac{AG'_{homo}}{k_B T}\right)$$ (34)

Where k_B is the Boltzman constant, T is the temperature, D is the diffusion coefficient of the species forming the nuclei, and d is the molecular diameter of the structural unit. The structural unit is related to the molecular volume through the formula:

$$d = \left(\frac{6}{\pi}v\right)^{1/6}$$ (35)

The activation energy (ΔG^*) depends on the molecular volume, the surface energy (γ), which is a value that can be obtained through fitting with the model, and the saturation (S), and can be computed as follows:

$$\Delta G^*_{homo} = \frac{4}{27}\frac{\varepsilon_A^3}{\varepsilon_v^3}\frac{v^2\gamma_{SL}^3}{k_B^2 T^2 ln^2(S)}$$ (36)

Where ε_A and ε_v are geometrical factors. These factors relate to the area and the volume of a particle and consider one single internal coordinate (L) which is the radius of a spherical particle. For such a spherical particle:

$$\varepsilon_A = 4\pi$$ (37)

$$\varepsilon_v = \frac{4}{3}\pi$$ (38)

$$L^* = \frac{2}{3}\frac{\varepsilon_A}{\varepsilon_v}\frac{v\gamma_{SL}}{k_B T ln(S)}$$ (39)

Where L* is the critical radius of a spherical particle from which it will theoretically undergo growth according to classical nucleation theory. Finally, secondary nucleation (B_{sec}) in three spatial dimensions can be computed from:

$$B_{sec} = \frac{dN(r)}{dt} = \frac{D}{d^4} exp\left(-\frac{AG'_{sec}}{k_B T}\right)$$ (40)

Where the ΔG^*_{sec} is analogous to ΔG^*_{homo} but replacing the surface energy (γ) by the equivalent surface energy which considers the adhesion energy (β).

$$\gamma_{eq} = \gamma - \alpha\beta_{adh} \tag{41}$$

As in the case study of ACC from Carino et al,[6] the growth mechanism considered in the present work is the diffusion of Ca^{2+}, which is the limiting species. The diffusion-limited linear growth can be expressed as:

$$G_D = \frac{dr}{dt} = \frac{Dv}{r}([C_{bulk}] - [C_{surf}]) \tag{42}$$

Where $[C_{bulk}]$ is the molar concentration of Ca^{2+} far from the surface, $[Ca_{surf}]$ is the molar concentration of Ca^{2+} at the surface, and r is the molar radius. The concentration of calcium ions at the surface of the particles can be estimated as:

$$[Ca^{2+}_{surf}] = \frac{a_{Ca^{2+}_{surf}}}{\delta_{Ca^{2+}}} \tag{43}$$

To complete the kinetic part of the model, the populations of particles need to be considered, along with how they change with respect to time. To do this, we use a discretized population balance approach, in which the first four moments of the distribution are calculated and which correspond to the number of particles (m_0), the length of all particles (m_1), the area of all particles (m_2) and the volume of all particles (m_4). The size class discretization used in the present work is the one proposed by Lister et al. and it uses the internal coordinate L which corresponds to the diameter of the particles, as previously mentioned. A differential equation that includes a term for nucleation and terms for growth is considered:

$$\left(\frac{dN_i}{dt}\right)_{total} = \left(\frac{dN_i}{dt}\right)_{primary\ nucleation} + \left(\frac{dN_i}{dt}\right)_{secondary\ nucleation} + \left(\frac{dN_i}{dt}\right)_{growth} \tag{44}$$

This equation only considers nucleation and growth as the terms making the populations of particles change because convection, coalescence and breakage are neglected. Within this simplified differential equation, the *i* index denotes the different size classes to which the populations of particles belong to. The smallest class (*i=0*) corresponds to particles that nucleate and is the only class where there is a contribution from primary nucleation. As particles from i=0 grow according to the growth term (eq. 41), they are transferred from lower-size classes to higher-size classes, as is depicted schematically in Figure 4.2.
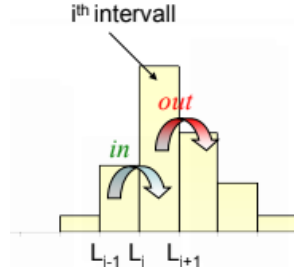
Figure 4.2: Schematic showing the discretized model and how size-classes change when particles nucleate and grow.

The primary and secondary nucleation terms and the growth term can be expressed as:

$$\left(\frac{dN_i}{dt}\right)_{primary\ nucleation} = \{B_{homo}\ if\ i = 0;\ 0\ if\ i \neq 0\} \tag{45}$$

$$\left(\frac{dN_i}{dt}\right)_{primary\ nucleation} = \{B_{sec}\ if\ i = i_{B_{sec}};\ 0\ if\ i \neq i_{B_{sec}}\} \tag{46}$$

$$\left(\frac{dN_i}{dt}\right)_{growth} = \frac{1}{L_i}\sum_{k=1}^{n} a_k\ N_{i-k+1}G_{i-k+1} \tag{47}$$

Where i_{Bhomo} and i_{Bsec} are the classes that contain the critical sizes, k is the number of moments that need to be computed unequivocally (for instance, 4), G is the linear growth rate, and a_k are the numerical growth parameters.

All the equations mentioned in this section are implemented in a FORTRAN[13] code which simultaneously solves for the thermodynamic speciation equations, the mass balances and the kinetic differential equations considering the nucleation and growth terms. The code can solve the complex system of equations within less than 7 s in the case of both conventional C-S-H and zinc-modified C-S-H and allows for the tuning (and fitting) of solubility products (K_{sp}) and surface energies (γ_{homo} and γ_{sec}). Additionally, an extra function is introduced to enforce a planar growth to produce platelets instead of spheres; this will be further discussed in the results and discussion section.

4.3 Results and discussion

4.3.1 Preliminary experimental results

The data from 5 different experiments varying in zinc content was collected (corresponding to the precipitation of the samples described in Table 4.1). The calibration was at first carried out through a normal first-degree Nernst equation but with this approach the pre-precipitation data from experiments

containing zinc showed a non-linear behavior (see Figure 4.3A). The use of a second-degree Nernst equationenforces the linearity of the pre-precipitation data (see Figure 4.3B), but this approach lacks physical meaning and raises questions about what is happening prior to precipitation and the interactions between species when zinc is present.
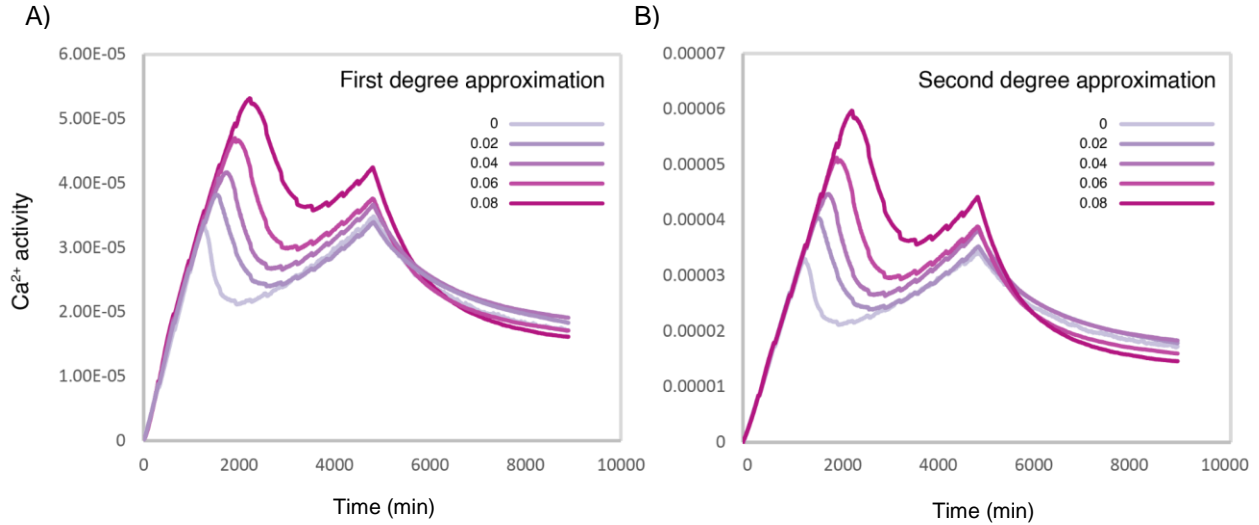
Figure 4.3: Ca^{2+} activity datasets corresponding the experiments with specific nominal Zn/Si ratios (numbered in the legends) and calibrated with A) a first-degree Nernst equation and B) a second-degree Nernst equation.

An important observation for this first set of data is that as the zinc increases a higher supersaturation is reached before precipitation. Consequently, an increasing content of zinc leads to a retardation in the precipitation, which is consistent with the retardation observed in C_3S systems as published by Li et al.[14] All the curves have a slope after precipitation which increases as more calcium is added into the system. This feature, in which the apparent supersaturation increases to the same level as in the precipitation first peak (at least in the case of conventional C-S-H), was not observed during the precipitation of amorphous calcium carbonate or ettringite and will further be discussed in section 4.4. All signals display step-like features, but these steps correspond to the moments where the syringe containing the calcium nitrate solution is being recharged.

4.3.2 Morphology of C-S-H and zinc-modified C-S-H during precipitation

The morphology of the precipitate at different reaction times was studied by means of S/TEM. Aliquots of the solution as the reaction was progressing were taken for TEM analysis at the following stages of reaction (for the cases with $(Zn:Si)_i=0$ and $(Zn:Si)_i=0.08$):
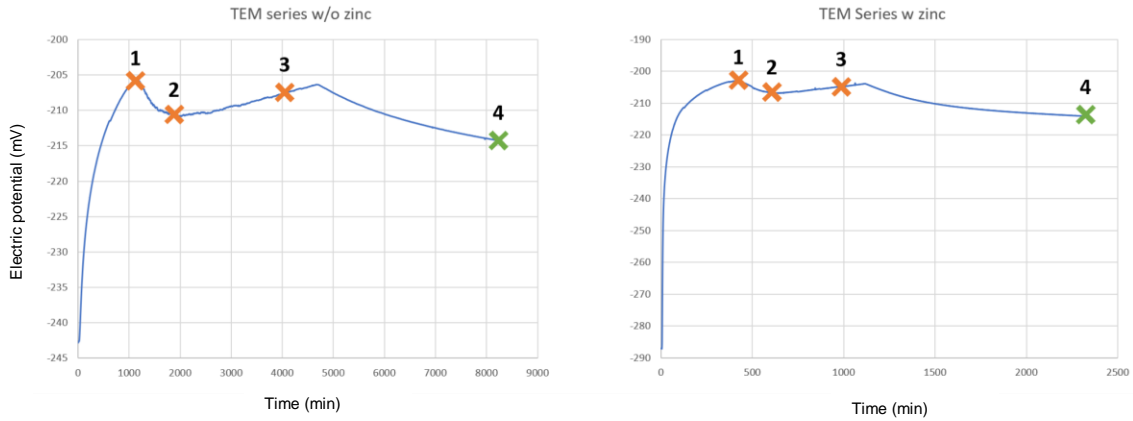
Figure 4.4: Uncalibrated as-obtained electrical potential datasets showing when aliquots were taken to carry out TEM for A) the precipitation of conventional C-S-H with $(Zn:Si)_i=0$, and B) the precipitation of zinc-modified C-S-H $(Zn:Si)_i=0.08$.

A series of the TEM micrographs corresponding to these aliquots, spaced in order to study the evolution of C-S-H's morphology over time, are shown in Figures 4.5 and 4.6.
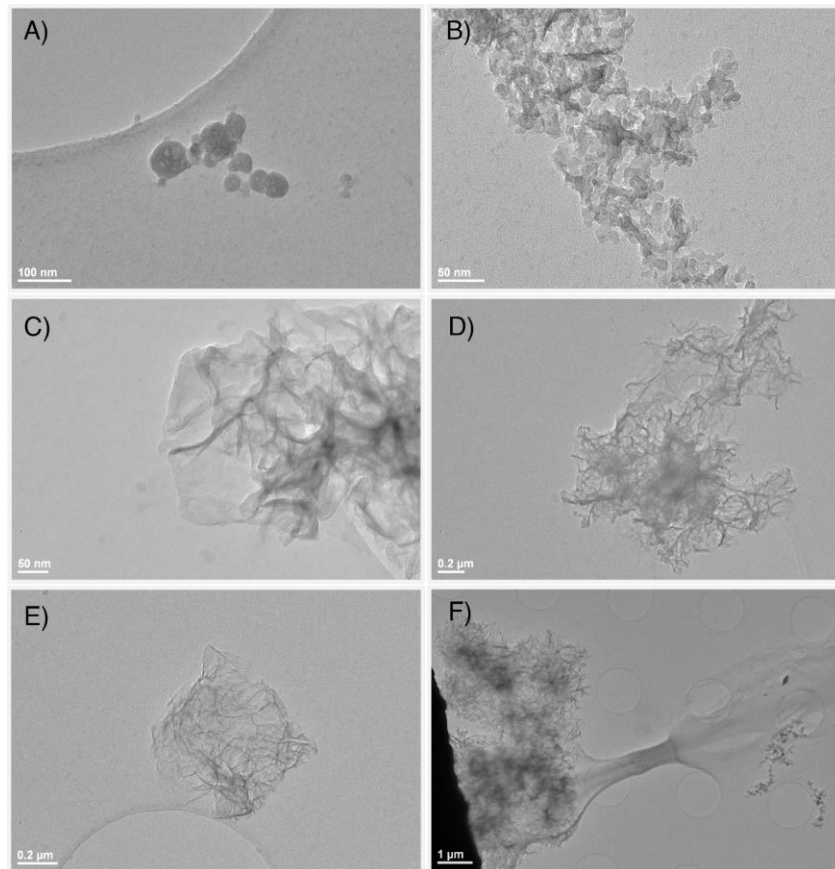
Figure 4.5: STEM micrographs of conventional C-S-H $(Zn:Si)_i = 0$ at different stages of the precipitation experiments. A and B) correspond to point 1, where precipitation starts. C and D) correspond to point 2,

at the valley of calcium activity. And E and F) correspond to point 3, moments before stopping the calcium addition.
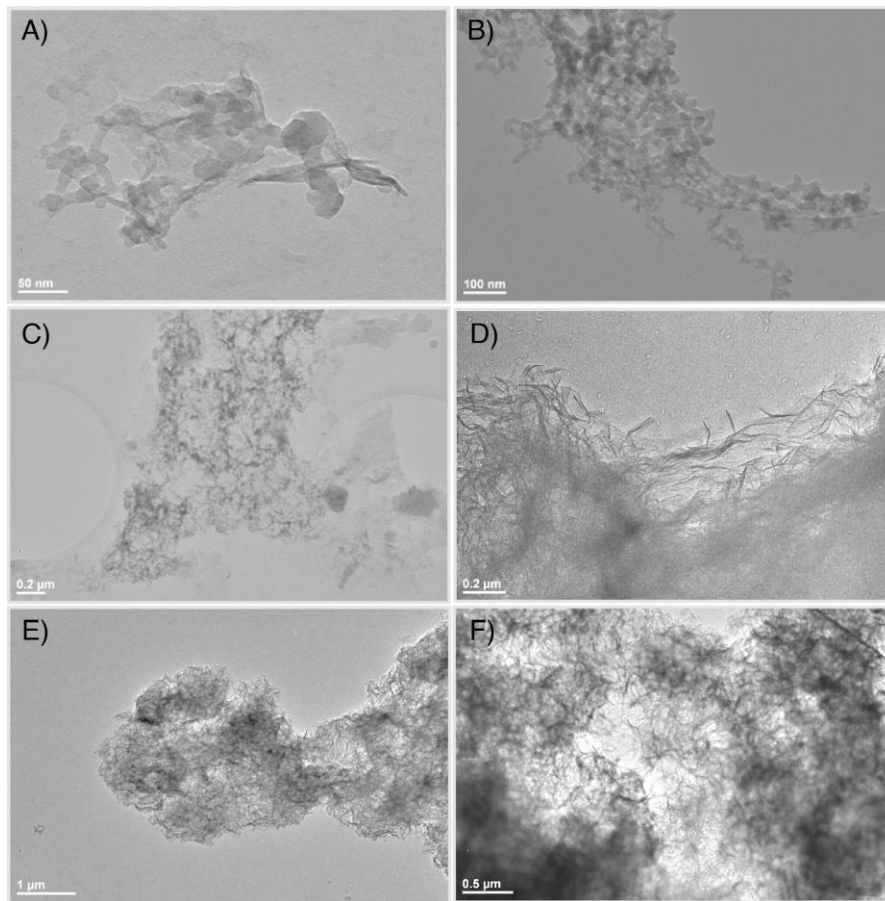
Figure 4.6: STEM micrographs of zinc-modified C-S-H with $(Zn:Si)_i$ = 0.08 at different stages of the precipitation experiments. A and B) correspond to point 1, where precipitation starts. C and D) correspond to point 2, at the valley of calcium activity. And E and F) correspond to point 3, moments before stopping the calcium addition.

This TEM study reveals that a more amorphous and apparently globular kind of C-S-H precipitates first, which then rapidly transforms into foil-like C-S-H. This result is analogous to the observations of other research groups.[15–17] Apparent differences between samples with and without zinc are not observable only through TEM and analysis of the size distribution is difficult due to agglomeration and scarcity of particles.

4.3.3 A comprehensive model for C-S-H precipitation

In this section, our preliminary model for C-S-H precipitation is put to test with two samples. First, the case for conventional C-S-H precipitation $(Zn:Si)_i$=0 is discussed. Then, the model is extended to zinc-modified C-S-H (sample with $(Zn:Si)_i$=0.08). This preliminary model gives several insights, but also raises

questions and need to be adjusted to include new theories and equations, a process that will be discussed in section 4.4.

Speciation and internal checks

Our model is comprehensive and considers both thermodynamic and kinetic processes in C-S-H precipitation. Thanks to this complex set of equations, important information such as the speciation of the system can be computed, as is shown in Figure 4.7.
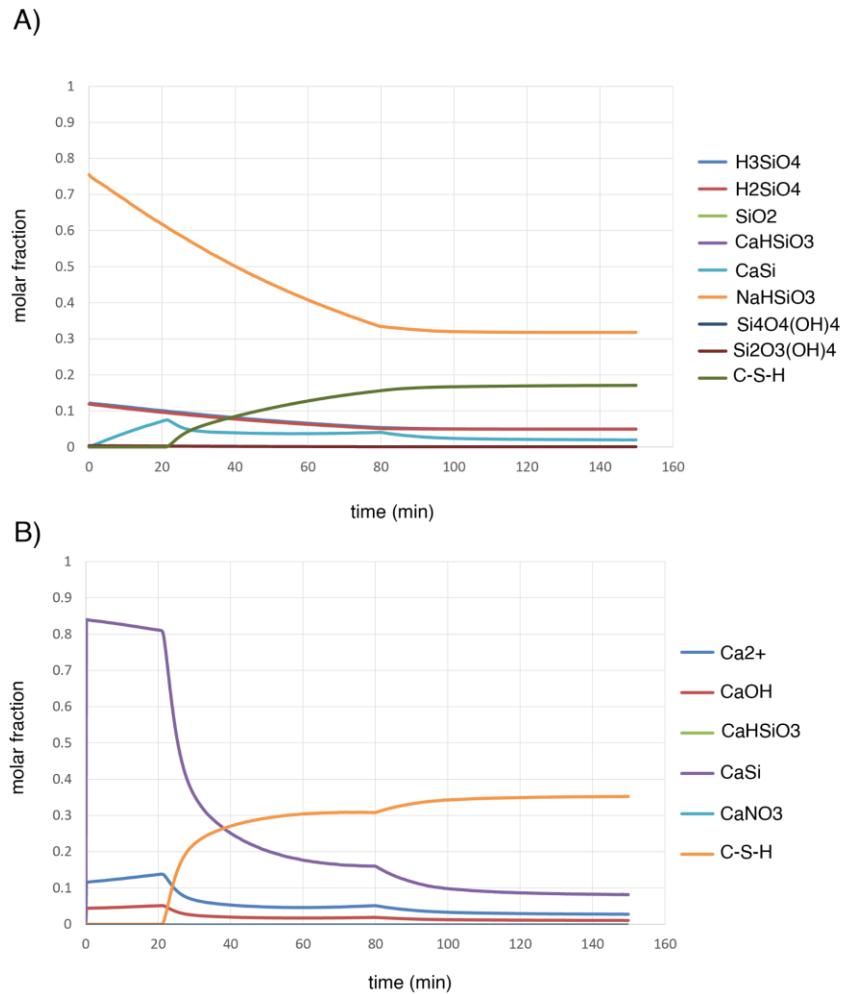
Figure 4.7: Speciation of A) silicon species and B) calcium species expressed in molar fraction as a function of experimental time for a sample with $(Zn:Si)_i$=0.

The results show consistency in the speciation, a decrease of all species in solution is seen as C-S-H precipitates and also shows different slopes when calcium addition is stopped at around 80 min. Additionally, the model allows for the calculation of the nucleation rates (B_{homo} and B_{sec}) at any moment during the reaction. Primary nucleation starts at around 20 min, and secondary nucleation is negligible. This is a strange feature, since almost all materials present secondary nucleation at some point during the

process of precipitation, and since previous work carried out by Reza et al.[2] found that secondary nucleation is an important event. This will be discussed in more depth further in this text.

Our model allows consistency to be verified with two internal checks: the total volume of NaOH added, which is compared to the volume of NaOH that is calculated by the model (see Figure 4.8A), and the population balance equations, whose results should always be very close to zero (see Figure 4.8B).
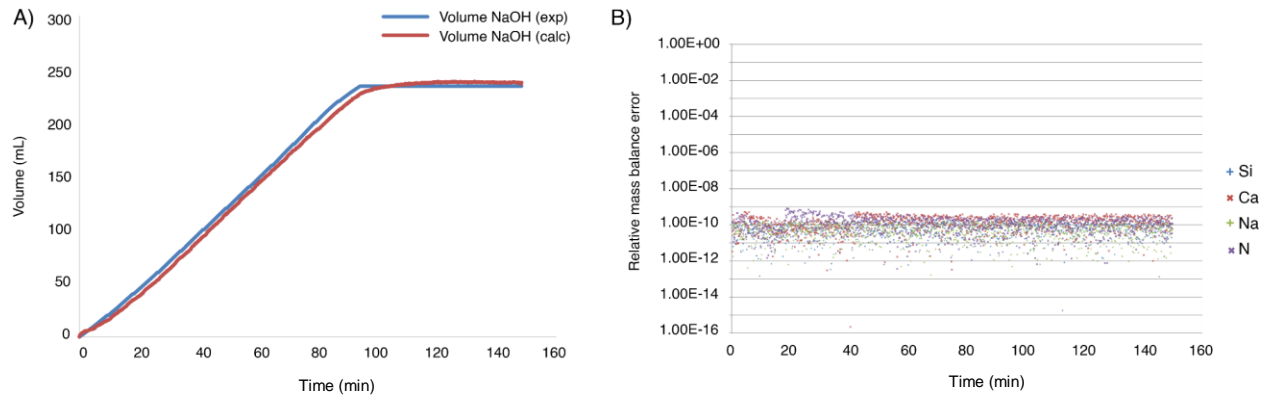
Figure 4.8: A) Experimental and calculated NaOH volume added during a precipitation experiment (for an experiment with (Zn:Si)$_i$=0). B) Mass balance error for the four elements in the mass balance equations (for an experiment with (Zn:Si)$_i$=0).

These results demonstrate consistency between experiments and the model and self-consistency in the model, and serve as a tool to verify that thermodynamic and kinetic equations are calculated appropriately.

Calcium activity, saturation and fitting

Our thermodynamic and kinetic approach was first used to model the calcium activity dataset corresponding to the precipitation of conventional C-S-H and calibrated with a second-degree Nernst equation. Considering spherical nuclei that undergo growth in all directions, the model correctly predicts the activity of Ca^{2+} during pre-precipitation, as well as during the signal decrease after precipitation, as is shown in Figure 4.9. However, under the aforementioned conditions, the model predicts a much flatter signal afterwards, while our data shows a steady increase of the Ca^{2+} signal and apparent supersaturation after the precipitation.
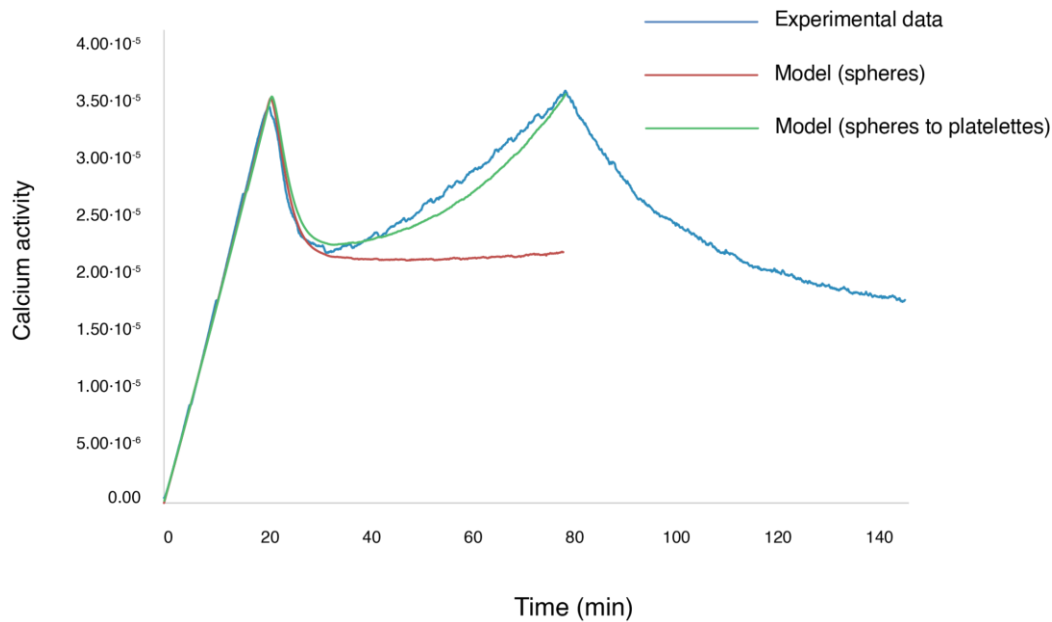
Figure 4.9: Experimental data (blue) compared to our thermodynamic and kinetic models, which consider only spherical particles growing in all directions (red), or spherical particles that nucleate and rapidly transition to a platelet shape (green).

It appears that there are features absent in this preliminary model that lead to the slope increasing after precipitation. This might indicate that the growth of C-S-H is restricted, since the increase of the Ca^{2+} signal could mean that calcium is dosed at a rate that is faster than the rate at which it is integrated in C-S-H. This hypothesis would also agree with what we know about the morphology of synthetic C-S-H, which grows in the shape of nanofoils or platelets, displaying a 2D shape, as seen in the TEM study above. So, it can be hypothesized that the growth mechanism is restricted by its dimensionality.

In order to implement this restricted growth hypothesis, an additional function was added to the model which takes the volume (m_4) of a spherical particle and finds the respective percentage of available surface assuming the shape is a flat square platelet with a thickness (which can be tuned in the input file). The growth is restricted only to the edge of this platelet which corresponds to an area that is 4 times the length (L) multiplied by the thickness (t) of this square platelet, as is depicted in Figure 4.10. The optimal width of the platelets is found to be 5 nm, suggesting that there are 2-3 C-S-H sheets sandwiched together, which agrees with several computational studies about the atomic structure of C-S-H. This function has an additional feature, which allows for a gradual transition from the sphere model to the platelet model, since the sphere model matches our experiments better up until the minimum, but the platelet model fits better after this minimum.
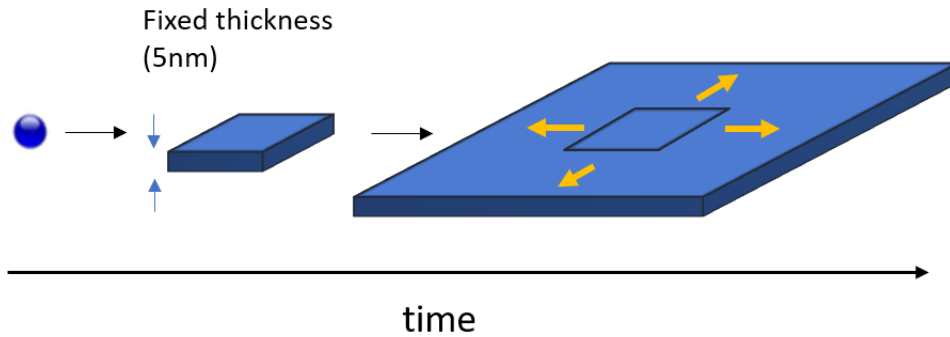
Figure 4.10: Schematic showing the transition from spheres to platelets implemented in the model.

Finally, our model also predicts the final activity value of the end-member after equilibration, showing a fit that, although not perfect, is very good within reason. Figure 4.11 shows a final fit along with the plot of saturation (S). The final values of the parameters that were tuned: the solubility product (K_{sp}) and the homonuclear surface energy (γ_{homo}), were found to be **$5.6 \cdot 10^{-7}$** and **$12.1 \cdot 10^{-3}$ N/m**, respectively. In addition, secondary nucleation is negligible with this specific model.
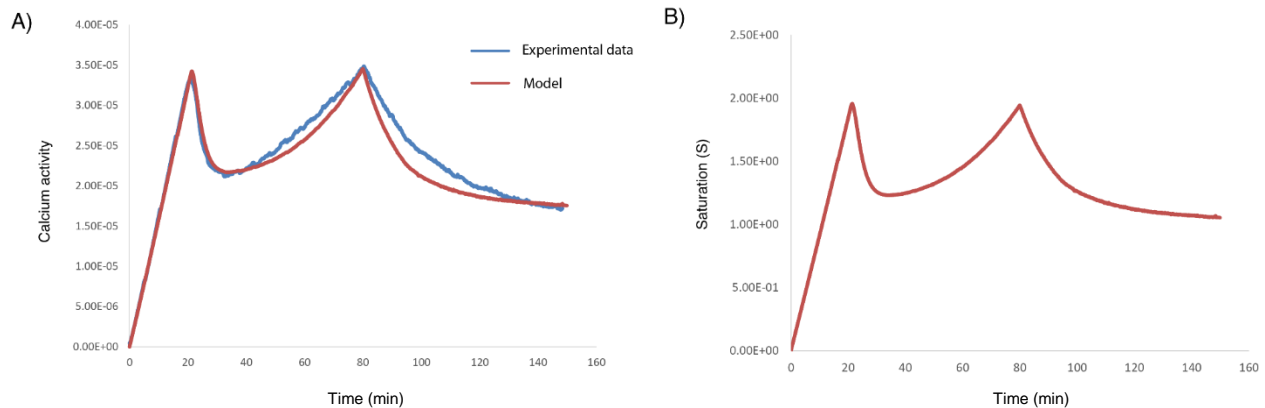
Figure 4.11: A) Best fit (red) compared to the experimental data (blue) of a synthetic conventional C-S-H precipitation experiment with matching experimental conditions: pH 12.82 ± 0.02, 20 ℃ and the concentrations shown in Table 4.1 for the sample with $(Zn:Si)_i$=0. B) The calculated saturation plot corresponding to the same experiment.

Although the sphere/platelet hypothesis might be correct and a restricted growth could be happening, an external constraint must be introduced in the model which forbids the supersaturation (S) to continue increasing over the level of the first peak if more calcium is added into the system. This is not ideal, as it lacks physical meaning and shows how the model is not totally consistent with experiments, where a second precipitation does not occur after 80 min, a fact that needs to be enforced externally in the model. An in-depth discussion about the validity of the sphere/platelet transition is provided in Section 4 since it

is still a matter of debate, and the model is now being modified to incorporate a new hypothesis regarding this apparent increase in saturation (S).
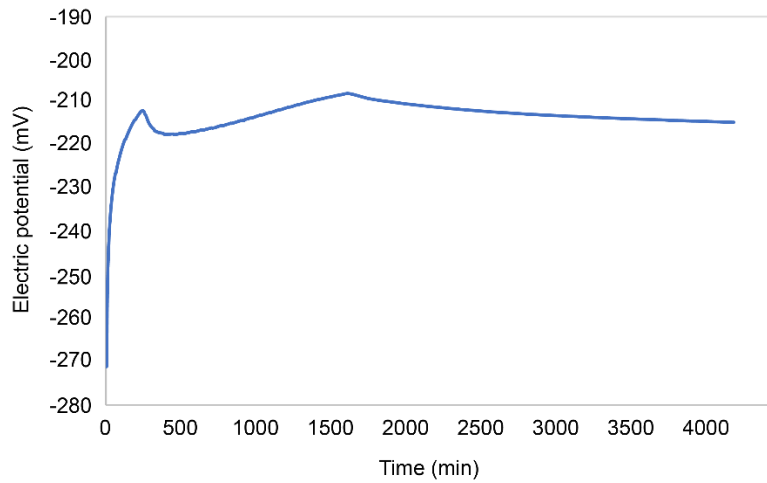
Figure 4.12: Uncalibrated electric potential dataset in which 250 mL of the calcium nitrate solution have been dosed (instead of 150 mL, as previously). A second precipitation is not observed.

Extension of the model to zinc-modified C-S-H

The model was extended to include zinc by adding the speciation of species containing this element, by extending Kersten's definition of K_{sp}, and by adapting the stoichiometry of the new possible end-members with the addition of the index z; all of these steps were discussed in more detail in Section 2.5. The model with zinc can also be used to describe conventional C-S-H just by setting $z=0$. Interestingly, the saturation (S) level does not seem to increase as much after precipitation as it does in the case of conventional C-S-H.
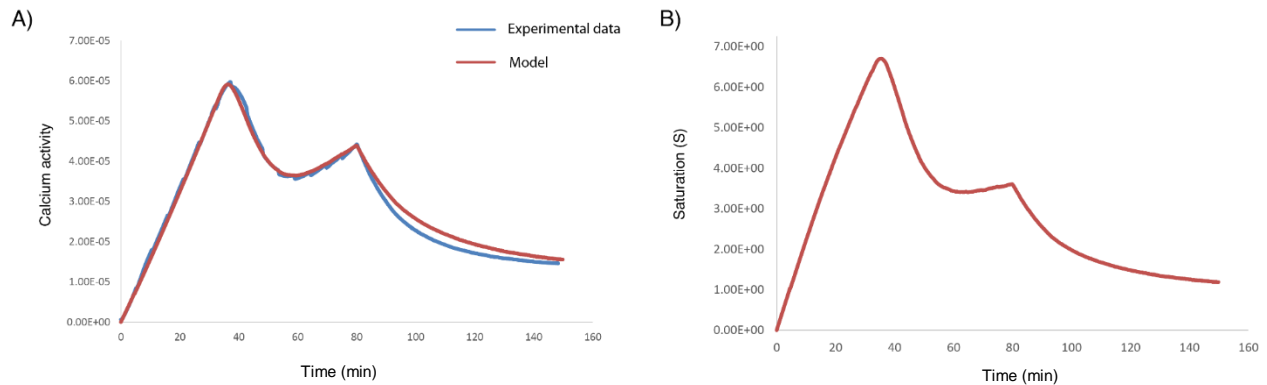
Figure 4.13: Our model's best fit (red) compared to the experimental data (blue) of a synthetic conventional C-S-H precipitation experiment with matching experimental conditions: pH 12.82 ± 0.02, 20 °C and the concentrations shown in Table 4.1 for the sample with $(Zn:Si)_i=0.08$.

70

In summary, our preliminary model is able to use the thermodynamic and kinetic equations governing the precipitation of C-S-H and compute the activity of calcium both when zinc is present in solution and when it is not. The model allows for the calculation of important data such as the speciation of the system over time, the NaOH volume added, the total volume and the mass balance error. Also, our data consistently presents a feature that has not been seen before in previous similar experiments with this kind of set-up:[6,18] as calcium is continuously added in the reactor, the curve corresponding to the growth of C-S-H continues to increase.

Our model tries to account for this by introducing an external function which limits growth to only a percentage of the surface (the edge of the platelets). Although after the implementation of this function the model fits our data nicely, according to this same model, the supersaturation (S) increases back to the point where the system should undergo a second precipitation event (at least in the case of $(Zn:Si)_i=0$). Experiments with longer calcium doses (at the same rate) show that this second precipitation event does not occur (Figure 4.12). This preliminary model needs then to account for different mechanisms governing the nucleation and growth of C-S-H, and the necessity of invoking a transition from spheres to platelets needs to be critically analyzed and compared to other hypotheses as to why the activity of calcium continues to increase during growth.

4.4 Outlook

This section elaborates on the questions that arise from our data and model and proposes an experimental plan to verify the current hypotheses. First, the fact that a second-degree Nernst equation is necessary to calibrate the data of zinc-modified C-S-H is discussed. Secondly, the hypotheses as to why there is an apparent supersaturation (S) increase are put forward. Then, the changes that are currently being implemented in the model are discussed. Finally, an experimental plan for the continuation of this work is proposed.

4.4.1 Zinc incorporation and the problem with calibration

As previously shown in Figure 4.3, the addition of zinc delays the precipitation of C-S-H and allows for higher calcium activities before precipitation. This could potentially be explained through the complexation of silicate-zincate anions, whose formation in solution was described by Anseau et al,[19] and calcium cations.
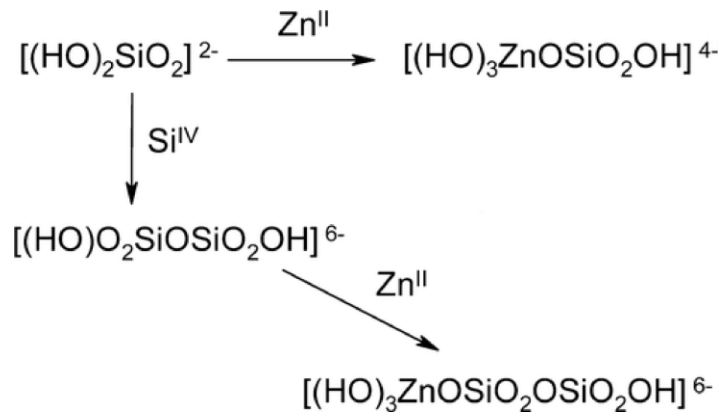
Figure 4.14: Schematic of the zinc-silicon species proposed in Anseau et al.[19]

The presence of complexes could also explain why the curves don't follow a linear trend in the case of zinc-modified C-S-H after being calibrated with the conventional Nernst equation, since any thermodynamic or kinetic event which is not well understood and implemented could be behind this feature, which is only seen when zinc is present during precipitation. Unraveling what occurs before precipitation and the species that are present should be a major focus in future work.

4.4.2 The calcium activity increase during growth

One of the main features of our datasets is the fact that the calcium activity increases dramatically during the growth stage of conventional C-S-H. There are two main hypotheses as to why this could be happening. First, the growth could be restricted due to C-S-H's dimensionality, and hence the rate of addition of calcium nitrate would be faster than the rate of calcium incorporation in C-S-H. This hypothesis was implemented in the model and tested, as previously discussed, and resulted in a proper fit which can model the behavior of calcium activity during our experiment. Despite the success of the fit, this model cannot properly determine the supersaturation (S) of the system, as it needs to invoke an external constraint to avoid a second precipitation event. The hypothesis of a transition between spheres to platelets with restricted available surface is then not sufficient, if even necessary at all, to model the precipitation of C-S-H and other hypotheses need to be considered.

A plausible hypothesis to explain the apparent increase in supersaturation (S) is the presence of **out-of-equilibrium species**. Until now we have only considered speciation equations where the reaction rates k and k$_{-1}$ were equal, with a resulting equilibrium constant K. This is not always the case. It seems plausible that the silicon species that participate in the formation of C-S-H (the silicate monomers in the preliminary model) are formed slowly, and that the calcium activity increases due to the scarcity of these silicon species. The saturation (S) can also be affected by this, since both the silicate and the calcium species are present in its description. If an out-of-equilibrium silicate species is considered, the actual saturation (S) could be lower than what we have calculated with the sphere/platelet model. The changes, implementations and new considerations that are being currently added to the model are discussed below.

4.4.3. Changes in the model

After the first draft of this thesis, the model has undergone some changes, as the behavior of the saturation level did not make physical sense. According to Kulik and Kersten,[11] the end-members can be described more generally according to:

$$(T5) = 4Ca(OH)_2 \cdot 5SiO_2 \cdot 4H_2O \leftrightarrow \frac{5}{2}Si_2O_3(OH)_4^{2-} + 4CaOH^+ + 4H_2O \tag{48}$$

$$(J5) = 10Ca(OH)_2 \cdot 5SiO_2 \cdot 4H_2O \leftrightarrow \frac{5}{2}Si_2O_3(OH)_4^{2-} + 10CaOH^+ + 4H_2O \tag{49}$$

$$Zn(OH)_2 + 2OH^- \leftrightarrow Zn(OH)_2^{2-} \tag{50}$$

$$(Zn:CSH) = (1-z)[(1-y)T5 \cdot (y)J5] \cdot z[aZn_{Si}(OH)_2 + (1-z)Zn_{Ca}(OH)_2] \tag{51}$$
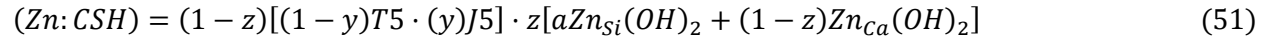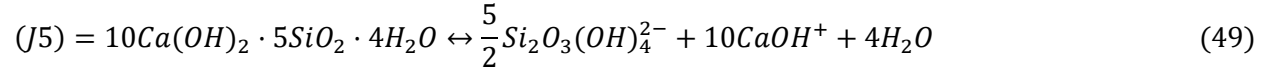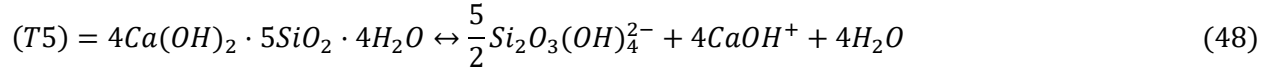
Where a tobermorite-like end-member (T5) and a jennite-like end-member (J5) are used to describe the material; and where the subscripts *Si* and *Ca* refer to a zinc atom substituting for a silicon or a calcium, respectively. To simplify, we can write:

$$Q_1 = (1-z)(4+6y) \tag{52}$$

$$Q_2 = 5(1-z) \tag{53}$$

$$Q_3 = z \tag{54}$$

$$Q_4 = 6y(z-1) + z - 1 \tag{55}$$

This description is more general than our previous description of the end-members and encompasses solid-solutions with a wider range of Ca:Si ratios. The activity and the solubility products can then be expressed in a more general fashion as:

$$IAP = \{CaOH^+\}^{Q_1}\{Si_2O_3(OH)_4^{2-}\}^{Q_2}\{Zn(OH)_4^{2-}\}^{Q_3}\{H^+\}^{Q_4} \tag{56}$$

$$Ksp_{C-Z-S-H} = \{CaOH^+\}_{eq}^{Q_1}\{Si_2O_3(OH)_4^{2-}\}_{eq}^{Q_2}\{Zn(OH)_4^{2-}\}_{eq}^{Q_3}\{H^+\}_{eq}^{Q_4} \tag{57}$$

Additionally, to keep the growth model more general, instead of considering a specific species in the growth mechanism and using the platelet hypothesis, the applied growth model has changed to the form:

$$\hat{G} = \alpha \cdot log^\beta(S) \tag{58}$$

73

Where $\hat{G}$ is the average growth term in eq. 58 and α and β are adjustable parameters. The drawback of this equation is that the two adjustable parameters do not now have a physical meaning, identifying a generic unknown growth mechanism, which can be a complex process involving several unknown species and making this model also empirical, after all.

A direct consequence of these changes, which are an updated version of the model and that can be applied to describe materials more generally, is the change in behavior of the saturation curve as the experiment progresses. With the changes implemented, no second precipitation is predicted with the model providing a more physically consistent result, as is shown below:
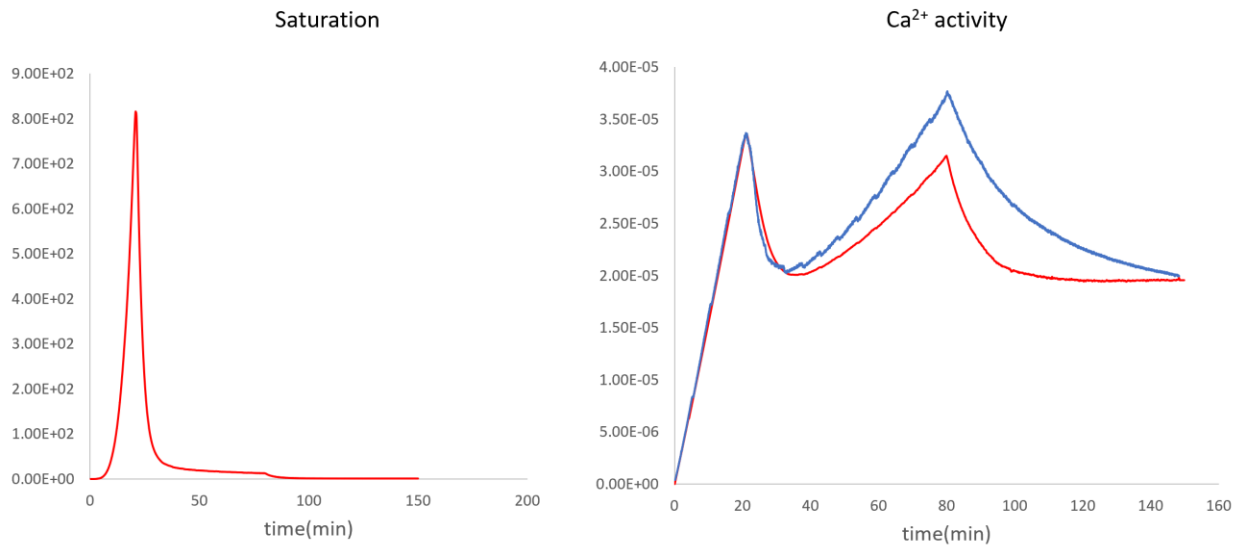
Figure 4.14: Saturation and calcium activity curves of the updated model.

4.4.4 Further experiments

There are several lines of work and proposed experiments which will help validate and finalize this model. First, the adaptation of the model to include out-of-equilibrium species needs to be perfected. Second, a series of dropwise precipitation experiments where conventional C-S-H is precipitated will be conducted at slightly different pH. This will help validate the hypothesis of the presence of out-of-equilibrium species, since a different pH translates into a different number of protons in solution, which will modify eq. 12. If the results show different calcium activity slopes in the growth regime at different pH, the presence of out-of-equilibrium species will be further supported.

Additionally, NMR experiments might shine light on the kinds of species which are present before precipitation and validate or help discard the hypothesis that there is some kind of complexation. The experiment which can help elucidating exactly what species are found before precipitation and during the formation of C-S-H is hyperpolarized real-time DNP NMR,[20] in which the sample is hyperpolarized through the rapid mixing with a radical and then sent to the magnet to be subject to microwaves (to enhance the

74

signal though DNP) and analyzed. Other experiments which have been a matter of discussion and will potentially be part of this project in the future are in-situ Raman spectroscopy, or Small-Angle X-Ray spectroscopy.

4.5 Conclusions

High-quality calcium activity datasets were collected during the precipitation of conventional C-S-H and zinc-modified C-S-H. Data shows how the precipitation of C-S-H is delayed upon zinc incorporation, which could potentially be due to the presence of zinc-silicate and calcium complexes.

A comprehensive thermodynamic and kinetic model has been developed. This preliminary model successfully calculates the speciation, the volumes, the mass balances and the calcium activity of our experiments, as well as the solubility products and the homogeneous surface energies. However, the model fails to describe the evolution of the saturation of the system, as the apparent saturation increases beyond the point where a second precipitation should take place. Therefore, the model is being updated to incorporate a new hypothesis to explain the increase in calcium activity during growth: the presence of out-of-equilibrium reactions.

The introduction of an out-of-equilibrium reaction involving the silicate species that participates in the formation of C-S-H (which are silicate dimers in this hypothesis), along with a more generic description of K_{sp} result in a saturation curve which only reaches supersaturation when nucleation takes place, and then decreases to a plateau. This change should result in a consistent saturation (S) curve and implies the fact that an external constraint doesn't need to be invoked. Additionally, there is no need to constrain the surface available for growth with the implementation of this hypothesis. This model is now being finalized, since introducing out-of-equilibrium equations implies a more complicated system and empirical factors which are now being tuned to properly fit our data.

In summary, quality data was gathered which shows features and insights that had never been observed in C-S-H before. A solid framework has been established for the thermodynamic and kinetic study of C-S-H and C-S-H-related materials and further experiments will involve extensive NMR and Raman studies to unravel the species present before precipitation, and more dropwise precipitations with different conditions to confirm the presence of out-of-equilibrium equations.

4.6 References

(1)   Krautwurst, N.; Nicoleau, L.; Dietzsch, M.; Lieberwirth, I.; Labbez, C.; Fernandez-Martinez, A.; Van Driessche, A. E. S.; Barton, B.; Leukel, S.; Tremel, W. Two-Step Nucleation Process of Calcium Silicate Hydrate, the Nanobrick of Cement. *Chemistry of Materials* **2018**, *30* (9), 2895–2904. https://doi.org/10.1021/acs.chemmater.7b04245.

(2)   Andalibi, M. R.; Kumar, A.; Srinivasan, B.; Bowen, P.; Scrivener, K.; Ludwig, C.; Testino, A. On the Mesoscale Mechanism of Synthetic Calcium-Silicate-Hydrate Precipitation: A Population Balance Modeling Approach. *J Mater Chem A Mater* **2018**, *6* (2), 363–373. https://doi.org/10.1039/c7ta08784e.

(3)   Kazmierczak, T. F.; Tomson, M. B.; Nancollas, G. H. Crystal Growth of Calcium Carbonate. A Controlled Composition Kinetic Study. *J Phys Chem* **1982**, *86* (1), 103–107.

(4)   Tomson, M. B.; Nancollas, G. H. Mineralization Kinetics: A Constant Composition Approach. *Science (1979)* **1978**, *200* (4345), 1059–1060.

(5)   Gebauer, D.; Cölfen, H. Prenucleation Clusters and Non-Classical Nucleation. *Nano Today* **2011**, *6* (6), 564–584.

(6)   Carino, A.; Testino, A.; Andalibi, M. R.; Pilger, F.; Bowen, P.; Ludwig, C. Thermodynamic-Kinetic Precipitation Modeling. A Case Study: The Amorphous Calcium Carbonate (ACC) Precipitation Pathway Unravelled. *Cryst Growth Des* **2017**, *17* (4), 2006–2015.

(7)   Wang, P.; Anderko, A.; Young, R. D. A Speciation-Based Model for Mixed-Solvent Electrolyte Systems. *Fluid Phase Equilib* **2002**, *203* (1–2), 141–176.

(8)   Morales-melgares, A.; Casar, Z.; Moutzouri, P.; Venkatesh, A.; Cordova, M.; Bowen, P.; Scrivener, K.; Emsley, L. Atomic-Level Structure and Kinetics of Synthetic Zinc-Modified C-S-H. **2022**, *97* (2), 3693.

(9)   Kersten, M. Aqueous Solubility Diagrams for Cementitious Waste Stabilization Systems. 1. The CSH Solid-Solution System. *Environ Sci Technol* **1996**, *30* (7), 2286–2293.

(10)   Kulik, D. A.; Kersten, M. Aqueous Solubility Diagrams for Cementitious Waste Stabilization Systems: II, End-member Stoichiometries of Ideal Calcium Silicate Hydrate Solid Solutions. *Journal of the American Ceramic Society* **2001**, *84* (12), 3017–3026.

(11)   Becker, R.; Döring, W. Kinetische Behandlung Der Keimbildung in Übersättigten Dämpfen. *Ann Phys* **1935**, *416* (8), 719–752.

(12)   Backus, J. W.; Heising, W. P. Fortran. *IEEE Transactions on Electronic Computers* **1964**, No. 4, 382–385.

(13)   Li, X.; Scrivener, K. L. Impact of ZnO on C3S Hydration and CSH Morphology at Early Ages. *Cem Concr Res* **2022**, *154*, 106734.

(14)   Plank, J.; Schönlein, M.; Kanchanason, V. Study on the Early Crystallization of Calcium Silicate Hydrate (CSH) in the Presence of Polycarboxylate Superplasticizers. *J Organomet Chem* **2018**, *869*, 227–232.

(15)   Schönlein, M.; Plank, J. A TEM Study on the Very Early Crystallization of CSH in the Presence of Polycarboxylate Superplasticizers: Transformation from Initial CSH Globules to Nanofoils. *Cem Concr Res* **2018**, *106*, 33–39.

(16) Shen, X.; Feng, P.; Liu, X.; Wang, W.; Zhang, Y.; Zhou, Y.; Ran, Q. New Insights into the Non-Classical Nucleation of CSH. *Cem Concr Res* **2023**, *168*, 107135.

(17) Testino, A.; Buscaglia, M. T.; Buscaglia, V.; Viviani, M.; Bottino, C.; Nanni, P. Kinetics and Mechanism of Aqueous Chemical Synthesis of BaTiO3 Particles. *Chemistry of materials* **2004**, *16* (8), 1536–1543.

(18) Anseau, M. R.; Leung, J. P.; Sahai, N.; Swaddle, T. W. Interactions of Silicate Ions with Zinc (II) and Aluminum (III) in Alkaline Aqueous Solution. *Inorg Chem* **2005**, *44* (22), 8023–8032.

(19) Weber, E. M. M.; Kress, T.; Abergel, D.; Sewsurn, S.; Azaïs, T.; Kurzbach, D. Assessing the Onset of Calcium Phosphate Nucleation by Hyperpolarized Real-Time NMR. *Anal Chem* **2020**, *92* (11), 7666–7673.

Contents

5. Conclusions

This thesis focused on the role of zinc in C-S-H to throw light on its dramatic effect on hydration kinetics. The first part of the experimental work focused on studying the atomic-level structure of zinc-modified C-S-H, while the second part of the experimental work focused on the development of a population balance-based thermodynamic and kinetic model to describe the nucleation and growth mechanisms of both C-S-H and zinc-modified C-S-H.

5.1 Contributions on the atomic-level structure of zinc-modified C-S-H

5.1.1 New silicate and zinc sites

Through a combination of DNP-enhanced 1D $^1H\rightarrow^{29}Si$ multi-CPMAS and natural-abundance 2D ^{29}Si-^{29}Si INADEQUATE NMR experiments, and DFT calculations of relaxed structures and chemical shifts, it was found that there are four possible new silicate sites in the structure upon zinc incorporation: $Q^{(1,Zn)}$, $Q^{(2p,Zn)}$, $Q^{(1,Zn\_int)}$ and $Q^{(2p,2Zn)}$. From these, the two more plausible silicate sites which are present in the samples are $Q^{(1,Zn)}$ and $Q^{(2p,Zn)}$. Two sites are identified for the incorporation of octahedrally coordinated zinc oxyhydroxide species ($ZnO_2(OH)_2^{4-}$), which readily substitute for $Q^{(1)}$ and bridging sites, unlike aluminium ions, which can only incorporate in the bridging sites in all coordinations.[1]

5.1.2 Increased mean chain length

The incorporation of zinc has a significant effect on the mean chain length (MCL) of the dreierketten C-S-H chains. A combined Q site analysis carried out with the 1D $^1H\rightarrow^{29}Si$ multi-CPMAS and 2D ^{29}Si-^{29}Si INADEQUATE spectra, showed that the MCL is increased from around 2.9 to 3.2 when the Zn/Si ratio is 0.15, and from 2.9 to 4.5 when the Zn/Si ratio is 0.40 (see Figure 5.1A). The increase in MCL could potentially be correlated to the accelerated hydration kinetics of zinc-containing cements since the effective growth units (zinc and silicon) in solution is increased.
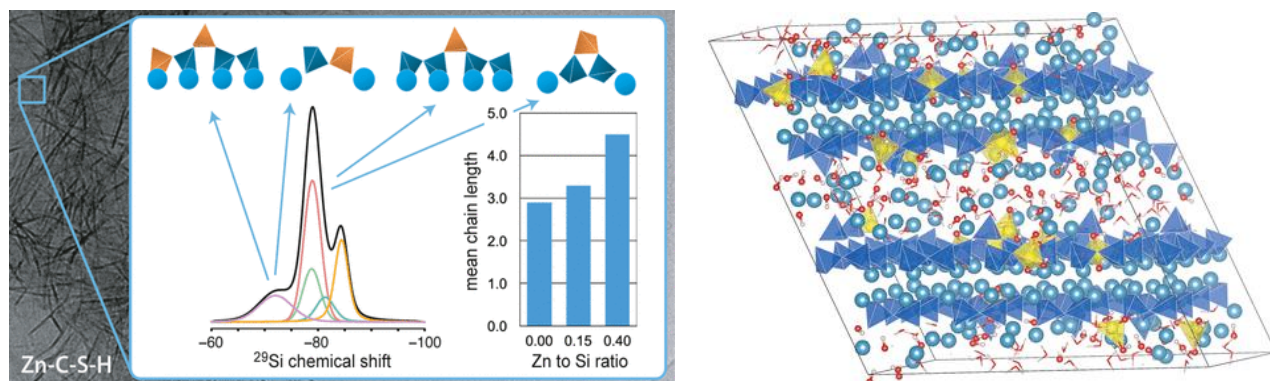

Figure 5.1: A) Composite scheme showing the four possible new zinc sites in zinc-modified C-S-H and mean chain lengths (MCL) for samples with (Zn/Si)$_i$ of 0, 0.15 and 0.40. B) Schematic representation of the as-determined atomic-level structure of zinc modified C-S-H with a (Zn/Si)$_i$ of 0.15.

5.2 Contributions on thermodynamic-kinetic modeling of C-S-H

The nucleation and growth mechanisms behind the formation of C-S-H and zinc-modified C-S-H were investigated by gathering thermodynamic and kinetic data which consisted in high-quality calcium activity datasets that were collected during the precipitation of C-S-H.

5.2.1 Precipitation delay upon zinc incorporation

C-S-H precipitation was delayed as the concentration of zinc in solution was increased and the system required higher supersaturation levels for precipitation to occur. This could potentially be due to the presence of complexes or unknown kinetic processes. Additionally, calibrated zinc-modified C-S-H datasets showed a non-linear trend, which points to the presence of complexes or kinetic events prior to precipitation which are yet unknown.

5.2.2 A preliminary comprehensive thermodynamic and kinetic model

A preliminary thermodynamic and kinetic comprehensive model was developed in FORTRAN[2] by considering the classical nucleation thermodynamic and kinetic expressions (eq. 1-46, Chapter 4) which define C-S-H and zinc-modified C-S-H. This preliminary model can calculate various properties of C-S-H precipitation experiments, such as speciation, volumes, mass balances, calcium activity, solubility products, and surface energies.

Transition from spheres to platelets theory

The collected datasets presented a feature that had never been observed before in these kinds of precipitation set-ups:[3,4] that the activity of calcium increased after precipitation to the point of reaching at least the same level it had during nucleation. Seemingly, calcium cannot be incorporated in C-S-H as fast as it is being added to the reactor. This issue was addressed by the incorporation of a function which limits the growth only to the edge of particles, so that particles evolve from small 3D spheres to 2D platelets. The addition of this theory is supported by:

- A very good fit between the calculated and the experimental data (see Figure 5.2).
- Several morphology studies show a transition from globules to foils.[5,6]
- TEM micrographs from our samples that show a globule-like morphology at the very early stages of precipitation.

However, the incorporation of this theory has several inconsistencies which point to it being either incomplete or incorrect:

- The apparent saturation increases over the point where a second precipitation should occur, which does not happen experimentally.
- Relating to the previous point, the increase in supersaturation must be constrained externally in the model to avoid the prediction of a second precipitation. This is not ideal as it lacks physical meaning and points to the sphere-platelet hypothesis being wrong.
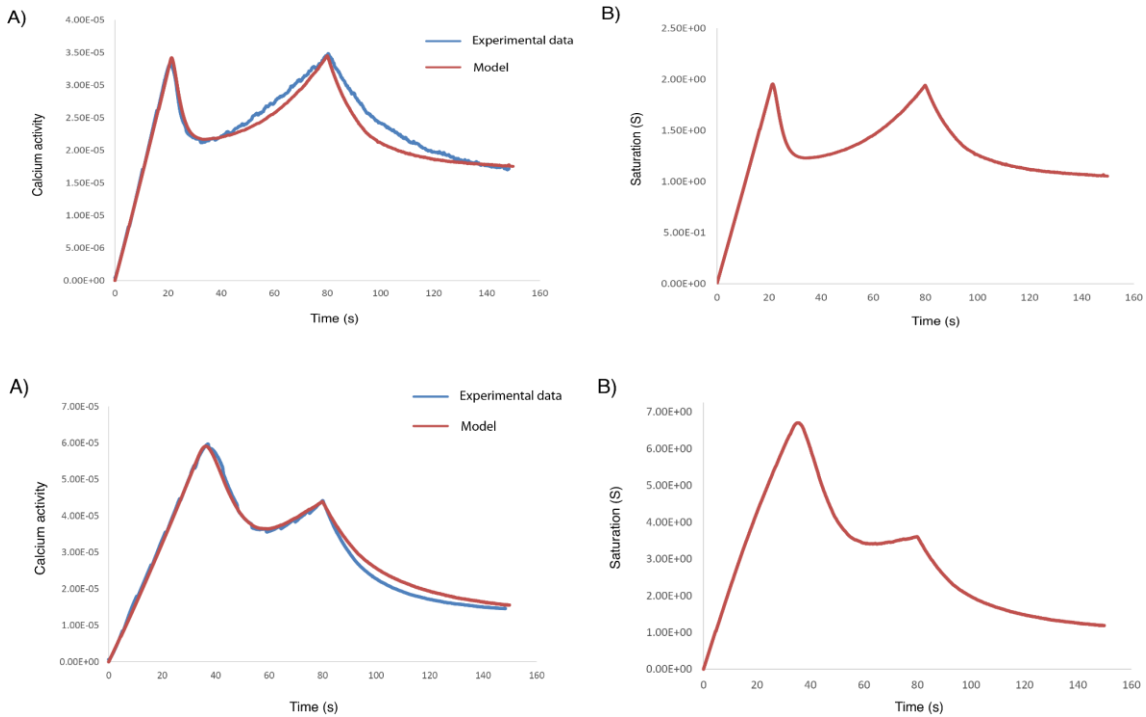
Figure 5.2: A) Experimental data vs calculated data from our model for a sample with (Zn/Si)$_i$ of 0 and B) its respective saturation curve. C) Experimental data vs calculated data from our model for a sample with (Zn/Si)$_i$ of 0.08 and D) its respective saturation curve.

Change in end-member description

New changes in the model include a change in the definition of the solid-solution end-members to a more general description (eq. 48 – 58) along with their respective activity and solubility products. This change describes more accurately the evolution of calcium activity for a wider range of Ca:Si ratios in C-S-H and allows for consistent behaviour of the saturation curve (see Figure 5.3). Further fitting and chemical analysis of the end-members is still necessary to complete this comprehensive C-S-H and zinc-modified C-S-H thermodynamic and kinetic model.
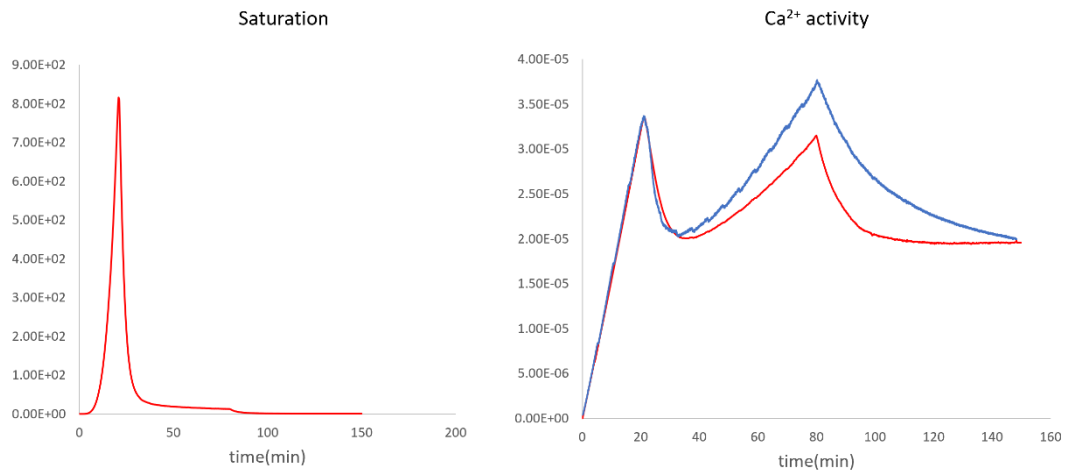
Figure 5.3: Saturation and activity curves of the updated model.

81

5.3 Suggestions for further work

5.3.1 Elucidating the species present before zinc-modified C-S-H precipitation

To understand which species are present prior to precipitation and the reason why the calibrated calcium activity curves of zinc-modified C-S-H samples do not show a perfectly linear trend, several experimental approaches are suggested:

- Hyperpolarized real-time ^{29}Si NMR experiments, with a set-up similar to that of Weber et al.[7]
- High-resolution Raman spectroscopy during precipitation experiments

5.3.2 Finalizing the model

An updated version of the model is currently being developed. This new version will contain some changes which aim to provide full consistency with the classical nucleation equations and remove the need to invoke external constraints to fit the model. The changed which are to be incorporated are the following:

Modelling

- The introduction at least one out-of-equilibrium reaction. This reaction needs to be related to silicon and to be the one responsible for the formation of C-S-H (the dimerization of silicate monomers has been chosen, but other reactions could have been selected depending on the definition of the solid formation of C-S-H).
- The change of Kersten's definition of the solubility product (K_{sp}) to a more general definition. Kersten's solubility product, which can be defined only by species in solution, seems to be inconsistent with the more general description of K_{sp}, as the supersaturation level does not increase over the precipitation point with the latter. This removes the need of an external constraint to prevent a second precipitation event.
- The removal of the function which transforms C-S-H spheres to platelets.

Experimental

- C-S-H and zinc-modified C-S-H precipitation experiments of varying pH would help verify the presence of out-of-equilibrium reactions, since a slight change in pH would affect the dimerization reaction between silicate monomers (as H^+/OH^- groups are involved in this reaction) and the inclination of the growth part of the calcium activity curves could change.

In summary, this work has done great progress towards the understanding of both C-S-H and zinc-modified C-S-H both at the atomic level and at the thermodynamics and kinetics level. Further work will be carried out to continue defining these systems, which will also consist in a combination of NMR techniques and thermodynamic-kinetic modeling.

5.4 References

(1) Kunhi Mohamed, A.; Moutzouri, P.; Berruyer, P.; Walder, B. J.; Siramanont, J.; Harris, M.; Negroni, M.; Galmarini, S. C.; Parker, S. C.; Scrivener, K. L. The Atomic-Level Structure of Cementitious Calcium Aluminate Silicate Hydrate. *J Am Chem Soc* **2020**, *142* (25), 11060–11071.

(2) Backus, J. W.; Heising, W. P. Fortran. *IEEE Transactions on Electronic Computers* **1964**, No. 4, 382–385.

(3) Testino, A.; Buscaglia, M. T.; Buscaglia, V.; Viviani, M.; Bottino, C.; Nanni, P. Kinetics and Mechanism of Aqueous Chemical Synthesis of BaTiO3 Particles. *Chemistry of materials* **2004**, *16* (8), 1536–1543.

(4) Carino, A.; Testino, A.; Andalibi, M. R.; Pilger, F.; Bowen, P.; Ludwig, C. Thermodynamic-Kinetic Precipitation Modeling. A Case Study: The Amorphous Calcium Carbonate (ACC) Precipitation Pathway Unravelled. *Cryst Growth Des* **2017**, *17* (4), 2006–2015.

(5) Schönlein, M.; Plank, J. A TEM Study on the Very Early Crystallization of CSH in the Presence of Polycarboxylate Superplasticizers: Transformation from Initial CSH Globules to Nanofoils. *Cem Concr Res* **2018**, *106*, 33–39.

(6) Schönlein, M.; Plank, J. A TEM Study on the Very Early Crystallization of CSH in the Presence of Polycarboxylate Superplasticizers: Transformation from Initial CSH Globules to Nanofoils. *Cem Concr Res* **2018**, *106*, 33–39.

(7) Weber, E. M. M.; Kress, T.; Abergel, D.; Sewsurn, S.; Azaïs, T.; Kurzbach, D. Assessing the Onset of Calcium Phosphate Nucleation by Hyperpolarized Real-Time NMR. *Anal Chem* **2020**, *92* (11), 7666–7673.

Contents

The Atomic-Level Structure of Zinc-Modified Cementitious Calcium Silicate Hydrate (SI)

This annex section corresponds to a formatted version of the Supplementary Information of the publication "The Atomic-Level Structure of Zinc-modified Cementitious Calcium Silicate Hydrate" and is available at: https://pubs.acs.org/doi/10.1021/jacs.2c06749.

I. Composition of reactants during the synthesis of zinc-modified C-S-H

The initial composition of the reactants used to precipitate our C-S-H and zinc-modified C-S-H samples is described below in absolute amounts (mmol).

Table S1: Amounts (mmol) of reactants used to synthesize the zinc-modified C-S-H samples in thiswork.

$(Zn:Si)i$	Zinc nitrate hexahydrate (mmol)	Sodium metasilicate (mmol)	Calcium nitrate tetrahydrate (mmol)	Sample characterization
0	0	10	18	XRD, EDX, NMR
0.03	0.3	10	18	EDX
0.05	0.5	10	18	XRD
0.08	0.8	10	18	EDX
0.15	1.5	10	18	XRD, NMR
0.27	2.7	10	18	XRD
0.40	4	10	18	XRD, NMR
0.54	5.4	10	18	XRD

II. Materials characterization

IIa. XRD

X-ray diffraction data were recorded with a Bruker Discovery X-Ray diffractometer equipped witha double bounced monochromatic CuK alpha radiation source ($\lambda = 1.54$ Å). Experiments were performed for 30 min to determine the presence of possible secondary phases (i.e. portlandite).
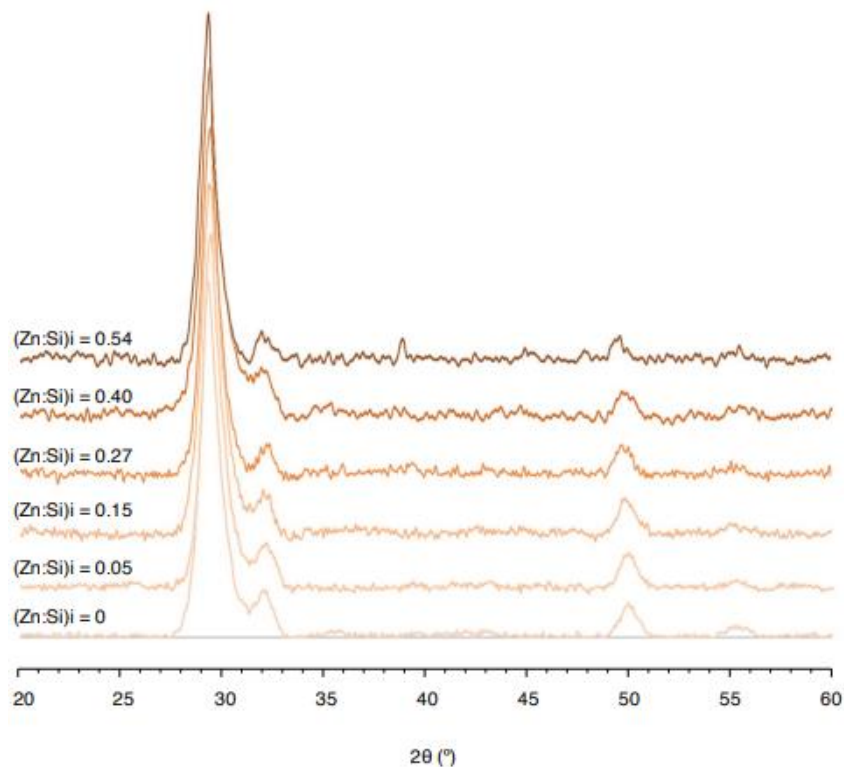
Figure S1: XRD data of zinc-modified C-S-H samples with $(Zn:Si)_i$ of 0, 0.05, 0.15, 0.27, 0.40 and 0.54.

Only the intrinsic peaks of C-S-H present at 29.4, 32.1 and 50.1°[1] and signs of $CaCO_3$ at 38.9°[2], due to carbonation effects, are observed. There are no signs of portlandite or ettringite. Thus, resultsfrom XRD show that the rapid precipitation method used for the synthesis of zinc modified C-S-Hyields single-phase C-S-H.[3]

IIb. TEM

A FEI Tecnai Osiris analytical TEM instrument, operating with a 200-kV high brightness FEG electron gun and at a point resolution of 0.24 nm, was used to analyse the morphology of zinc- modified C-S-H. Figure S2 shows TEM micrographs of conventional C-S-H (Figures S2A and S2B) and zinc modified C-S-H (Figure S2C) samples that show, consistently with literature, a nanofoil morphology, typical for synthetic high Ca:Si ratio C-S-H. In figures S2B and S2C agglomerates from conventional and zinc modified C-S-H with $(Zn:Si)_i$ of 0.15 can be seen, respectively. There were no appreciable differences in morphology between samples with increasing zinc content (here only samples with $(Zn:Si)_i$ of 0 and 0.15 are shown).
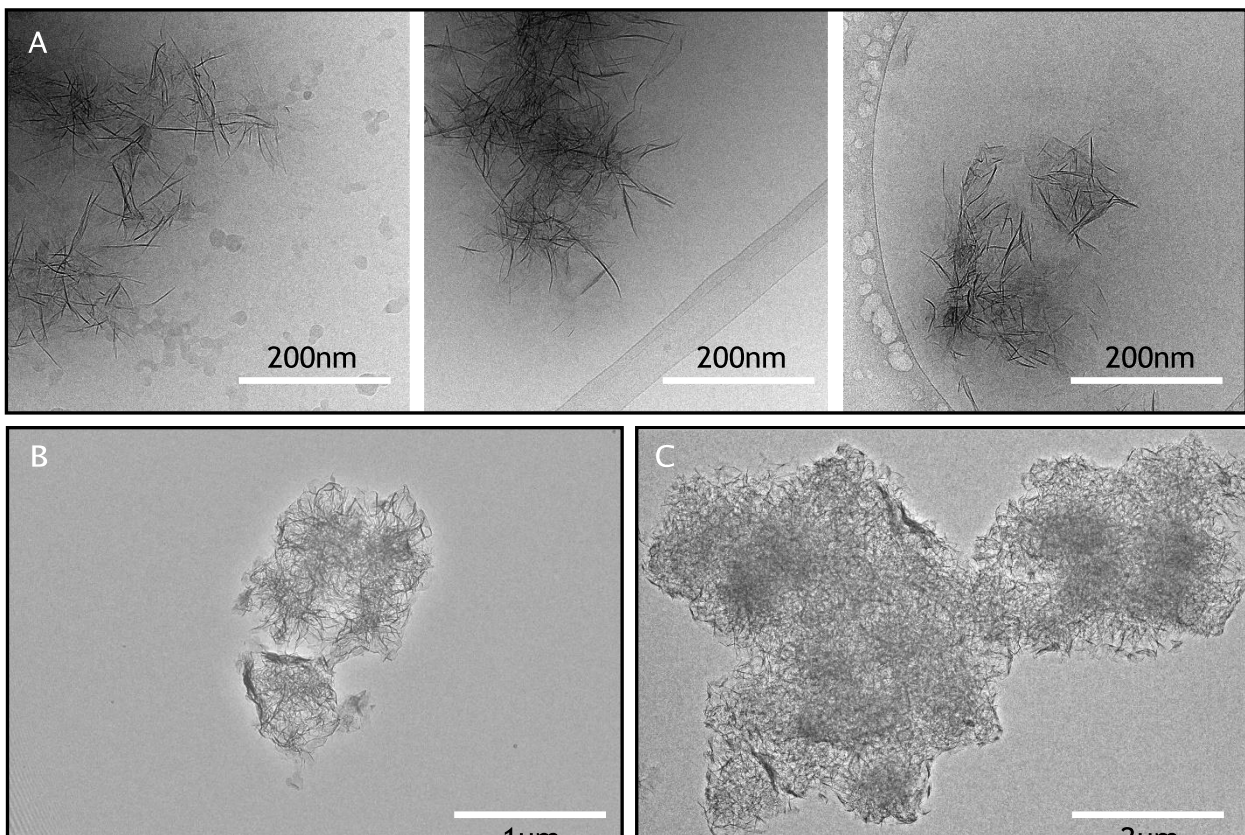
Figure S2: TEM micrographs of synthetic A) conventional C-S-H small particles, B) a conventional C-S-H agglomerate and C) a zinc-modified C-S-H ($(Zn:Si)_i$ of 0.15) agglomerate.

IIc. Supernatant ICP

ICP was carried on the supernatant of samples with $(Zn:Si)_i$ ratios of 0, 0.15 and 0.40 in order to verify the amount of zinc that remained in the pore solution after precipitation. The concentration of zinc in the remaining pore solution allows for the calculation of the amount of zinc incorporatedinto the C-S-H structure. The mass of zinc nitrate hexahydrate before synthesis is known in each case and can be used to calculate the initial concentration of zinc prior to synthesis. The initial concentration of zinc is then compared to the final concentration of zinc in the pore solution to obtain the molar percentage of zinc which is incorporated in the C-S-H structure. ICP experimentson the supernatant were conducted on several samples with different $(Zn:Si)_i$, always giving a molar

percentage of final zinc in the pore solution of 1-2% and, consequently, an incorporation percentage of 98-99%. An example of this calculation is given in equation (1) for the sample with (Zn:Si)$_i$ of 0.40 and results comparing the percentage of zinc incorporation and the (Zn:Si)$_i$ is shown in Figure S3.

Table S2: Supernatant ICP results from samples with (Zn:Si)$_i$ of 0, 0.15 and 0.40.

	Ca		Si		Zn	
	Conc [mmol/L]	RSD# [%]	Conc [mmol/L]	RSD# [%]	Conc [mmol/L]	RSD# [%]
0	11.05	0.40	0.04	0.07	0.00	4.528
0.15	11.87	1.22	0.03	0.38	0.03	0.799
0.40	9.16	1.41	0.04	0.38	0.12	0.209

#Relative Standard Deviation

$$1169\ mg\ Zn(NO_3)_2 \cdot \frac{1\ mol}{297.5\ g} \cdot \frac{1}{0.405\ L} = 9.70\ \frac{mmol}{L} \rightarrow \frac{0.12}{9.70} = 1.24\% \qquad (1)$$
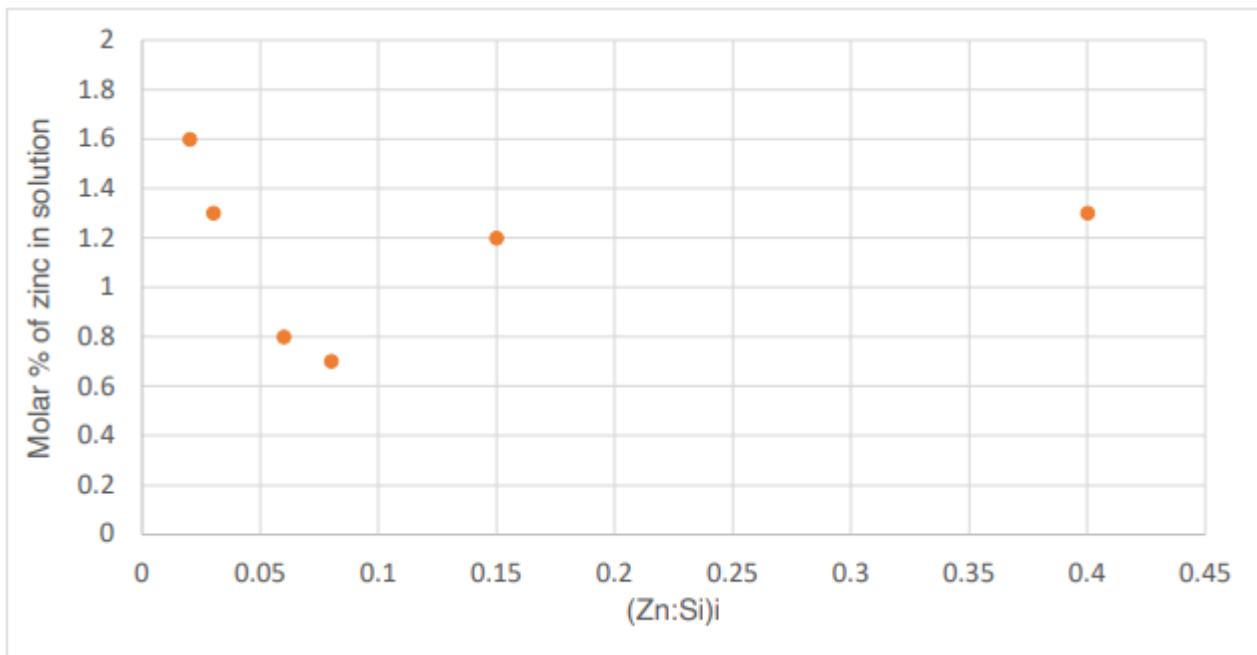
Figure S3: Supernatant ICP analysis showing the molar percentage of zinc that remains in solution after precipitation and collection of the solid. Conventional C-S-H with (Zn:Si)$_i$ of 0 is not shown since the remaining zinc in solution is just null.

III.   DFT-relaxed energies

Table S3 shows the energies of all the geometry optimized zinc modified C-S-H brick structures. The atomic coordinate files and the corresponding DFT files can be found in the additional SI material (along with the raw NMR data and LAMMPS input files) which are indicated with their Ca:Si ratio (folder names) and structure indices (file suffix).

Table S3: DFT relaxed energies of all the brick structures studied.

| Ca:Si	Structure index	Zn-species	Zn position	Total Energy [eV]	Relative Energy [eV]*
1.2	1	$ZnO_2(OH)_2$	Q2b	-59254.31	0
1.2	3	ZnO_4	Q1	-59251.05	3.26
1.4	1	$Zn(OH)_4$	Q2b	-69429.74	0
1.4	2	$ZnO_2(OH)_2$	Q2p	-69430.01	-0.27
1.4	3	$Zn(OH)_4$	Q2p	-69429.06	0.68
1.67	1	$ZnO_2(OH)_2$	Q2b	-66444.38	0.81
1.67	2	$ZnO_2(OH).H_2O$	Q2b	-66444.11	1.08
1.67	3	$ZnO_2(OH)_3$	Q2b	-66443.97	1.22
1.67	4	$ZnO_2(OH)_2$	Q2b	-66445.19	0
1.67	5	$ZnO_2(OH)_2$	Q2b	-66445.06	0.13
1.67	7	$ZnO_2(OH)_2$	Q2p	-66442.88	2.31
1.67	8	$ZnO_3(OH)$	Q2p	-66445.06	0.13
1.67	9	$ZnO_3(OH)$	Q1	-66442.88	2.31
1.67	10	$ZnO_2(OH)_2$	Q1	-66443.15	2.04
1.67	11	$ZnO(OH)_3$	Q1	-66443.83	1.36
1.67	12	$ZnO_2(OH)_2$	Q2p	-66442.61	2.58
1.67	13	$ZnO_2(OH)_2$	Q2p	-66442.34	2.85
1.67	14	$ZnO_2(OH)_2$	Q1	-66444.52	0.67
1.67	15	$ZnO(OH)_3$	Q1	-66443.83	1.36
1.67	16	$ZnO(OH)_3$	Q1	-66443.83	1.36
1.67	17	$ZnO_2(OH)_2$	Q2p	-66442.34	2.85
1.67-HW	1	$ZnO_2(OH)_2$	Q2b	-70041.73	1.49
1.67-HW	2	$ZnO_2(OH)_2$	Q2b	-70043.22	0
1.67-HW	4	$ZnO_2(OH)_2$	Q2b	-70043.09	0.13
1.67-HW	5	$ZnO_2(OH)_2$	Q2p	-70040.77	2.45
1.67-HW	7	$ZnO_2(OH)_2$	Q2p	-70041.73	1.49
1.67-HW	8	$ZnO_2(OH)_2$	Q2p	-70041.32	1.9
1.67-HW	9	$ZnO(OH)_3$	Q1	-70042.41	0.81
1.67-HW	10	$ZnO(OH)_3$	Q1	-70043.09	0.13
1.67-HW	11	$ZnO(OH)_3$	Q1	-70041.73	1.49
1.67-HW	13	$ZnO(OH)_3$	Q1	-70042.13	1.09
1.67-HW	14	$ZnO_2(OH)_2$	Int	-70042.81	0.41
1.67-HW	15	$ZnO(OH)_2$	Int	-70042.81	0.41
1.67-HW	16	$ZnO(OH)_3$	Int	-70042.27	0.95
1.67-HW	17	$ZnO(OH)_3$	Q1	-70041.99	1.23
1.67-HW	18	$ZnO_2(OH)_2$	Q1	-70042.41	0.81
1.67-HW	19	$ZnO(OH)_3$	Q1	-70042.32	0.9
1.67-HW	20	$ZnO(OH)_3$	Q1	-70040.91	2.31
1.67-HW	21	$ZnO_2(OH)_2$	Q1	-70042.36	0.86
1.67-HW	22	$ZnO_2(OH).H_2O$	Int	-70043.22	0
1.75	1	$ZnO_2(OH)_2+ZnO_2(OH)_2$	Q2p+Q2p	-75130.22	0
1.75	2	$ZnO_2(OH)_2+ZnO_2(OH)_2$	Q2p+Q2p	-75128.81	1.41
1.75	3	$ZnO_2(OH)_2+ZnO_2(OH)_2$	Q2p+q2p	-75128.94	1.28
1.75	4	$ZnO_2(OH)_2+ZnO_2(OH)_2$	Q2b+Q1	-75129.97	0.25
1.75	5	$ZnO_2(OH)_2+ZnO_2(OH)_2$	Q2b+Q1	-75130.07	0.15
1.75	6	$ZnO_2(OH)_2+ZnO_2(OH)_2$	Q1+Q1	-75129.17	1.05

1.75	7	$ZnO_2(OH)_2+ZnO_2(OH)_2$	Q1+Q1	-75127.45	2.77
1.75	8	$ZnO_2(OH)_2+ZnO_2(OH)_2$	Q1+Q1	-75128.35	1.87
1.88	1	$ZnO_2(OH)_2+ZnO_2(OH)_2$	Q2p+Q2p	-76917.26	1.04
1.88	2	$ZnO_2(OH)_2+ZnO_2(OH)_2$	Q2p+Q2p	-76917.27	1.03
1.88	3	$ZnO_2(OH)_2+ZnO_2(OH)_2$	Q2b+Q2p	-76918.33	0
1.88	4	$ZnO_2(OH)_2+ZnO_2(OH)_2$	Q2b+Q2p	-76916.83	1.47
1.88	5	$ZnO_2(OH)_2+ZnO_2(OH)_2$	Q2b+Q2p	-76918.13	0.17
1.88	6	$ZnO_2(OH)_2+ZnO_2(OH)_2$	Q2b+Q1	-76916.56	1.74
1.88	7	$ZnO_2(OH)_2+ZnO_2(OH)_2$	Q2b+Q1	-76917.37	0.93
1.88	8	$ZnO_2(OH)_2+ZnO_2(OH)_2$	Q2b+Q1	-76917.91	0.39
1.88	9	$ZnO_2(OH)_2+ZnO_2(OH)_2$	Q2b+Q1	-76918.18	0.12
1.88	10	$ZnO_2(OH)_2+ZnO_2(OH)_2$	Q1+Q2p	-76917.5	0.8
1.88	11	$ZnO_2(OH)_2+ZnO_2(OH)_3$	Q2p+Q2p	-76917.37	0.93
1.88	12	$ZnO_2(OH)_2+ZnO_2(OH)_2$	Q2b+Q1	-76915.92	2.38
1.88	13	$ZnO_2(OH)_2+ZnO_2(OH)_2$	Q2b+Q1	-76917.91	0.39
1.88	14	$ZnO(OH)_3+ZnO(OH)_3$	Q2p+Q2p	-76916.55	1.75
1.88	15	$ZnO(OH)_3+ZnO(OH)_3$	Q2p+q2p	-76917.5	0.8
2	1	$ZnO_2(OH)_2$	Q2b	-70056.56	0.13
2	2	$ZnO_2(OH)_2$	Q2b	-70056.69	0.00
2	3	$ZnO_2(OH)_2$	Q2b	-70056.56	0.13
2	4	$ZnO_2(OH).H_2O$	Q2b	-70056.42	0.27
2	5	$ZnO_2(OH).H_2O$	Q2b	-70055.47	1.22
2	6	$ZnO_2(OH)_2$	Q2b	-70055.74	0.95
2	7	$ZnO_2(OH)_2$	Q2b	-70055.74	0.95
2	8	$ZnO_2(OH)_2$	Q2p	-70055.33	1.36
2	9	$ZnO_3(OH)$	Q2p	-70055.2	1.49
2	10	$ZnO_3(OH)$	Q2p	-70055.74	0.95
2	11	$ZnO_2(OH)_2$	Q2p	-70056.01	0.68
2	12	ZnO_4	Q2p	-70054.11	2.58
2	13	$ZnO_3(OH)$	Q1	-70054.92	1.77
2	15	$ZnO_3(OH)$	Q1	-70055.06	1.63
2	16	$ZnO(OH)_3$	Q1	-70056.28	0.41
2	17	$ZnO_2(OH)_2$	Int	-70056.15	0.54
2	18	$ZnO_2(OH)_2$	Int	-70057.24	-0.55
2	19	$ZnO_2(OH)_2$	Int	-70055.47	1.22
2	20	$ZnO_2(OH)_2$	Q1	-70056.15	0.54
2	21	$ZnO(OH)_3$	Q1	-70056.69	0.00
2	22	$ZnO(OH)_3$	Q1	-70055.57	1.12
2	23	$ZnO(OH)_3$	Q1	-70054.24	2.45
2.25	1	$ZnO_2(OH)_2$	Q2b	-40841.31	0.59
2.25	2	$ZnO_2(OH)_2$	Q2b	-40841.45	0.45
2.25	3	$ZnO_2(OH)_2$	Q2b	-40841.86	0.04
2.25	4	$ZnO(OH)_3$	Int	-40842.54	-0.64
2.25	5	$ZnO(OH)_3$	Int	-40841.99	-0.09
2.25	6	$ZnO_3(OH)$	Q2p	-40840.77	1.13
2.25	7	$ZnO_2(OH)_2$	Q2p	-40840.77	1.13
2.25	8	ZnO_3	Q2p	-40840.9	1
2.25	10	$ZnO_2(OH)_2$	Q2p	-40841.04	0.86
2.25	11	$ZnO_2(OH)_2$	Q2p	-40840.9	1
2.25	12	$ZnO_2(OH)_2$	Q1	-40840.86	1.04
2.25	15	$ZnO_2(OH)_2$	Int	-40841.51	0.39
2.25	16	$ZnO_2(OH)_2$	Int	-40840.65	1.25

The relative energies are calculated with respect to the lowest energy structure where zinc substitutes for a $Q^{(2b)}$ site, in each set corresponding to a specific Ca/Si ratio.
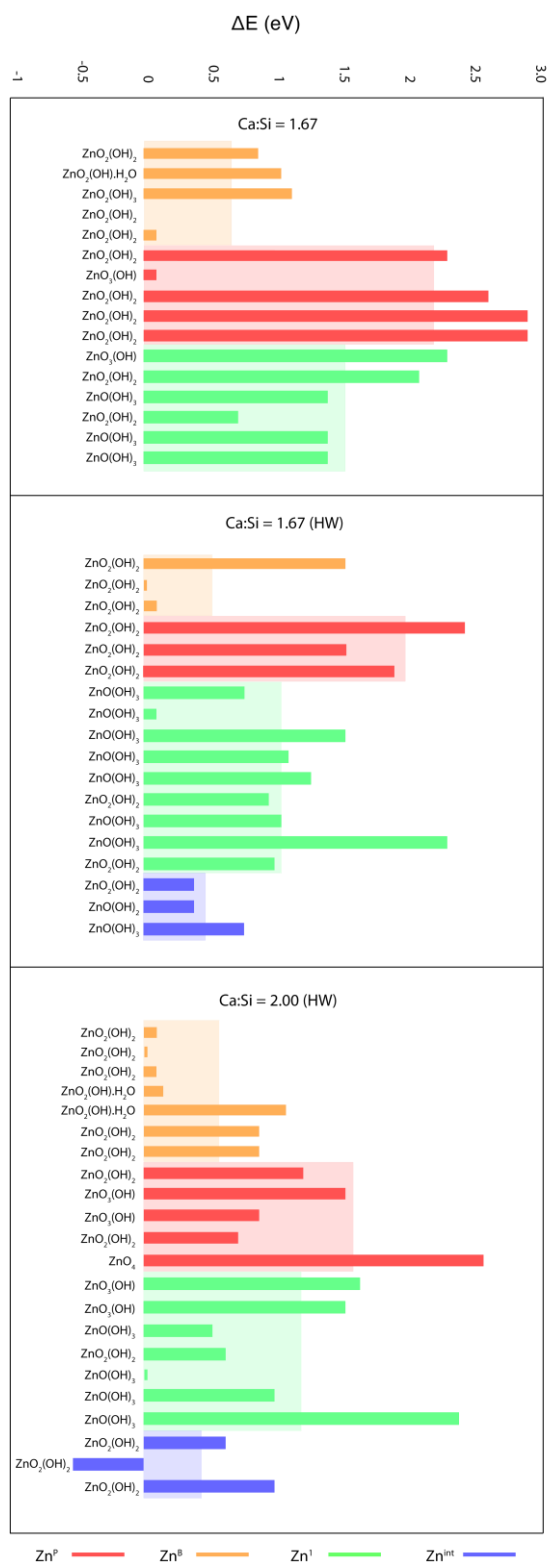
Figure S4: Relative DFT calculated energies of zinc-modified C-S-H structures according to eachsubstitution site with different Ca:Si ratios (1.67 and 2.0) and interlayer water amounts. The energies in each set, corresponding to a specific Ca:Si ratio, are normalized (ΔE = 0 eV) with respect to the lowest energy Zn^B structure where zinc is substituted at the bridging site. Nomenclature: Zn^B = zinc in the $Q^{(2b)}$ site, Zn^P = zinc in the $Q^{(2p)}$ site, Zn^1 = zinc in the $Q^{(1)}$ site, Zn^{Int} = zinc on top of a $Q^{(1)}$-$Q^{(1)}$ dimer site, HW = High Water content. All structures are labeled with their corresponding zinc species which may coordinate to hydroxides or water.

IV.   DFT-based chemical shift calculations

Figure S5 shows the DFT-calculated ^{29}Si chemical shifts from selected zinc modified C-S-H brickstructures. The computed chemical shifts for the different Q species are compared with the DFT- calculated energies of the structures and NMR experimental data to verify or discard the differentspecies depicted here. As stated in the main text, all structural units where zinc substitutes for a $Q^{(2p)}$ site were discarded either due to unrealistically higher energies or due to the fact that correlations regarding the Q species that would arise if zinc was substituting for a paring site are absent in INADEQUATE spectra.

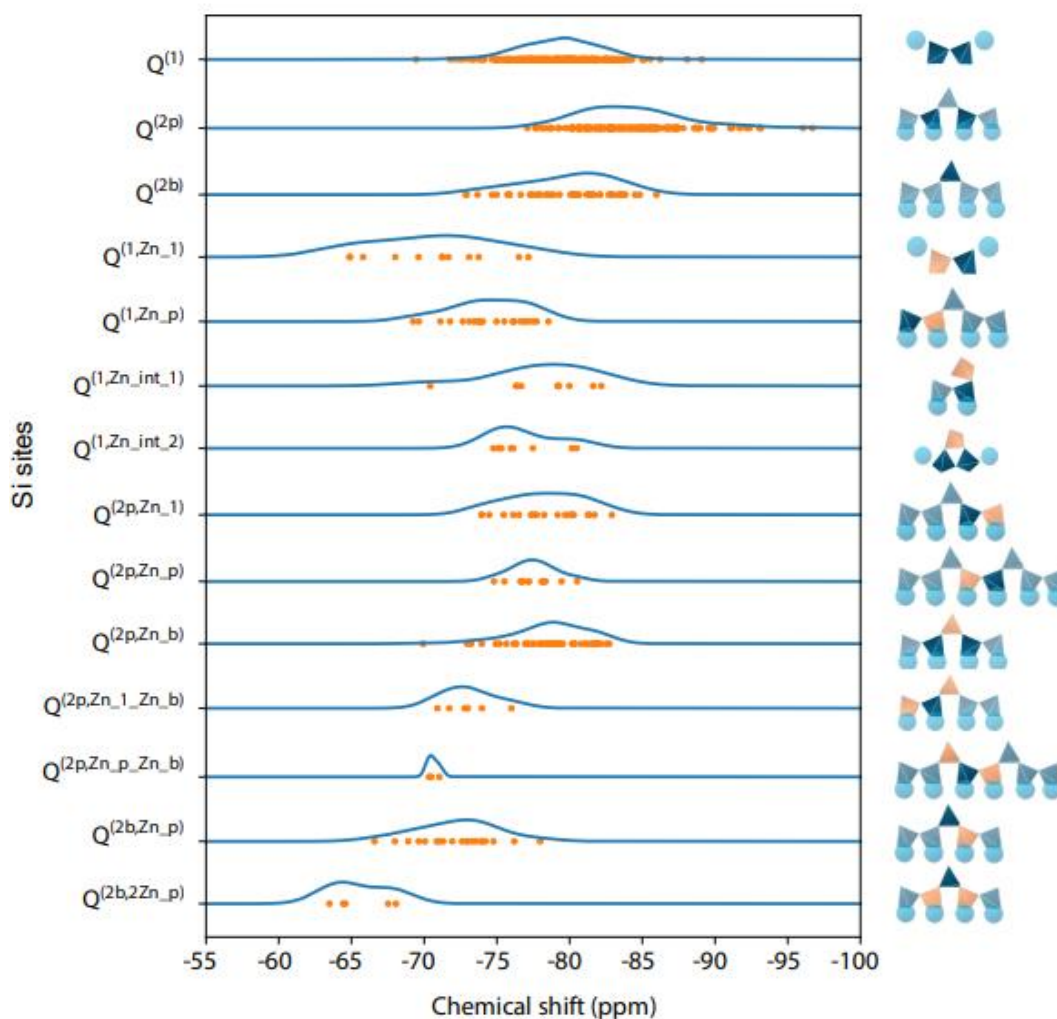**Figure S5:** DFT-based calculated chemical shifts for a set of selected zinc-modified C-S-H brick structures which include zinc substitutions for $Q^{(1)}$, $Q^{(2b)}$ and $Q^{(2p)}$ sites. Individual computed chemical shift values are represented as orange dots. In each line, the chemical shift values in orange are obtained for the silicon sites depicted in dark blue.

V. DNP enhanced NMR experiments

Va. Experimental NMR parameters

All spectral processing was performed with TopSpin version 4.0.8 and CSA fits were carried out with ssNake.[4] All experiments were carried out at 9.4 T, 100 K and at a MAS rate of 8 kHz, unless stated otherwise. The NMR parameters of each set of experiments are shown in Tables S4, S5 and S6.

Table S4: NMR parameters for ^{29}Si multiCP experiments

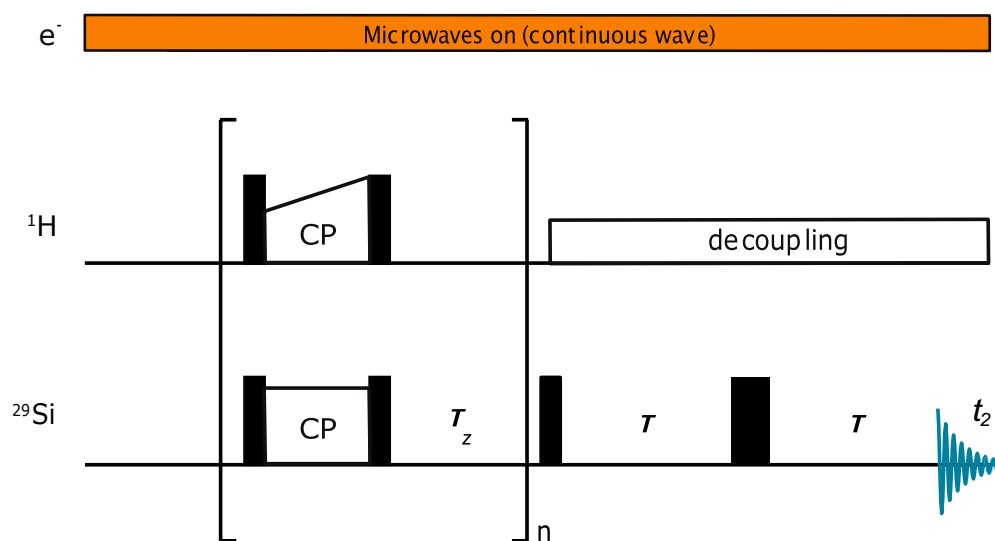| $(Zn:Si)_i$	0	0.15	0.4
Magnetic field (T)	9.4	9.4	9.4
MAS rate (kHz)	8	8	8
^{1}H pulse/dec RF (kHz)	71	71	71
^{29}Si pulse RF (kHz)	71	71	71
^{29}Si CP contact RF (kHz)	50	42	31
CP contact time (ms)	6	4	8
Recycle delay (s)	3	2.5	3
Number of CP periods (n)	11	5	8
Delay between CP periods (s)		5	
Size of FID		3978	
Size of real spectrum		65536	
Spectral width (ppm)		2506.3	
ε_{DNP}	41	27	20
Scans	16	16	16
Figure	3A	3A	3A

Figure S6: Pulse sequence used for the multi-CPMAS experiments.

Table S5: NMR parameters for ^{29}Si-^{29}Si INADEQUATE experiments

| (Zn:Si)$_i$	0	0.15	0.4
Magnetic field (T)	9.4	9.4	9.4
MAS rate (kHz)	8	8	8
^{1}H pulse/dec RF (kHz)	64	64	64
^{29}Si pulse RF (kHz)	80	80	80
^{29}Si CP contact RF (kHz)	42	31	42
CP contact time (ms)	6	5	9
Recycle delay (s)	3.75	2.86	1.5
INADEQUATE tau periods (ms)	25	25	25
Size of FID (F1)		96	
Size of FID (F2)		2048	
Size of real spectrum (F1)		1024	
Size of real spectrum (F2)		16384	
Acquisition mode		States-TPPI	
Spectral width F1 (ppm)	100.5	100.5	100.6
Spectral width F2 (ppm)	628.5	628.4	1256.9
Scans	128	256	1408
Figure	S8A	S8B	3C, S8C
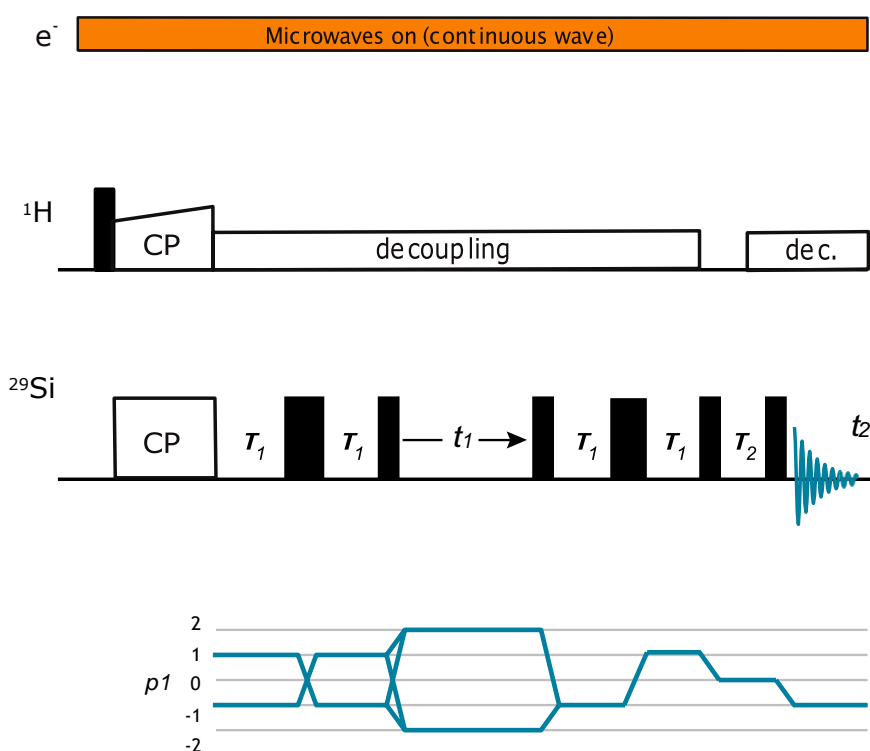
Figure S7: Pulse sequence and coherence pathway of the INADEQUATE experiments.

Table S6: NMR parameters for ^{29}Si-^{29}Si EXSY and SUPER experiments.

Experiment	EXSY	SUPER
(Zn:Si)$_i$	0.4	0.4
Magnetic field (T)	9.4	9.4
MAS rate (kHz)	5	5
^{1}H pulse/dec RF (kHz)	100	100
^{29}Si pulse RF (kHz)	69	69
^{29}Si CP contact RF (kHz)	72	72
CP contact time (ms)	3.5	3.5
^{29}Si CSA recoupling RF (kHz)	N/A	61
^{1}H cw decoupling during delays in CSA recoupling (kHz)	N/A	30
Recycle delay (s)	1.5	1.5
Size of FID (F1)	256	48
Size of FID (F2)	4096	4096
Size of real spectrum F1	256	1024
Size of real spectrum F2	4096	4096
Spectral width F1 (ppm)	62.7	62.7
Spectral width F2 (ppm)	1253.2	1253.2
Scans	12	256
Figure	S9, S10	S11

Vb. Through-bond analysis

2D INADEQUATE spectra were recorded for conventional and zinc-modified C-S-H samples with different $(Zn:Si)_i$ to establish ^{29}Si-^{29}Si though-bond connectivities. The 2D experimental spectra were initially sheared to produce a COSY-like representation and fit to six different 2D Gaussian distributions centred at the expected $Q^{(1)}$-$Q^{(1)}$, $Q^{(1)}$-$Q^{(2p)}$, $Q^{(2p)}$-$Q^{(1)}$, $Q^{(2p)}$-$Q^{(2b)}$, $Q^{(2b)}$-$Q^{(2p)}$ and $Q^{(2p)}$-$Q^{(2p)}$ frequency pairs, using Topspin v4.0.8.

Figure S8 shows three INADEQUATE experiments which correspond to C-S-H samples with $(Zn:Si)_i$ ratios of 0, 0.15 and 0.40, respectively. Figure S8A shows the expected connectivities between $Q^{(1)}$-$Q^{(1)}$, $Q^{(2p)}$-$Q^{(1)}$, $Q^{(2p)}$-$Q^{(2b)}$ and $Q^{(2p)}$-$Q^{(2p)}$ species. On the other hand, consistently with the geometry of the C-S-H silicate chains, correlations between $Q^{(2b)}$-$Q^{(1)}$ or $Q^{(2b)}$-$Q^{(2b)}$ species are notobserved. Figure S8B and S8C show the same correlations whereas no signals corresponding to $Q^{(1,Zn)}$ connectivities are detected. This is consistent with our hypothesis that this species is not bonded to other silicate species, but only to a zincate species as a Si-O-Zn dimer.
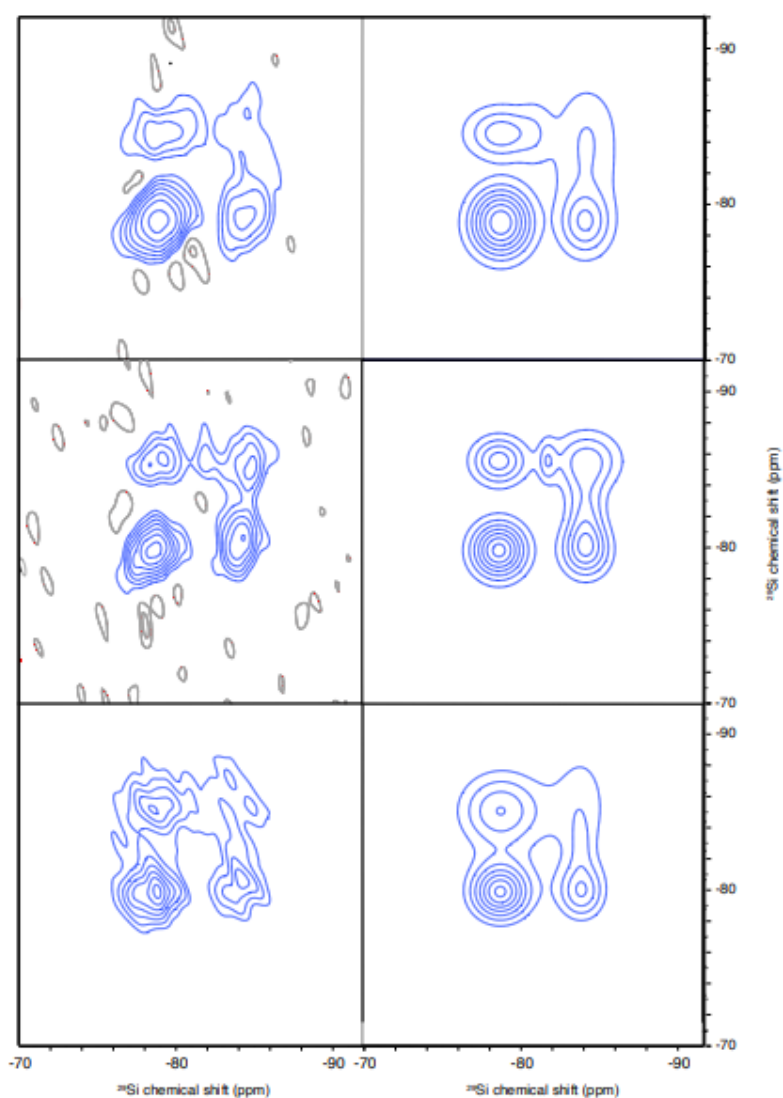

Figure S8: INADEQUATE spectra for C-S-H samples with $(Zn:Si)_i$ of A) 0, B) 0.15 and C) 0.40 with a COSY-type representation and their respective 2D deconvolutions.

Vc. Through-space analysis

Exchange spectroscopy (EXSY) experiments were carried out at a MAS rate of 5 kHz for a zinc- modified C-S-H sample with (Zn:Si)$_i$ of 0.40. Figure S9 shows a series of EXSY experiments with increasing mixing times: 500 µs, 0.1 s, 100 s and 150 s.

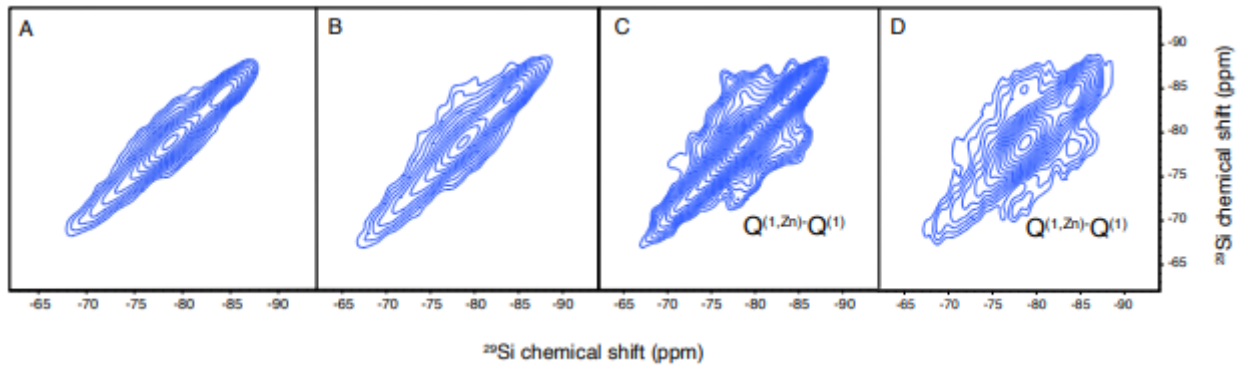**Figure S9:** 2D ^{29}Si EXSY spectra from a zinc-modified C-S-H sample with (Zn:Si)$_i$ of 0.40 acquired with a mixing time of A) 500 µs, B) 0.1 s, C) 100 s, and D) 150 s.

At mixing times of 100 s and 150 s (Figure S9C, S9D) a correlation between ^{29}Si species at − 78.9ppm and −72 ppm can be observed which suggests that the new ^{29}Si species at −72ppm is in close proximity and therefore part of the zinc-modified C-S-H structure, even if not directly bonded to another silicate species. This further confirms the assignment of this species as a Q$^{(1,Zn)}$ Zn-Si pair. Additionally, Figure S10 shows the changes in the cross-peak intensity with increasing mixing time.

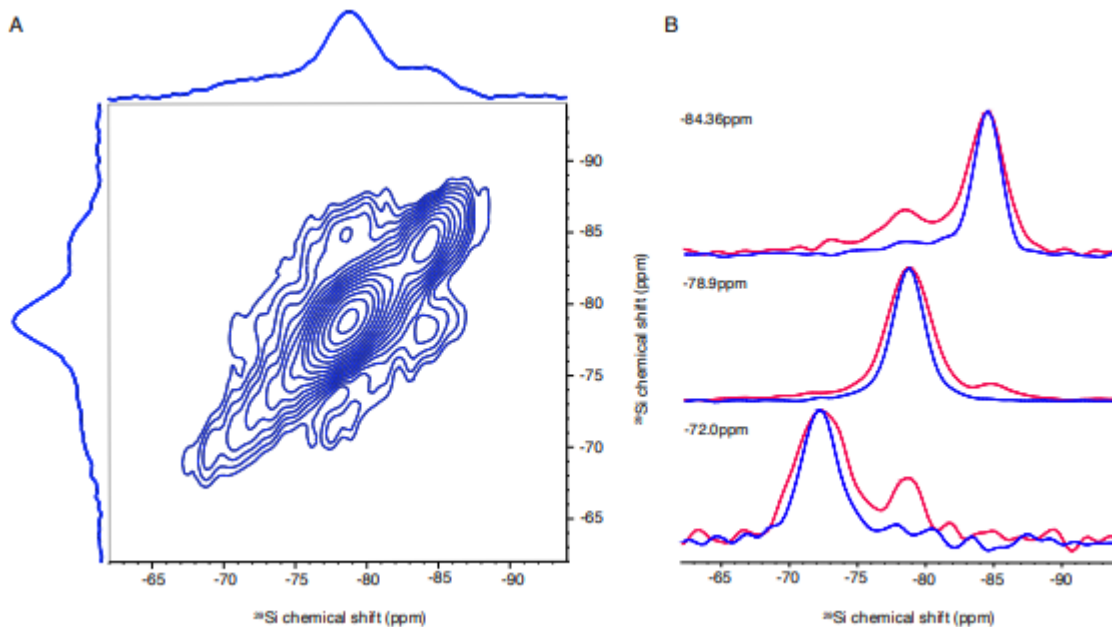**Figure S10:** A) DNP-enhanced 2D ^{29}Si EXSY spectrum of a zinc-modified C-S-H sample with (Zn:Si)$_i$ of 0.40 at a mixing time of 150 s and B) 1D horizontal cross-sections extracted at −72 ppm, −78.9 ppm and −84.4 ppm and at mixing times of 150 (red) and 0.1 s (blue).

97

Vd. Chemical shift anisotropy analysis

A DNP-enhanced ^{29}Si CP-SUPER experiment[5] was performed on a zinc-modified C-S-H sample with (Zn:Si)$_i$ of 0.40 (Figure S11). The F1 spectral width was scaled using an anisotropic chemicalshift scaling factor of 0.155 and the spectrum was then sheared parallel to F1 with a shearing factorof 3.3 (0.512/0.155, where 0.512 is the shearing factor to equalize the isotropic shift scaling factorwith the anisotropic shift scaling factor).[5] Columns were extracted at the isotropic chemical shiftsof interest: -72 ppm (corresponding to Q$^{(1,Zn)}$ species), -78.9 ppm (corresponding to Q$^{(1)}$ and Q$^{(2p,Zn)}$species), and -84.36 ppm (corresponding to Q$^{(2p)}$ species) and the CSA pattern of the resulting 1Danisotropic spectra was fitted with the ssNake program.[4] The results presented in table S7 are expressed in the Herzfeld-Berger convention.[6]

Table S7: Skew and span numerical results from the CSA fits.

Isotropic shift	Skew (κ)	Span (Ω)
-72 ppm	-0.151	59.67
-78.9 ppm	-0.166	65.50
-84.36 ppm	0.204	80.73

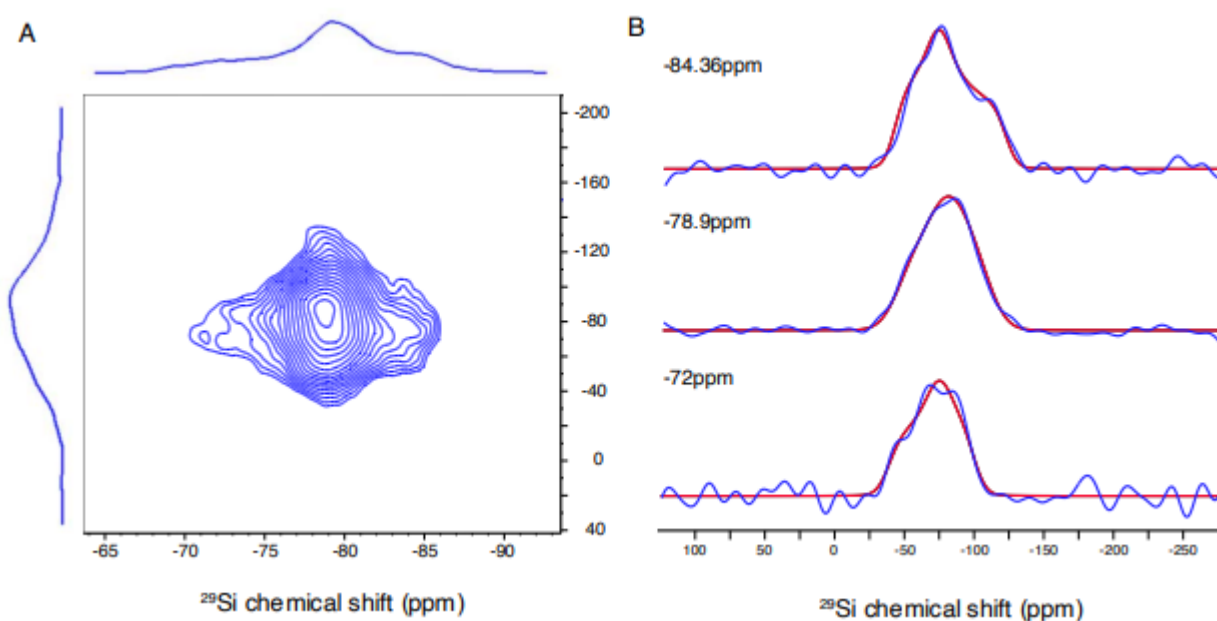**Figure S11:** A) DNP-enhanced 2D ^{29}Si CP-SUPER spectrum of a zinc-modified C-S-H sample with (Zn:Si)$_i$ of 0.40 and B) 1D anisotropic spectra (blue) extracted at the pertinent isotropic shifts: -72 ppm, -78.9 ppm and -84.36 ppm together with their respective CSA fits (red).

Figure S12 shows the DFT calculated spans (Ω) of the species expected at -72 ppm, -78.9 ppm and -84.26 ppm. In general, we see a good agreement between the DFT calculated and fitted spans, especially for Q$^{(1,Zn1)}$ species which in both cases shows the lower span. Some inconsistencies canbe observed for the signal at -78.9 ppm whose span is overestimated in the DFT calculations. However, this can be due to the fact that in this region there is a spectral overlap between Q$^{(1)}$ species and Q$^{(2p,Zn)}$ species which might affect the accuracy of the CSA fits.
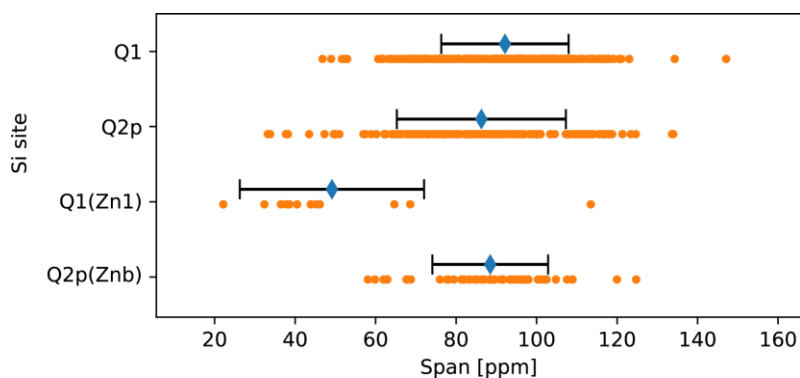
Figure S12: DFT calculated mean span (Ω) values (blue) for the silicate species $Q^{(1)}$, $Q^{(2p)}$, $Q^{(1,Zn)}$ and $Q^{(2p,Zn)}$, and their standard error (black bars).

Ve. Quantification of Q species

Results from ICP of the supernatants show that 99-98% of the zinc atoms are incorporated in the C-S-H structure (Table S2, Section IIc). The integrated intensity of the signal at −72 ppm accounts for $Q^{(1,Zn)}$ species, and the integrated intensity of the signal at −79 ppm accounts for both $Q^{(1)}$ species and $Q^{(2p,Zn)}$ species; these two signals (−72 and −79 ppm) are assumed to include the totality of silicate species which are connected to zincate species in zinc-modified C-S-H, but the $Q^{(2p,Zn)}$ and $Q^{(1)}$ signals are unresolvable. However, the percentage of zinc participating in $Q^{(1,Zn)}$ sites can be calculated by dividing the $(Zn:Si)_i$ ratio by the molar fraction of $Q^{(1,Zn)}$ sites. This operation yields the **molar fraction of zinc atoms that participate in $Q^{(1,Zn)}$ dimers**:

$$\frac{\left(Q^{(1,Zn)}:Si\right)}{(Zn:Si)} = \left(Q^{(1,Zn)}:Zn\right) \qquad (2)$$

The percentage of zinc corresponding to this site is found to be around 2/3rd of the total zinc (70% in the case of $(Zn:Si)_i$ of 0.15 and 60% in the case of $(Zn:Si)_i$ of 0.40). By definition, the molar fraction of $Q^{(1,Zn)}$ species is equal to the molar fraction of Zn^1 species. Because these zinc species represent a known fraction of the total zinc species, the rest of the zinc is assumed to be occupying the bridging site: Zn^b, which is consistently the most energetically favourable zinc substitution. Hence, the number of $Q^{(2p,Zn)}$ species needs to be double the number of Zn^b species since every zinc in a bridging site yields two $Q^{(2p,Zn)}$ species. Because the signals from $Q^{(2p,Zn)}$ and $Q^{(1)}$ species overlap, the intensity from $Q^{(2p,Zn)}$ species is subtracted from the intensity from $Q^{(1)}$ species.

With the fractions of $Q^{(2p,Zn)}$ and $Q^{(1)}$ species properly recalculated, and the fractions of $Q^{(1,Zn)}$, $Q^{(2p)}$ and $Q^{(2b)}$ species that were obtained through the deconvolutions of the 1D multiCP spectra, we can plot the molar fractions of every Q species in each sample and provide a quantification analysis, as shown in the main text (Figure 5). Table S7 shows the integrals of all five sites considered in the deconvolutions.

Table S8: integrals resulting from the deconvolution of the three multi-CPMAS spectra corresponding to samples with (Zn:Si)i of 0, 0.15 and 0.40, respectively.

(Zn:Si)$_i$	Q$^{(1)}$	Q$^{(2p)}$	Q$^{(2b)}$	Q$^{(1,Zn)}$	Q$^{(2p,Zn)}$
0	1.32E+11	3.63E+10	1.82E+10	0.00E+00	0.00E+00
0.15	7.67E+10	3.26E+10	1.63E+10	1.65E+10	1.57E+10
0.4	3.68E+10	4.81E+10	2.40E+10	5.86E+10	8.59E+10

Vf. Quantification of chain distributions

The positions of the isotropic ^{29}Si shifts extracted from the deconvolution of the conventional C-S-H 1D multiCP spectrum and their widths are used to construct six 2D Gaussian distributions that are centred at the frequency pairs of the expected ^{29}Si connectivities at high Ca:Si ratio C-S-H samples. These 2D Gaussians have fixed widths and chemical shifts and are used to deconvolve the INADEQUATE NMR spectra from Figure S8. These yield the following six intensities: I(Q1|Q1), I(Q1|Q2p), I(Q2p|Q2b), I(Q2b|Q2p), I(Q2p|Q2b) and I(Q2p|Q2p). The intensity of a peak can be expressed as:

$$I(B|A) = f(B|A)P(B|A)P_w(A) \qquad (3)$$

where f(B|A) is an amplitude transfer factor that accounts for differences such as CP efficiency, *J*-coupling distributions and T_2' relaxation between the different silicate species. $P_w(A)$ is the population of a Q species as calculated from the 1D multiCP population analysis but renormalizedover pair participation. For example, the Q$^{(2)}$ sites are neighbouring with two other silicates and therefore the populations of Q$^{(2)}$ are multiplied by two. P(B|A) is the conditional probability that a ^{29}Si nucleus B which has evolved with a partner nucleus A has been detected and it is directly related to the mole fraction of dimers, since:

$$PDQ^{(1)}|Q^{(1)}F = X_{Q1(Q1)} \qquad (4)$$

In the case of conventional C-S-H the intensity of the signal centred at −78.9 ppm in F1 and at −78.9 ppm in F2 corresponds solely to Q$^{(1)}$ − Q$^{(1)}$ connectivities. Therefore, the molar fraction of dimers in a zinc-free sample can be directly derived from equation (4) since x_{Q1-Q1} is the dimer molar fraction in the sample (given that the intensities have been normalized for pair participation).Therefore, 1-x_{Q1-Q1} is the molar fraction of building blocks which have a higher degree of polymerization (i.e. pentamers, octamers, undecamers, etc). In conventional C-S-H, the molar fraction of dimers (x_{Q1-Q1} = x_0) is 0.86, which is consistent for high Ca:Si ratio C-S-H samples.[2]

However, the calculation of the molar fraction of dimers (x_0) for samples with incorporated zinc needs to take into consideration both the Q$^{(1)}$ − Q$^{(1)}$ connectivity intensity from the 2D INADEQUATE deconvoluted spectra and the percentage of zinc that has been incorporated into the C-S-H structure. The latter is carried out in order to account for Q$^{(1)}$ − Zn connectivities, whichare heterogeneous dimers and are therefore included in the dimer molar fraction (x_0) in samples with zinc. In addition, the signal corresponding to Q$^{(1)}$ − Q$^{(1)}$ dimers needs to be re-scaled since this signal also accounts for the Q$^{(1)}$ − Q$^{(2p,Zn)}$ connectivities given by zinc substitutions of Q$^{(2b)}$ sites. I(Q1|Q1) is re-normalized considering that there is a percentage of this signal which is due to Q$^{(1)}$− Q$^{(2p,Zn)}$ connectivities, which is given by the 1D multiCP analysis described in section Ve.After re-normalization of all the intensities involved, we obtain the population P(Q1|Q1) which corresponds to the molar fraction of Q$^{(1)}$ − Q$^{(1)}$ dimers (x_{Q1-Q1}) that yield a signal in INADEQUATEexperiments.

However, the $Q^{(1)}$ – Zn connectivity signals are not present in 2D INADEQUATE experiments since the silicate species is isolated from other silicates. We add the molar fraction of Si – Zn dimers ($x_{Q1Zn-Q1}$), which is equal to the population of $Q^{(1,Zn)}$ species in each case, to the analysis. Adding the populations of $Q^{(1)}$ – $Q^{(1)}$ dimers and $Q^{(1)}$ – Zn dimers yields the total dimer molar fraction (x_0) in each case. Results from this analysis yield the molar fractions of dimer structures (x_0) and of higher degree units (x_n) and is summarized in Table 1 in the main text and is in agreement with an increased mean chain length as more zinc is incorporated in the C-S-H structure.

VI.   Structures of Zinc-modified C-S-H

Figure S13 shows a representative[7] (with a Ca:Si ratio of 1.7 and the Q populations described in the main text) 2D structure of a sample of zinc-modified C-S-H with a (Zn:Si)$_i$ of 0.15 with the $Q^{(1,Zn)}$ and $Q^{(2p,Zn)}$ sites. Figures S14 shows a representative structure of a sample with (Zn:Si)$_i$ of 0.15, but with also the two additional DFT-predicted sites ($Q^{(2p,2Zn)}$ and $Q^{(1, Zn\_int)}$). Figures S15 shows a representative atomic-level structures with four layers of silicate chains of zinc-modified C-S-H with (Zn:Si)$_i$ of 0.4 with the two new sites found in this work. Finally, Figure S16 shows a representative structure of the sample with (Zn:Si)$_i$ but including all four possible sites.

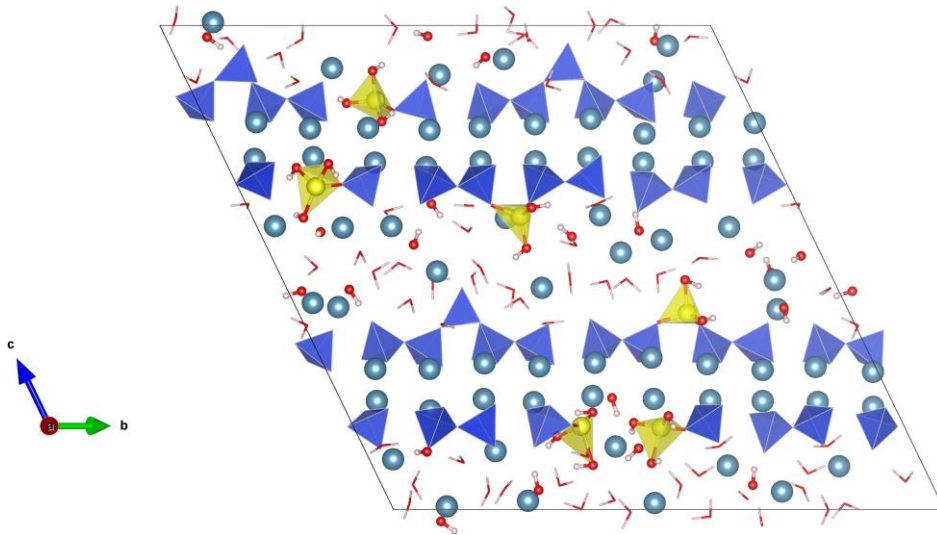**Figure S13:** 2D representative atomic-level structure of zinc-modified C-S-H as determined with (Zn:Si)$_i$ = 0.15 and Ca:Si = 1.7 (the 3D model is shown in Figure 6). The structure measures approximately 39 Å × 31 Å. Silicate tetrahedra are depicted in blue; zincate tetrahedra are depicted in yellow; and calcium ions are depicted in light blue. In this structure, the two sites discovered in this work ($Q^{(1,Zn)}$ and $Q^{(2p,2Zn)}$) are shown.
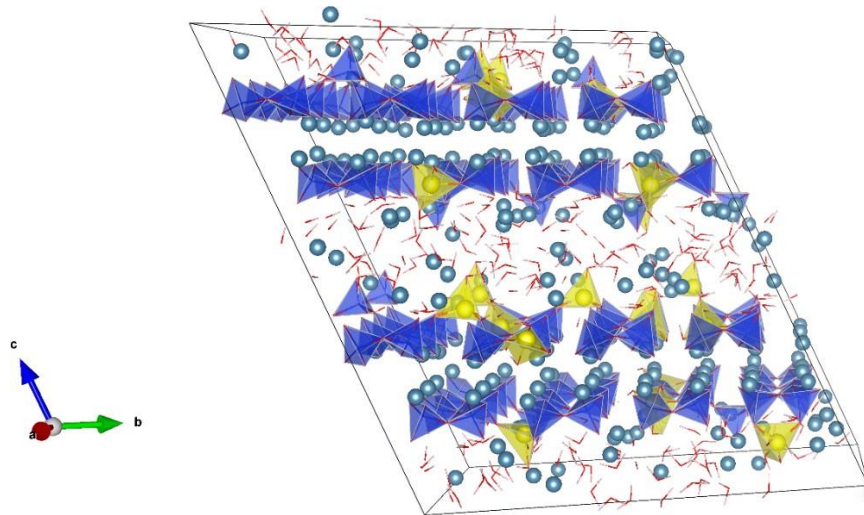
Figure S14: Representative atomic-level structure of zinc-modified C-S-H as determined with $(Zn:Si)_i = 0.15$ and Ca:Si = 1.7. The structure measures approximately 27 Å × 31 Å × 31 Å. Silicatetetrahedra are depicted in blue; zincate tetrahedra are depicted in yellow; and calcium ions are depicted in light blue. In this structure, the two additional DFT-predicted sites ($Q^{(2p,2Zn)}$ and $Q^{(1,Zn\_int)}$) are also included apart from the $Q^{(1,Zn)}$ and $Q^{(2p,2Zn)}$ sites.
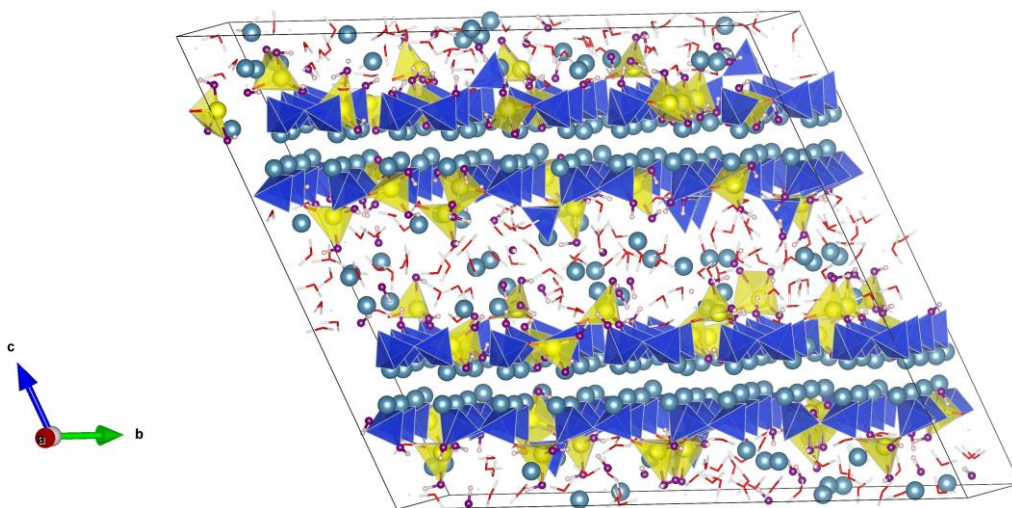

Figure S15: Large representative atomic-level structure of zinc-modified C-S-H as determined with $(Zn:Si)_i = 0.4$ and Ca:Si = 1.7. The structure measures approximately 27 Å × 39 Å × 31 Å andincludes $Q^{(2p,Zn)}$ and $Q^{(1,Zn)}$ as the new silicon sites. Silicate tetrahedra are depicted in blue; zincatetetrahedra are depicted in yellow; and calcium ions are depicted in light blue.
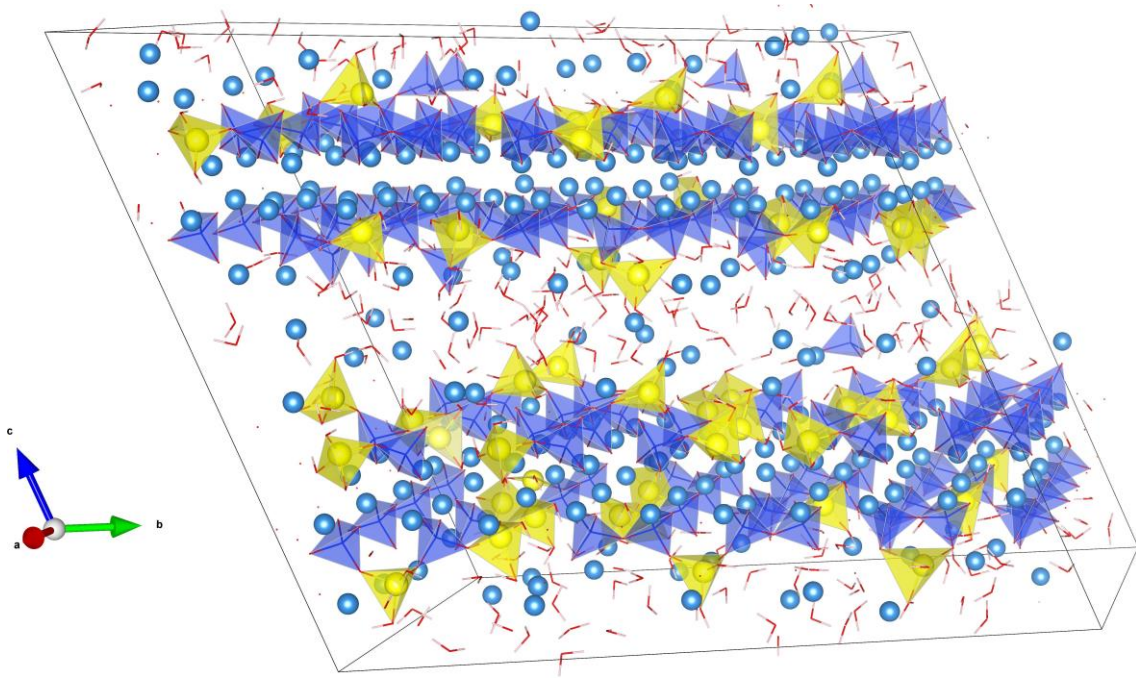
Figure S16: Large representative atomic-level structure of zinc-modified C-S-H as determined with $(Zn:Si)_i =$ 0.4. Silicate tetrahedra are depicted in blue; zincate tetrahedra are depicted in yellow; and calcium ions are depicted in light blue. In this structure, the two additional DFT- predicted sites ($Q^{(2p,2Zn)}$ and $Q^{(1,Zn\_int)}$) are also included apart from the $Q^{(1,Zn)}$ and $Q^{(2p,2Zn)}$ sites.

VII.   Zinc substituting for calcium in C-S-H

The incorporation of heavy metals into C-S-H was mostly investigated with XRD and XPS in former works. It was observed that C-S-H can incorporate up to 6 wt.% zinc,[8] and that this incorporation does not appear to influence the calcium and silicon content.[9] While it was first theorized that zinc replaces calcium in C-S-H,[10] it was later concluded that zinc is incorporated into C-S-H in tetrahedral coordination, and according to measured Ca-Zn distances indicates that the zinc tetrahedra substitutes the silicon tetrahedra,[11] which was also observed with ^{29}Si NMR.[12] The ^{29}Si NMR suggests a Zn-O-Si linkage, where a silicon tetrahedron is linked to silicon and zinc tetrahedra.

Additionally, our DFT-relaxed structures where zinc substituted for calcium in the main layer presented zinc in a quasi-6-fold coordination and with interatomic distances between zinc and oxygen which were unusually long (20% more than expected for C-S-H systems). Tetrahedral coordination was never achieved.
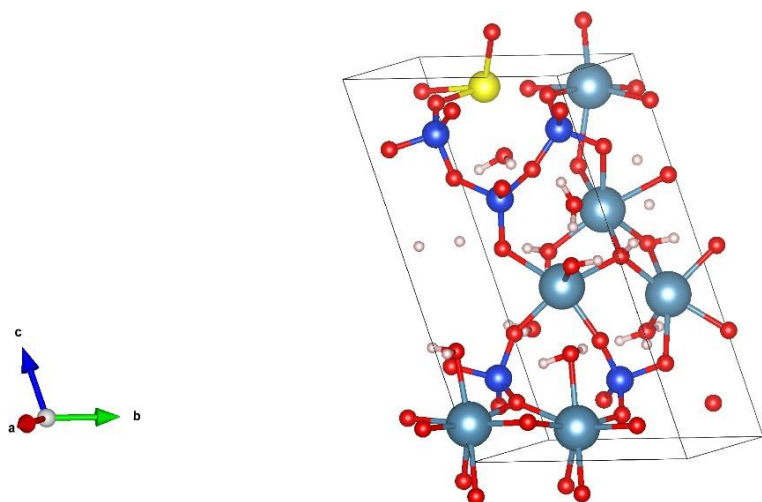
103

Figure S17: Structure where zinc substitutes calcium in the main layer.

Annex 2: Incorporation of zinc in C-A-S-H (C-Z-A-S-H)

This annex section corresponds to a short side project which is of potential interest regarding the precipitation of C-S-H in presence of both aluminum and zinc species.

I. STEM-EDX Analysis of zinc-modified C-S-H, C-A-S-H and C-Z-A-S-H

Zinc-modified C-S-H and C-A-S-H samples were precipitated following the dropwise precipitation method used by Morales-Melgares et al.[13] and Kunhi et al.[14] with a nominal $(Zn:Si)_i$ of 0.15 and a nominal $(Al:Si)_i$ of 0.15. Samples were analyzed with STEM and EDX using a Tecnai OSIRIS (Thermofisher). A summary image of the results is shown below.
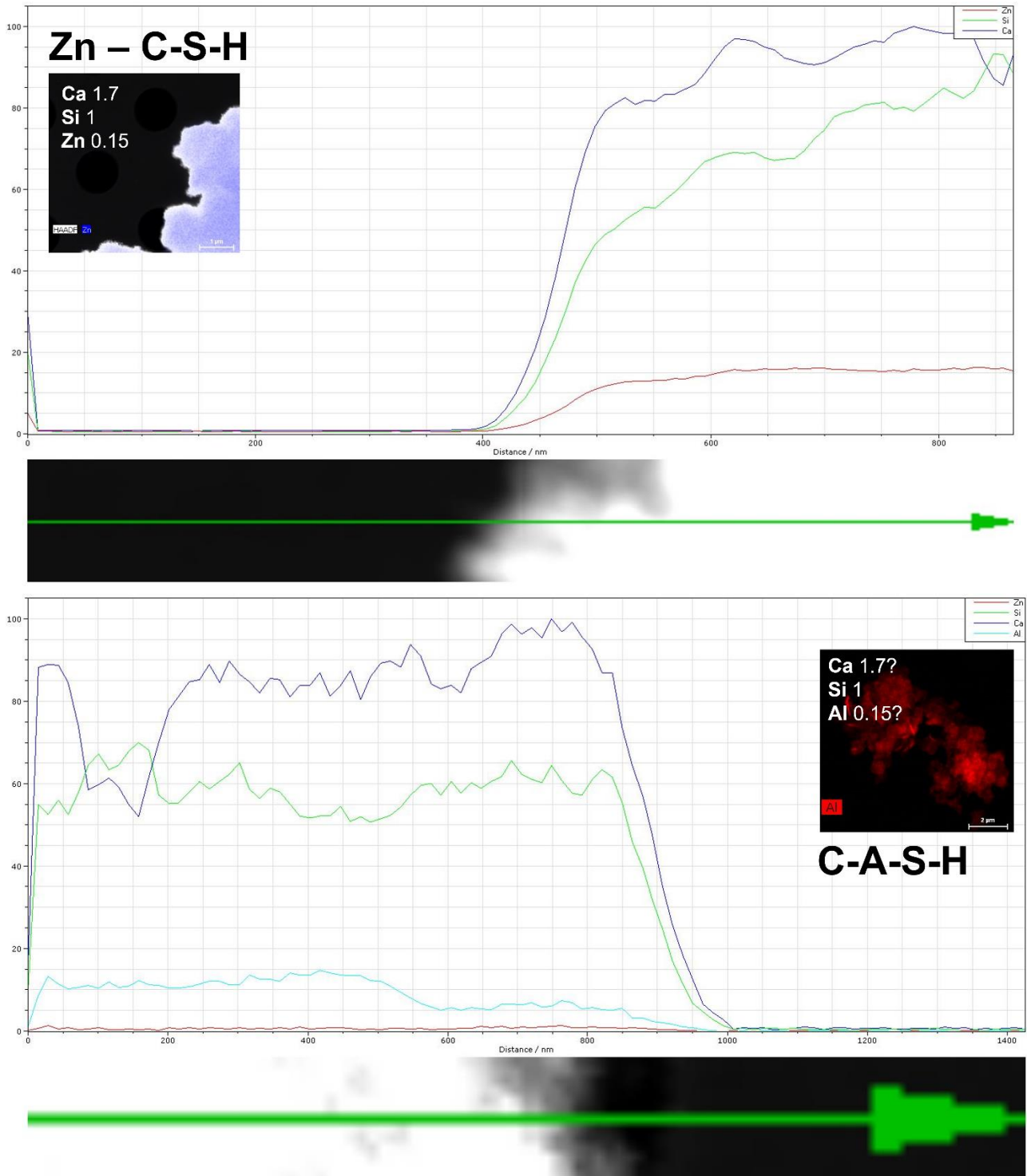

Figure S18: Top) Zinc-modified C-S-H sample with nominal $(Zn:Si)_i$ of 0.15 and down) C-A-S-H sample with nominal $(Al:Si)_i$ of 0.15. Both figures show a line (green) along which the EDX analysis was carried out and which corresponds to the EDX counts in the graphs.

Results point to the fact that zinc and aluminum are incorporated into the C-S-H structure, which is widely accepted by now. The C-A-S-H sample presented a C_xAH_y phase (or phases) which is attributed to C_4AH_y, according to Kunhi et al.[14]

A C-Z-A-S-H sample was precipitated using the same dropwise precipitation method, but having the titrated solution contain both calcium nitrate tetrahydrate ($Ca(NO_3)_2·4H_2O$), zinc nitrate hexahydrate ($Zn(NO_3)_2·6H_2O$) and aluminum nitrate nonahydrate ($Al(NO_3)_3·9H_2O$). This sample was then analyzed through STEM-EDX. Results are shown below.
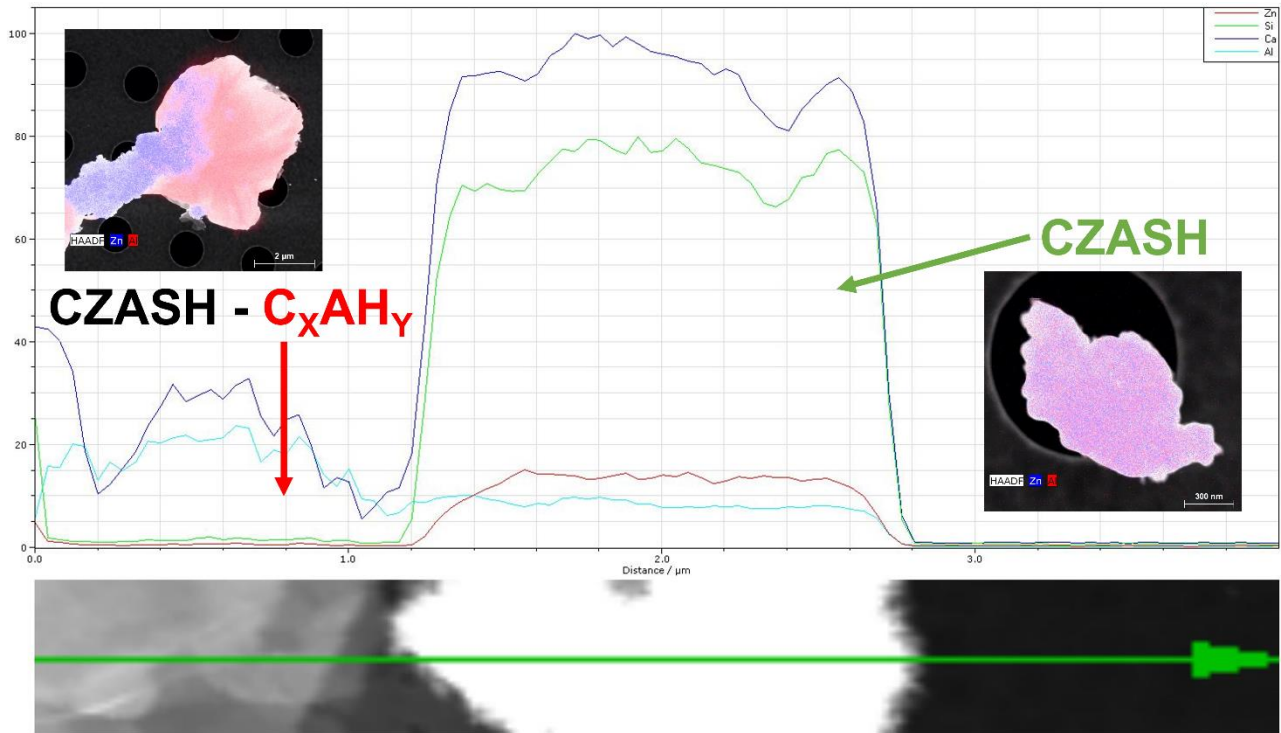

Figure S19: C-Z-A-S-H sample with nominal $(Zn:Si)_i$ and $(Al:Si)_i$ of 0.15. This figure shows a line (green) along which the EDX analysis was carried out and which corresponds to the EDX counts in the graphs.

These preliminary results point to a double incorporation of both aluminum and zinc, which seem to be able to be incorporated in the C-S-H structure at the same time. C_xAH_y phases are still present and higher EDX counts for zinc suggest that zinc might be preferentially occupying sites which are available for aluminum as well (i.e the bridging site).

An in depth ^{29}Si-NMR and ^{27}Al-NMR (and potentially [67]Zn-NMR) analysis could help elucidate the mechanisms behind this apparent competition of minor elements. This could be of potential interest since the atomic-level structures of both materials have already been resolved and because any industrial cementitious system will also contain aluminum, and it is thus important to understand how zinc might modify not only C-S-H but also C-A-S-H.

References

(1)   Renaudin, G.; Russias, J.; Leroux, F.; Frizon, F.; Cau-dit-Coumes, C. Structural Characterization of C–S–H and C–A–S–H Samples—Part I: Long-Range Order Investigated by Rietveld Analyses. *J Solid State Chem* **2009**, *182* (12), 3312–3319. https://doi.org/https://doi.org/10.1016/j.jssc.2009.09.026.

(2)   Kumar, A.; Walder, B. J.; Kunhi Mohamed, A.; Hofstetter, A.; Srinivasan, B.; Rossini, A. J.; Scrivener, K.; Emsley, L.; Bowen, P. The Atomic-Level Structure of Cementitious Calcium Silicate Hydrate. *The Journal of Physical Chemistry C* **2017**, *121* (32), 17188–17196.

(3)   Harris, M.; Simpson, G.; Scrivener, K.; Bowen, P. A Method for the Reliable and Reproducible Precipitation of Phase Pure High Ca/Si Ratio (> 1.5) Synthetic Calcium Silicate Hydrates (CSH). *Cem Concr Res* **2022**, *151*, 106623.

(4)   Van Meerten, S. G. J.; Franssen, W. M. J.; Kentgens, A. P. M. SsNake: A Cross-Platform Open-Source NMR Data Processing and Fitting Application. *Journal of Magnetic Resonance* **2019**, *301*, 56–66.

(5)   Liu, S. F.; Mao, J. D.; Schmidt-Rohr, K. A Robust Technique for Two-Dimensional Separation of Undistorted Chemical-Shift Anisotropy Powder Patterns in Magic-Angle-Spinning NMR. *Journal of Magnetic Resonance* **2002**, *155* (1), 15–28.

(6)   Herzfeld, J.; Berger, A. E. Sideband Intensities in NMR Spectra of Samples Spinning at the Magic Angle. *J Chem Phys* **1980**, *73* (12), 6021–6030.

(7)   Mohamed, A. K.; Parker, S. C.; Bowen, P.; Galmarini, S. An Atomistic Building Block Description of CSH-Towards a Realistic CSH Model. *Cem Concr Res* **2018**, *107*, 221–235.

(8)   Stumm, A.; Garbev, K.; Beuchle, G.; Black, L.; Stemmermann, P.; Nüesch, R. Incorporation of Zinc into Calcium Silicate Hydrates, Part I: Formation of CSH (I) with C/S= 2/3 and Its Isochemical Counterpart Gyrolite. *Cem Concr Res* **2005**, *35* (9), 1665–1675.

(9)   Ziegler, F.; Scheidegger, A. M.; Johnson, C. A.; Dáhn, R.; Wieland, E. Sorption Mechanisms of Zinc to Calcium Silicate Hydrate: X-Ray Absorption Fine Structure (XAFS) Investigation. *Environ Sci Technol* **2001**, *35* (7), 1550–1555. https://doi.org/10.1021/es001437+.

(10)   Stephan, D.; Maleki, H.; Knöfel, D.; Eber, B.; Härdtl, R. Influence of Cr, Ni, and Zn on the Properties of Pure Clinker Phases Part II. C3A and C4AF. *Cem Concr Res* **1999**, *29* (5), 651–657. https://doi.org/10.1016/S0008-8846(99)00008-3.

(11)   Tommaseo, C. E.; Kersten, M. Aqueous Solubility Diagrams for Cementitious Waste Stabilization Systems. 3. Mechanism of Zinc Immobilizaton by Calcium Silicate Hydrate. *Environ Sci Technol* **2002**, *36* (13), 2919–2925. https://doi.org/10.1021/es0102484.

(12)   Rose, J.; Moulin, I.; Masion, A.; Bertsch, P. M.; Wiesner, M. R.; Bottero, J. Y.; Mosnier, F.; Haehnel, C. X-Ray Absorption Spectroscopy Study of Immobilization Processes for Heavy Metals in Calcium Silicate Hydrates. 2. Zinc. *Langmuir* **2002**, *17* (12), 3658–3665. https://doi.org/10.1021/la001302h.

(13)   Morales-melgares, A.; Casar, Z.; Moutzouri, P.; Venkatesh, A.; Cordova, M.; Bowen, P.; Scrivener, K.; Emsley, L. Atomic-Level Structure and Kinetics of Synthetic Zinc-Modified C-S-H. **2022**, *97* (2), 3693.

(14)   Kumar, A.; Walder, B. J.; Kunhi Mohamed, A.; Hofstetter, A.; Srinivasan, B.; Rossini, A. J.; Scrivener, K.; Emsley, L.; Bowen, P. The Atomic-Level Structure of Cementitious Calcium Silicate Hydrate. *Journal of Physical Chemistry C* **2017**, *121* (32), 17188–17196. https://doi.org/10.1021/acs.jpcc.7b02439.

Anna Morales-Melgares

Science Communication + Content Creation and Management
Lausanne, Switzerland
Contact:
078 918 90 21
moralesmelgaresanna@hotmail.com
sizemattersbaby@gmail.com

I am a Material Science PhD graduate with a high interest in science communication and a personal nanoscience communication project in social media with my brand SizeMatters. My social media journey has increased my reach across YouTube and other platforms and has allowed me to publish my first science communication book, El Nanomundo al Descubierto, with Editorial Planeta.

Social Media Links:
YouTube
Twitter
Instagram
TikTok
Facebook

Metrics:

127.3K subs.

26.5K subs.

34.1K subs.

544.8K YouTube views in the last 90 days

Proficient Skills:
Content Creation

Media Management

Google Analytics

Lab Expertise

Adobe Premiere Pro

Project Management

Languages:
Spanish (Native)
Catalan (Native)
English (C2)
French (B1)

Employment history

Scientific Content Creator (SizeMatters)
March 2019 – Present

My YouTube channel, SizeMatters, which focuses on communicating nanotechnology to the general public, gathers more than 126K subscribers to date, and more than 2.7M views. SizeMatters' communities are managed across other social media platforms including Instagram, TikTok and Twitter.

PhD Researcher (EPFL, Lausanne)
September 2019 – September 2023

Studied and resolved the atomic-level structure of zinc-modified C-S-H by means of nuclear magnetic resonance (NMR). Additionally, developed a thermodynamic and kinetic model for the precipitation of this phase in collaboration with the Paul Scherrer Institute.

Education

Dip. Management of Digital Communities (TECH, online)
September 2023 – Present

PhD. Material Sciences (EPFL, Lausanne)
September 2019 – September 2023

M.Sc. Material Sciences (EPFL, Lausanne)
September 2017 – September 2019

B.Sc. Nanotechnology (UAB, Barcelona)
September 2012 – September 2017

Internships

Research Intern (NIMS, Tsukuba)
July 2018 – September 2018

Severo Ochoa Fellow (ICN2, Barcelona)
July 2016 – February 2017

Research Intern (CNM, Barcelona)
March 2016 – July 2016

Research Intern (Unibas, Basel)
September 2014 – February 2014

Scholarships and Awards

QSIT Inspire Potentials Master Thesis Award
April 2019 – September 2019

Severo Ochoa Fellowship
July 2016 – February 2016

Publications

A Comprehensive Thermodynamic and Kinetic Model for C-S-H Precipitation
Research paper, under review

"El Nanomundo al Descubierto"
Book (2023) Editorial Planeta

The Atomic-Level Structure of Zinc-Modified Cementitious Calcium Silicate Hydrate
Research paper (2023) Journal of American Chemical Society (JACS)

PbTiO3 Ferroelectric Oxide as an Electron Extraction Material for Stable Halide Perovskite Solar Cells
Research paper (2019), Sustainable Energy and Fuels

Interfacial Engineering of Metal Oxides for Highly Stable Perovskite Solar Cells
Research paper (2018), Advanced Materials

About me

I enjoy art in all its forms, especially film and videogames. I am sporty and friendly, and really like going to the gym and doing barbecues and Spanish paellas with my friends. I believe in a balanced life between my job, my friends and family and myself; and I also think that is key to communicate effectively through social media, since it is crucial to be relatable and genuine.

My favorite band is Daft Punk, but lately I am really enjoying Nathy Peluso; here is one motto from her lyrics that really stood out for me:

"I'm about to turn 30 and I just realized that she who loses wins more than she who doesn't try"

- Nathy Peluso (Salvaje, 2023)